

Spin transport in nanocontacts and nanowires

Tesis doctoral

por

David Jacob

Director de tesis: Juan José Palacios Burgos
Departamento de Física Aplicada
Universidad de Alicante

Alicante en febrero de 2007

In this thesis we study electron transport through magnetic nanocontacts and nanowires with ab initio quantum transport calculations. The aim is to gain a thorough understanding of the interplay between electrical conduction and magnetism in atomic-size conductors and how it is affected by different aspects as e.g. the atomic structure and the chemical composition of the conductor. To this end our ab initio quantum transport program ALACANT which combines the non-equilibrium Green's function formalism (NEGF) with density functional theory (DFT) calculations has been extended to describe spin-polarized systems. We present calculations on nanocontacts made of Ni as a prototypical magnetic material. We find that atomic disorder in the contact region strongly reduces the a priori high spin-polarization of the conductance leading to rather moderate values of the so-called ballistic magnetoresistance (BMR). On the other hand, we show that the adsorption of oxygen in the contact region could strongly enhance the spin-polarization of the conduction electrons and thus BMR by eliminating the spin-unpolarized s-channel. Finally, we show that short atomic Pt chains suspended between the tips of a nanocontact are magnetic in contrast to bulk Pt. However, this emergent nanoscale magnetism barely affects the overall conductance of the nanocontact making it thus difficult to demonstrate by simple conductance measurements. In conclusion, we find that spin-transport through atomic-scale conductors is quite sensitive to the actual atomic structure as well as to the chemical composition of the conductor. This presents both, opportunities and challenges for the realization of future nanoscale spintronics devices.

Acknowledgments

I am especially grateful to Prof. Juanjo Palacios and Dr. Joaquin Fernández-Rossier for directing this work. The discussions on physical problems were always both, enlightening and enjoyable. Their enthusiasm for the physics was really inspiring and motivating. I also would like to thank Dr. Carlos Untiedt, Dr. María José Caturla, Prof. Enrique Louis, Prof. José Antonio Vergés and Dr. Guillermo Chiappe for fruitful discussions. Special thanks to James McDonald who built the Beowulf cluster facility here in the Applied Physics Department without which this work would not have been possible. I thank the MECD for financial support under grant No. UAC-2004-0052. I feel grateful to all my colleagues, Cristophe, Deborah, Eladio, Federico, Fernando, Giovanni, Igor, Loïc, Martin, Natamar, Pedro, Reyes and Richard which have made my life here in Alicante really enjoyable by sharing a lot of beers, barbecues, paellas, tapas, and a lot more with them. I would like to thank my family for their constant support. Finally but most importantly, I would like to thank María for her love and support, and especially for her patience during the last months.

Contents

1	Introduction	9
2	Quantum theory of electron transport	15
2.1	Landauer formalism	15
2.2	Non-equilibrium Green's function formalism	19
2.2.1	Hamiltonian and overlap	19
2.2.2	Green's function for the open system	21
2.2.3	Calculation of density matrix and electron number at equilibrium	24
2.2.4	Non-equilibrium density matrix	27
2.2.5	Current and transmission	29
2.3	Application to simple models	32
2.4	Discussion of the Landauer approach	37
3	<i>Ab initio</i> quantum transport	39
3.1	Density functional theory	39
3.1.1	Hohenberg-Kohn theorem	40
3.1.2	Kohn-Sham equations	40
3.1.3	Energy functionals	42
3.2	Kohn-Sham based NEGF formalism	44
3.2.1	Modeling of the bulk electrodes	48
3.3	Beyond density functional theory	53
4	Spin transport	57
4.1	Domain wall scattering in the classical <i>sd</i> -model	58
4.1.1	Abrupt domain wall	59
4.1.2	Smooth domain walls	60
4.2	One-dimensional Hubbard model	61
4.2.1	Hartree-Fock approximation – the Stoner model	61
4.2.2	Homogeneous Chain	62
4.3	DW formation and scattering	64
4.4	Summary	68
5	Ni nanocontacts	71
5.1	Monatomic Ni chain	72
5.2	More realistic contact geometries	77
5.3	Orbital eigenchannel analysis	79
5.4	The self-interaction problem	86
5.5	Discussion of results	88

Contents

6 NiO chains in Ni nanocontacts	91
6.1 Electronic and magnetic properties of bulk NiO	91
6.2 One-dimensional NiO	93
6.3 O-bridge in Ni nanocontacts	96
6.4 O-Ni-O bridge in Ni nanocontacts	99
6.5 Conclusions	100
7 Transport through magnetic Pt nanowires	101
7.1 Electronic and magnetic structure of atomic Pt chains	102
7.2 Transport through suspended Pt chains	104
7.3 Conclusions and Discussion	106
8 Summary and Outlook	109
8.1 Overview of developed computational tools	109
8.2 Summary of results	109
8.3 Outlook	111
A Representation of operators in non-orthogonal basis sets	113
B Partitioning method	115
C Self-energy of a one-dimensional lead	117
D Bethe lattices	119
E Non-Collinear Unrestricted Hartree-Fock Approximation	121
Bibliography	129
List of abbreviations	131
List of publications	133

1 Introduction

The invention of the integrated circuit (IC) in 1959 by J. Kilby (Nobel price in 2000 together with H. Kroemer and Z. I. Alferov) triggered the stunning and still ongoing development of computer technology which has led to ever faster, cheaper, and smaller computers. An IC is an electronic circuit where all electronic components (transistors, capacitors, interconnects) are integrated on a single silicon chip. The successive improvement of the fabrication techniques and the introduction of new materials allowed to constantly decrease the sizes of the IC components so that an increasing number of them could be integrated on a single IC. This development has led to increasingly powerful and faster computer chips. The other basic ingredient of modern computer systems are non-volatile mass storage devices presented in today's computers by hard drives which store data in form of magnetic bits on magnetic disks (hard disks). Here the improvement of fabrication techniques, introduction of new materials and new concepts for the read and write mechanism of the hard drives allowed to constantly decrease the minimum area needed to record a magnetic bit making them faster and increasing their data capacities by several orders of magnitude since the invention in 1979.

Thus miniaturization has become the leading paradigm of today's computer industry and a lot of effort in industrial research and development is dedicated to further decreasing the minimum feature size of semiconductor chips or the areas of the magnetic bits on hard disks. However, this miniaturization trend cannot go on forever since the atomic scale presents an ultimate limit which can never be surpassed and possibly not even reached. This is not a kind of hypothetical scenario but rather relevant for the development of microprocessor chips in the near future as is impressively demonstrated by today's most advanced microprocessors and memory chips whose smallest features (the gate length) have already reached a size in the order of 30 nm, and IC transistors with a gate length of only 10nm are currently under investigation [1]. The miniaturization of IC components has in fact reached a level where atomic structure effects like *electro-migration* processes [2] become an issue because they can seriously limit the usability and lifetime of ICs. Another serious problem are the so-called subthreshold leakage currents between the electrodes of the transistor which increase considerably as the size of the transistors shrinks and are responsible for a grand part of the power consumption loss in microchips [3]. Similar problems arise when reducing the dimensions of magnetic bits. Moreover, when finally reaching the nanoscale, inevitably quantum effects will come into play and seriously challenge current silicon based IC technology possibly demanding radically different approaches. *Molecular electronics* and *spintronics* are two promising examples of radically new strategies for information processing.

Molecular electronics aims at employing single molecules as the ultimate electronic components for realizing nanoscale electronic circuits. Indeed the use of single molecules as rectifiers for electrical current has been proposed as early as 1974 by Aviram and Ratner [4]. But not until the advent of the scanning probe microscopes was it possible to study and manipulate material properties at the molecular or atomic level let alone electrically

1 Introduction

contact individual molecules. The invention of the scanning tunneling microscope (STM) by G. Binnig and H. Rohrer in 1981 (Nobel price in 1986 together with E. Ruska) [5] made it for the first time possible to study (metallic) surfaces and molecules adsorbed on them with atomic resolution. By contacting an individual molecule adsorbed on a metal surface with the STM tip it is possible to measure the conductance of this molecular conductor. This technique was first employed to measure the conductance of individual C_{60} molecules [6, 7]. Since then more conductance measurements of individual molecules have been reported in the literature [8, 9, 10, 11, 12]. However, establishing electrical contacts with individual molecules and measuring their conductance remains a formidable task and care must be taken to assure that a molecule has indeed been contacted [12].

Using an STM it is also possible to fabricate atomic-size nanocontacts where two sections of a metal wire are connected via a constriction of just a few atoms in diameter which thus represent the ultimate electrical conductors with respect to size [13]. Nanocontacts are formed when an STM tip is pressed into the substrate and then slowly retracted until an atomic-size neck is formed [14]. Another technique to fabricate very stable and reproducible nanocontacts in an efficient and cheap way is the mechanically controllable break junction technique (MCBJ)[15] where a notched thin wire mounted on a bending beam is broken in controlled way. The bending can be fine-controlled by a piezo element allowing a very precise control over the separation of the two sections of the wire. Just a third method to fabricate nanocontacts is by electrodeposition [16, 17] where the nanocontacts are electro-chemically deposited between two macroscopic electrodes. Interesting phenomena for atomic-size nanocontacts have been observed in experiments like the formation of monatomic chains suspended between Gold or Platinum contacts, see e.g. [18].

Another approach that promises to revolutionize conventional electronics is the field of spintronics [19] which aims to combine the traditionally separated fields of magnetic information storage and semiconductor electronics in order to build more powerful electronic devices that exploit the electron spin in addition to the electron charge. The example that best illustrates the spintronics philosophy is the so-called Magnetic Random Access Memory (MRAM) [20] which combines the advantages of conventional magnetic data storage (hard drives) and conventional electronic random access memory (RAM) into a single device in order to achieve at the same time non-volatile memory cells that are as fast as conventional RAM cells.

An essential ingredient for spintronics is the generation of spin-polarized electron currents which is typically accomplished by passing the electrical current through a ferromagnetic metal. The other basic ingredient are spin-valves which are devices that change their resistivity depending on the polarization of the spin-current and thus allow to detect the spin-polarization of an electrical current. An example for an actual spin-valve device are the giant magneto-resistance (GMR) devices consisting of alternating magnetic and non-magnetic metal multilayers that display a strong sensitivity of the electrical current to the relative orientation of the magnetizations of the magnetic layers [21]. Soon after its discovery in 1988, the GMR effect was exploited to improve the sensitivity of read heads in hard drives which before had been based on simple magnetic induction or the much smaller anisotropic magneto-resistance effect displayed by bulk metals. This in turn allowed to decrease the size of the magnetic bits and thus to increase the data storage density of the hard disks dramatically. Consequently, GMR read heads can now be found in the hard drives of every modern computer.

Magnetic tunnel junctions (MTJs) are similar to GMR devices but feature an insulating layer instead of the non-magnetic metal layer separating the ferromagnetic metal layers which presents a tunnel barrier for the electrons flowing between the ferromagnetic layers. MTJs display a MR known as tunneling magneto-resistance (TMR) which was first demonstrated by Julliere [22]. The TMR spin-valve is a crucial ingredient for an efficient realization of the above described MRAM device [23]. In the earlier experiments TMR was found to be much smaller than GMR, but very recently new material combinations (Fe-MgO-Fe) for the MTJs motivated by theoretical studies [24, 25] have lead to a dramatic increase of the TMR which now actually exceeds GMR values [26, 23].

GMR and TMR spin-valves are nanoscale devices in the sense that the thicknesses of the layers making up the spin-valve structures are on the nanometer scale, and can be made as thin as 5Å with modern growth methods, so that electron transport is governed by quantum effects. In fact, these devices actually only work because of quantum effects, i.e. the coherent transmission of a spin-polarized current through the non-magnetic layer. Moreover, when finally shrinking the other two dimensions of a spin-valve to the nanoscale, quantum and atomic structure effects will become even more important. Thus it is of fundamental importance to gain a thorough understanding of the interplay between magnetism and electrical conduction at the atomic scale. Nanocontacts and nanowires made from ferromagnetic metals allow to study this interplay between magnetism and electrical conduction or in more fundamental terms the interplay between electron spin and charge flow in the smallest possible magnetic conductors.

An important question is whether GMR or TMR effects survive when the other two device dimensions are scaled down to the nanoscale, or whether other magneto-resistance (MR) effects emerge at the nanoscale which could be exploited for the realization of nanoscale spintronics devices. Therefore, measuring the MR of ferromagnetic nanocontacts has recently attracted a lot of interest [27, 28, 29, 30, 31, 32, 33, 34, 35, 36, 37, 38]. Indeed, some groups have found a huge MR (exceeding even the GMR effect) for Ni nanocontacts which was coined ballistic magneto-resistance (BMR) for its supposed origin in the ballistic scattering of spin polarized electrons on a sharp domain wall (DW) which should form at the atomic neck of the nanocontact[39, 40, 41]. However, the possibility of huge BMR in ferromagnetic nanocontacts has been a controversial topic since its discovery, and is one of the principal topics of this thesis (See Ch. 5 and Ch. 6).

Integrating the fields of molecular electronics with that of spintronics is another promising approach for realizing nanoscale spintronics devices because of the expected very long spin-decoherence times in organic molecules as compared to bulk metals and semiconductors. Strong indications on the possibility of integrating the two fields come from a few recent experiments indicating e.g. a long spin-flip scattering length for carbon nanotubes [42], spin injection from strongly spin polarized materials into carbon nanotubes [43], and spin transport through organic molecules [44]. Since ferromagnetic nanocontacts are a basic ingredient for molecular spintronics for injecting spin-polarized currents into the molecules, it is also in this context important to gain a solid understanding of electrical conduction and magnetism in nanocontacts.

In this thesis electron transport through magnetic nanocontacts and nanowires is investigated theoretically. The starting point for the theoretical investigation of electron transport through nanocontacts and nanowires is the Landauer formalism, which is introduced in Ch. 2. The Landauer approach assumes that electron transport through nanostructures is phase coherent, i.e. decoherence by phase-breaking scattering processes

1 Introduction

is neglected. This turns out to be a reasonable assumption at low temperatures and for small bias voltages. Indeed, the Landauer approach has been successfully applied for studying electrical transport through metallic nanocontacts, so that now we have a good understanding of atomic scale conductors [45, 46].

In order to predict the transport properties of atomic scale nanocontacts and nanowires it is important to have a realistic description of the electronic and magnetic structure of the nanocontact taking into account its actual atomic structure. This can be achieved most conveniently by ab initio electronic structure methods based on localized atomic orbitals like e.g. GAUSSIAN [47] or SIESTA [48]. Ch. 3 shows how ab initio quantum transport calculations based on density functional theory (DFT) [49] are implemented in the ALACANT package [50, 51] which as a part of this thesis was extended in order to describe spin transport in magnetic systems and to incorporate one-dimensional leads calculated from first principles in addition to the semi-empirical Bethe lattice electrodes [52]. Other DFT based quantum transport methods are developed by various groups around the world [53, 54]. In Ch. 4, the Landauer formalism is generalized to describe transport of spin-polarized electrons (or in short “spin transport”) in magnetic nanostructures. In order to understand basic aspects of spin transport in nanoscopic conductors like the scattering of spin-polarized electrons on domain walls as well as the formation of domain walls in nanoscopic conductors, the spin-resolved transport formalism is applied to simplified models of magnetic materials.

In Ch. 5 spin transport through Ni nanocontacts is investigated theoretically with ab initio quantum transport calculations using the afore mentioned ALACANT package. In order to asses the above discussed possibility of huge BMR in Ni nanocontacts, we calculate the magneto resistance due to the formation of a DW at the atomic neck of the nanocontact for different contact geometries. We find that BMR of *pure* Ni nanocontacts is rather moderate [55], i.e. much smaller than the famous GMR effect. This is contrary to the claims of huge BMR found in the first experiments on Ni nanocontacts but in agreement with some recent experiments measuring very clean samples under very controlled conditions [37, 38].

In Ch. 6, we study the electronic and magnetic structure, and transport properties of atomic NiO chains, both ideal infinite ones and short ones suspended between the tip atoms of Ni nanocontacts. It is found that the presence of a single oxygen atom between the tip atoms of a Ni nanocontact increases the spin-polarization of the conduction electrons dramatically, converting the nanocontact into an almost perfect half-metallic conductor, and leading to huge values of the BMR [56]. It is also discussed to what extent these results could explain the huge MR of Ni nanocontacts obtained in the experiments mentioned above.

In Ch. 7, the electronic structure and transport properties of *magnetic* Pt nanowires is studied. It had been shown before that atomic Pt nanowires can actually become magnetic in contrast to bulk Pt due to the lower coordination of the Pt atoms in the atomic chain compared to the bulk [57, 58]. We reproduce this result for infinite chains, and find that also short Pt chains suspended between the tips nanocontacts become magnetic. However, the overall conductance of the Pt nanocontact is barely affected by the magnetism of the chain, so that simple conductance measurements of Pt nanocontacts cannot probe the magnetism [59].

Finally, Ch. 8 concludes this thesis with a general discussion of the obtained results, and their significance in the broader context of spin transport and spintronics in nanoscopic

systems. Moreover, we will point out open questions and give an outlook on possible future lines of work.

1 Introduction

2 Quantum theory of electron transport

The description of electrical conduction through a nanoscopic conductor like a molecule bridging the tips of two metal electrodes or a nanoscopic constriction in a metal wire as shown in Fig. 2.1 is a challenging problem. In systems of such small size the dimension of the conductor becomes comparable to the Fermi wavelength of the conduction electrons, so that the transport properties of the conductor are governed by quantization effects demanding a full quantum treatment of the transport process. Moreover, for molecular- and atomic-size conductors the actual atomic structure of the conductor has a strong effect on the electronic structure and transport properties.

Our starting point for a quantum description of electrical conduction is the Landauer formalism [60, 61, 62, 63, 64] which is introduced in Sec. 2.1. In Sec. 2.2 we describe the Landauer formalism within the framework of non-equilibrium Green's functions (NEGF) formalism. In Sec. 2.3 we illustrate the derived formalism by applying it to simple model systems. Finally, in Sec. 2.4 we discuss the validity of the Landauer approach, pointing out its problems and limitations, and indicating ways of improving it as well as alternative approaches.

2.1 Landauer formalism

In the Landauer formalism electron transport is considered as a scattering process where the nanoscopic conductor acts as a quantum mechanical scatterer for the electrons coming in from the leads. It is further assumed that the electrons scatter only elastically on the nanoscopic sample, i.e. inelastic scattering e.g. by phonons or by other electrons is neglected so that transport becomes phase coherent. Thus electron transport through a nanoscopic conductor is described in terms of *non-interacting* quasi particles coming in

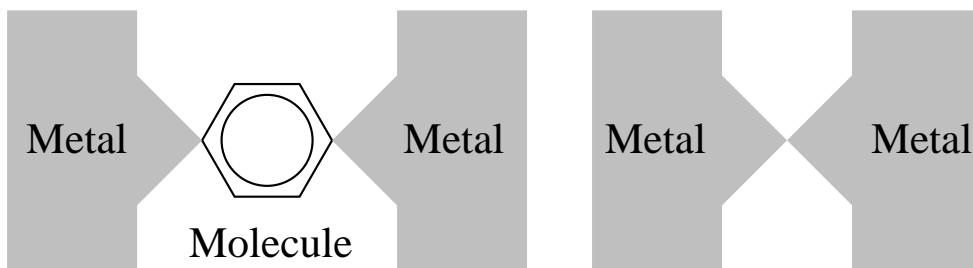


Figure 2.1: Sketch of typical nanoscopic conductors. Left: A molecule connecting the tips of two bulk metal electrodes. Right: A nanoscopic constriction of a metal wire connecting two bulk metal electrodes.

2 Quantum theory of electron transport

from the leads and being scattered elastically on the nanoscopic device.

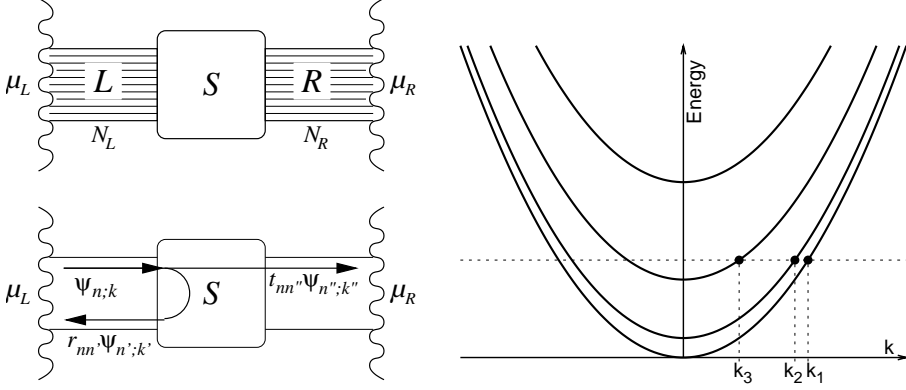


Figure 2.2: Left: Schematic illustration of Landauer formalism (See text for explanation). Right: Energy dispersion of propagating modes for electrons moving freely in one direction and confined in the other directions.

Fig. 2.2 shows how the transport problem is modeled in the Landauer formalism: The central scattering region (S) containing the nanoscopic conductor is connected via two ideal semi-infinite leads of some finite width to two electron reservoirs that are each in thermal equilibrium but at different chemical potentials μ_L and μ_R . The reservoirs are assumed to be reflection-less, i.e. incoming electrons are not reflected back to the leads, so that the two reservoirs are independent of each other. Due to the finite width of the leads the motion of the electrons perpendicular to the direction of the leads is quantized giving rise to a finite number of propagating modes or bands $\{\psi_{n,k}\}$ for a given energy E . This is illustrated on the right hand side of Fig. 2.2 for the case of a two-dimensional electron gas confined in the vertical direction but moving freely in the horizontal direction. In that case a propagating wave is given by a plane wave in the z -direction e^{ikz} modulated by a transverse wavefunction $\phi_n(x, y)$:

$$\psi_{n;k}(x, y) = \phi_n(x, y)e^{ikz}.$$

In the more general case of a periodic potential, $V(x, y, z + a) = V(x, y, z)$, generated e.g. by the atomic nuclei in the direction of the lead the propagating modes are Bloch waves

$$\psi_{n;k}(x, y, z) = \sum_{j,\alpha} c_{n;\alpha}(k) \phi_{j;\alpha}(x, y, z) e^{ikaj},$$

where the sum goes over all unit cells j of the lead and $\phi_{j\alpha}(x, y, z)$ is a localized wavefunction centered in unit cell j . From the fact that $\phi_{j\alpha}(x, y, z + a) = \phi_{j-1\alpha}(x, y, z)$, it follows that the Bloch functions also have the periodicity of the potential, apart from a trivial phase factor:

$$\begin{aligned} \psi_{n;k}(x, y, z + a) &= \sum_{j,\alpha} c_{\alpha;n}(k) \phi_{j;\alpha}(x, y, z + a) e^{ikaj} \\ &= e^{ika} \sum_{j,\alpha} c_{\alpha;n}(k) \phi_{j-1;\alpha}(x, y, z) e^{ika(j-1)} = e^{ika} \psi_{n;k}(x, y, z). \end{aligned}$$

We define $k_n(E)$ as the wave vector corresponding to the band n at the energy E that gives rise to a current in the *positive* z -direction. The current associated with the propagating mode n is given by its group velocity which in turn is given by the derivative of the dispersion relation $\frac{1}{\hbar} \frac{dE_n}{dk}$ for that band:

$$j_n(k) := \frac{e}{\lambda} v_n(k) = \frac{e}{\lambda \hbar} \frac{dE_n}{dk}(k), \quad (2.1)$$

where λ is the length of the conductor. This is trivial to prove for the case of free electrons where the group velocity is directly proportional to the wave vector, $v_n(k) = \hbar k/m_e$. For Bloch waves the situation is more complicated, and the group velocity can even have the opposite sign of the wave vector. A proof can be found e.g. in the book by Ashcroft and Mermin [65].

Elastic scattering means that an electron with some energy E coming from one of the reservoirs will be scattered to some out-moving state with the *same* energy E of one of the leads, so that the process is phase coherent. Thus an incoming wave at some energy E on the left lead will give rise to a coherent superposition with outgoing states of the *same* energy E on both leads:

$$\psi_{n;k_n(E)}^L + \sum_{n' \in N_L} r_{nn'}(E) \psi_{n';-k_{n'}(E)}^L + \sum_{n'' \in N_R} t_{nn''}(E) \psi_{n'';k_{n''}(E)}^R, \quad (2.2)$$

where $r_{nn'}(E)$ is the probability amplitude for an incoming electron on mode n at energy E to be reflected into the outgoing mode n' of the left lead, and $t_{nn''}(E)$ is the amplitude for the electron to be transmitted into the mode n'' of the right lead. Thus an incoming electron on mode n of the left lead will be transmitted with a probability of $\sum_{n''} \|t_{nn''}(E)\|^2$ to the right lead giving rise to a current density in that lead of magnitude

$$j_n^t(E) := \sum_{n'' \in N_R} \|t_{nn''}(E)\|^2 j_{n''}(k_{n''}(E)). \quad (2.3)$$

The left electron reservoir injects electrons into the *right*-moving modes of the left lead up to the chemical potential μ_L . Thus the transmission of electrons through the nanoscopic conductor gives rise to a current to the right in the right electrode.

$$I_t = \sum_{n \in N_L} \int_{E_n(k) < \mu_L} dk j_n^t(E_n(k)) = \sum_{n \in N_L, n'' \in N_R} \int_{-\infty}^{\mu_L} dE \mathcal{D}_n^R(E) \|t_{nn''}(E)\|^2 j_{n''}(k_{n''}(E))$$

In the second step we have converted the integral over the wave vectors into an integral over the energy by making use of the density of states (DOS) $\mathcal{D}_n^R(E)$ projected onto band n of the right lead. For one-dimensional systems the DOS is given by the inverse derivative of the dispersion relation of the band, $\mathcal{D}_n(E) = \frac{1}{2\pi} \frac{dk_n}{dE}$, so that it cancels exactly with the group velocity of the band:

$$I_t = \sum_{n \in N_L, n'' \in N_R} \frac{e}{\hbar} \int_{-\infty}^{\mu_L} dE \|t_{nn''}(E)\|^2 = \frac{e}{\hbar} \sum_{n \in N_L} \int_{-\infty}^{\mu_L} dE T_n(E), \quad (2.4)$$

where we have defined the *transmission per conduction channel* $T_n(E)$ as

$$T_n(E) = \sum_{n'' \in N_R} \|t_{nn''}(E)\|^2. \quad (2.5)$$

2 Quantum theory of electron transport

On the other hand the right electron reservoir injects electrons into the *left*-moving modes of the right lead up to the chemical potential μ_R and the transmission of electrons through the device region gives rise to a left-directed current in the left lead:

$$I'_t = \frac{e}{h} \sum_{n \in N_R} \int_{-\infty}^{\mu_R} dE T'_n(E), \quad (2.6)$$

where $T'_{n'}(E)$ now is the transmission probability of channel n' of the right lead:

$$T'_{n'}(E) = \sum_{n \in N_L} \|t'_{n'n}(E)\|^2, \quad (2.7)$$

and $t'_{n'n}(E)$ is the transmission amplitude for a mode n' of the right lead to be transmitted into mode n of the left lead. Because of time inversion symmetry the amplitude $t'_{n'n}(E)$ is the same as the the amplitude $t_{nn'}(E)$ for the transmission from the left to the right electrode apart from a trivial phase factor. Hence the total transmission probability from the left to the right lead $T(E) := \sum_n T_n(E)$ is equal to the total transmission probability from the right to the left lead $T'(E) := \sum_{n'} T'_{n'}(E)$:

$$\sum_{n \in N_L} T_n(E) = \sum_{n \in N_L, n' \in N_R} \|t_{nn'}(E)\|^2 = \sum_{n \in N_L, n' \in N_R} \|t'_{n'n}(E)\|^2 = \sum_{n' \in N_R} T'_{n'}(E). \quad (2.8)$$

Furthermore the summed reflection probability $R'(E)$ for all electrons injected from the right reservoir at some energy E is $R'(E) = N_R - T'(E) = N_R - T(E)$. Therefore the current composed of *backscattered* electrons (originating from the right reservoir) and *transmitted* electrons (originating from the left reservoir) cancels exactly the current of the *incoming* electrons coming in from the right electron reservoir. Analogously the same holds true for the left lead. Thus the net current at some energy E is zero when the current there is current injection from *both* electrodes at that energy.

Thus assuming a positive bias voltage V , so that $\mu_L = \mu_R + eV > \mu_R$, only electrons above μ_R give a net contribution to the total current. Since for energies above μ_R the only contribution to the net current through the right lead is the transmission current I_t of electrons coming from the left, the total current for a given bias voltage V is given by the famous Landauer formula:

$$I(V) = \frac{e}{h} \sum_{n \in N_L} \int_{\mu_R}^{\mu_L} dE T_n(E). \quad (2.9)$$

Taking the derivative with respect to the bias voltage one obtains the corresponding conductance:

$$G(V) = \frac{\partial I}{\partial V} = \frac{e^2}{h} \sum_{n \in N_L} T_n(eV), \quad (2.10)$$

where $\frac{e^2}{h}$ is half the fundamental conductance quantum G_0 . The spin-degree of freedom of the electrons is contained in the index n for the channels. Assuming a spin-degenerate system the transmissions for up- and down channels are equal, so that a factor of two appears when summing transmissions over the spin-degree of freedom, and one obtains the usual Landauer formula with G_0 as the proportionality constant. Here however, we are interested in magnetic systems, so the transmissions are spin-dependent.

The transmission amplitudes $t_{nm}(E)$ define an in general non-quadratic matrix $\mathbf{t}(E) := (t_{nm}(E))$. The square of this matrix defines a (quadratic) hermitian matrix called the transmission matrix:

$$\mathbf{T}(E) := \mathbf{t}^\dagger(E)\mathbf{t}(E) \text{ or } T_{nm}(E) = \sum_m t_{m'n}^*(E)t_{n'm}(E) \quad (2.11)$$

The channel transmissions $T_n(E) = \sum_{n' \in N_R} \|t_{nn'}^r(E)\|^2$ are now just the diagonal elements of this transmission matrix, and summing up over all channel transmissions in the Landauer formula now corresponds to taking the trace of the transmission matrix:

$$G(V) = \frac{e^2}{h} \times \text{Tr}[\mathbf{T}(eV)] \text{ and } I(V) = \frac{e}{h} \sum_{n \in N_L} \int_{\mu_R}^{\mu_L} dE \text{Tr}[\mathbf{T}(E)]. \quad (2.12)$$

The transmission matrix is the central quantity in the Landauer formalism since it allows to calculate the electrical conductance and current-voltage characteristics of a nanoscopic conductor. Depending on the actual system a variety of methods exists for obtaining this quantity. For our purpose of describing transport through atomic- and molecular-size conductors the NEGF described in the next section is the most appropriate approach since it can be combined in a straight-forward manner with *ab initio* electronic structure methods like density functional theory (DFT) or the Hartree-Fock approximation (HFA) as implemented in standard quantum chemistry codes employing atomic orbital basis sets.

2.2 Non-equilibrium Green's function formalism

In this section we will restate the Landauer approach to quantum transport in the language of one-body Green's functions [66, 64]. To this end we will first introduce the Hamiltonian and overlap matrices for the transport problem in a basis set of localized atomic orbitals. We will then derive a Green's function for the finite scattering region connected on both sides to semi-infinite leads. From the Green's function (GF) one can then obtain the (reduced) density matrix and the transmission matrix. Here we will mainly follow the arguments presented by Paulsson in his introductory paper on the NEGF [67] but generalize them to non-orthogonal basis sets (NOBS) as commonly employed in quantum chemistry packages. A few other derivations of the Landauer formalism within the NEGF framework taking into account non-orthogonality of basis sets can be found in the recent literature [68, 69].

2.2.1 Hamiltonian and overlap

We divide the system into 3 parts as shown in Fig. 2.3: The left lead (L), the right lead (R), and the intermediate region called device (D) containing the central scattering region (S). This scattering region can be given by e.g. a molecule coupled to metallic contacts, or simply a nanoscopic constriction as indicated in the figure.

We assume that the leads are only coupled to the scattering region but not to each other. Thus the device region must be chosen sufficiently large for that to be true. The

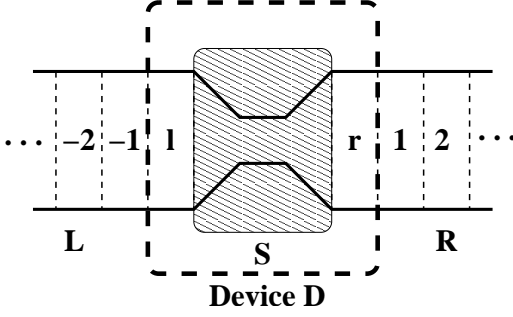


Figure 2.3: Sketch of the transport problem. L: Left (bulk) lead. D: Device. R: right (bulk) Lead. S: Central scattering region containing nanoconstriction or contacted molecule. See text for further explanations.

Hamiltonian \hat{H} describing the system is then given by the matrix

$$\mathbf{H} = \begin{pmatrix} \mathbf{H}_L & \mathbf{H}_{LD} & \mathbf{0}_{LR} \\ \mathbf{H}_{DL} & \mathbf{H}_D & \mathbf{H}_{DR} \\ \mathbf{0}_{RL} & \mathbf{H}_{RD} & \mathbf{H}_R \end{pmatrix}. \quad (2.13)$$

Furthermore we assume a non-orthogonal localized basis set. Assuming again no overlap between atomic orbitals in different leads the overlap of the atomic-orbitals of the system is given by the following overlap matrix:

$$\mathbf{S} = \begin{pmatrix} \mathbf{S}_L & \mathbf{S}_{LD} & \mathbf{0}_{LR} \\ \mathbf{S}_{DL} & \mathbf{S}_D & \mathbf{S}_{DR} \\ \mathbf{0}_{RL} & \mathbf{S}_{RD} & \mathbf{S}_R \end{pmatrix}. \quad (2.14)$$

As indicated in Fig. 2.3 we subdivide the leads into unit cells (UCs) which must be chosen sufficiently large so that the coupling between non-neighboring unit cells can be neglected. Thus in general a UC consists of several primitive unit cells (PUCs). The Hamiltonian matrix \mathbf{H}_L of the left lead can be subdivided into sub-matrices in the following manner:

$$\mathbf{H}_L = \begin{pmatrix} \vdots & \vdots \\ \cdots & \mathbf{H}_{-2,-2} & \mathbf{H}_{-2,-1} \\ \cdots & \mathbf{H}_{-1,-2} & \mathbf{H}_{-1,-1} \end{pmatrix} = \begin{pmatrix} \ddots & \ddots & \ddots & \mathbf{0} \\ & \mathbf{H}_1^\dagger & \mathbf{H}_0 & \mathbf{H}_1 \\ & & \mathbf{H}_1^\dagger & \mathbf{H}_0 & \mathbf{H}_1 \\ \mathbf{0} & & & \mathbf{H}_1^\dagger & \mathbf{H}_0 \end{pmatrix} \quad (2.15)$$

Analogously the Hamiltonian of the right lead is given by the following matrix:

$$\mathbf{H}_R = \begin{pmatrix} \mathbf{H}_{1,1} & \mathbf{H}_{1,2} & \cdots \\ \mathbf{H}_{2,1} & \mathbf{H}_{2,2} & \cdots \\ \vdots & \vdots & \end{pmatrix} = \begin{pmatrix} \mathbf{H}_0 & \mathbf{H}_1 & & \mathbf{0} \\ \mathbf{H}_1^\dagger & \mathbf{H}_0 & \mathbf{H}_1 & \\ & \mathbf{H}_1^\dagger & \mathbf{H}_0 & \mathbf{H}_1 \\ \mathbf{0} & & \ddots & \ddots & \ddots \end{pmatrix}. \quad (2.16)$$

In a similar way, the overlap inside the leads is given by the matrices

$$\mathbf{S}_L = \begin{pmatrix} \vdots & \vdots \\ \cdots & \mathbf{S}_{-2,-2} & \mathbf{S}_{-2,-1} \\ \cdots & \mathbf{S}_{-1,-2} & \mathbf{S}_{-1,-1} \end{pmatrix} = \begin{pmatrix} \ddots & \ddots & \ddots & \mathbf{0} \\ & \mathbf{S}_1^\dagger & \mathbf{S}_0 & \mathbf{S}_1 \\ & & \mathbf{S}_1^\dagger & \mathbf{S}_0 & \mathbf{S}_1 \\ \mathbf{0} & & & \mathbf{S}_1^\dagger & \mathbf{S}_0 \end{pmatrix} \quad (2.17)$$

and

$$\mathbf{S}_R = \begin{pmatrix} \mathbf{S}_{1,1} & \mathbf{S}_{1,2} & \cdots \\ \mathbf{S}_{2,1} & \mathbf{S}_{2,2} & \cdots \\ \vdots & \vdots & \ddots \end{pmatrix} = \begin{pmatrix} \mathbf{S}_0 & \mathbf{S}_1 & & \mathbf{0} \\ \mathbf{S}_1^\dagger & \mathbf{S}_0 & \mathbf{S}_1 & \\ & \mathbf{S}_1^\dagger & \mathbf{S}_0 & \mathbf{S}_1 \\ \mathbf{0} & & \ddots & \ddots & \ddots \end{pmatrix} \quad (2.18)$$

Furthermore the unit cell of each lead that is immediately connected to the scattering region (unit cell “ l ” for the left and unit cell “ r ” for the right lead) is included into the device part of the system.:

$$\mathbf{H}_D = \begin{pmatrix} \mathbf{H}_l & \mathbf{H}_{l,S} & \mathbf{0}_{l,r} \\ \mathbf{H}_{S,l} & \mathbf{H}_S & \mathbf{H}_{S,r} \\ \mathbf{0}_{r,l} & \mathbf{H}_{r,S} & \mathbf{H}_r \end{pmatrix} \text{ and } \mathbf{S}_D = \begin{pmatrix} \mathbf{S}_l & \mathbf{S}_{l,S} & \mathbf{0}_{l,r} \\ \mathbf{S}_{S,l} & \mathbf{S}_S & \mathbf{S}_{S,r} \\ \mathbf{0}_{r,l} & \mathbf{S}_{r,S} & \mathbf{S}_r \end{pmatrix}. \quad (2.19)$$

In the next subsection we will show how to calculate the GF for the device part of the system as defined by the above Hamilton and overlap matrices.

2.2.2 Green's function for the open system

The one-body GF operator $\hat{G}(E)$ of a system is defined as the solution to the generalized inhomogeneous Schrödinger equation (see e.g the book by E. N. Economou, Ref. [66]):

$$(z - \hat{H})\hat{G}(z) = \hat{1}, \quad (2.20)$$

where \hat{H} is an (effective) one-body Hamiltonian, and z is a complex number. When z does not coincide with the eigenvalues ϵ_k of the Hamiltonian \hat{H} , the GF operator has the following formal solution:

$$\hat{G}(z) = (z - \hat{H})^{-1} \text{ for } z \neq \epsilon_k. \quad (2.21)$$

Obviously, for $z = \epsilon_k$ the GF operator has a pole and is thus not well defined. In this case one can define two GFs which are both solutions to eq. (2.20) by a limiting process.

1) The *retarded* GF is defined as:

$$\hat{G}(E) := \lim_{\eta \rightarrow 0} (E + i\eta - \hat{H})^{-1}, \quad (2.22)$$

and 2) the *advanced* GF is defined as the hermitian conjugate of the *retarded* GF:

$$\hat{G}^\dagger(E) := \lim_{\eta \rightarrow 0} (E - i\eta - \hat{H})^{-1}. \quad (2.23)$$

E is a real number which can be any of the energy eigenvalues ϵ_k of the Hamiltonian \hat{H} . When E does not coincide with an eigenvalue of \hat{H} the two GFs reduce to the GF operator defined in eq. (2.21). In the basis of eigenstates of the Hamiltonian the GF operator becomes diagonal:

$$\hat{G}(z) = \sum_k \frac{|k\rangle\langle k|}{z - \epsilon_k} \text{ with } \hat{H}|k\rangle = \epsilon_k |k\rangle. \quad (2.24)$$

The GF yields the complete information of a one-body system. For example, eq. (2.24) makes clear that the poles of the GF along the real axis represent the eigenvalues of the

2 Quantum theory of electron transport

Hamiltonian \hat{H} . Thus by plotting $\hat{G}(E)$ along the real axis one can find all the eigenvalues in a certain energy range.

A very important quantity is the density of states (DOS) $\mathcal{D}(E)$. The DOS can be calculated from the trace of the imaginary part of the GF along the real axis:

$$\begin{aligned} \text{Im Tr}[\hat{G}(E)] &= \sum_k \lim_{\eta \rightarrow 0} \text{Im} \frac{1}{E + i\eta - \epsilon_k} = \\ &= \sum_k \lim_{\eta \rightarrow 0} \frac{-\eta}{(E - \epsilon_k)^2 + \eta^2} = -\pi \sum_k \delta(E - \epsilon_k) = -\pi \mathcal{D}(E). \end{aligned} \quad (2.25)$$

Another important quantity of the GF formalism is the *spectral density* $\hat{A}(z)$ which is defined as the difference between the *retarded* and the *advanced* GF:

$$\hat{A}(E) := i(\hat{G}(E) - \hat{G}^\dagger(E)). \quad (2.26)$$

It is straight forward to show that the eigenstate representation of the spectral function on the real axis is given by:

$$\hat{A}(E) := \sum_k \delta(E - \epsilon_k) |k\rangle \langle k|, \quad (2.27)$$

so that the trace of the spectral function directly gives the DOS. The spectral function can thus be seen as a generalized DOS.

The grand advantage of the GF formalism is that it allows one to calculate all properties of a one-body system without having to calculate the eigenstates of the Hamiltonian explicitly. Instead the GF can be calculated in any basis set by a matrix inversion for any value z , eq. (2.21). It turns out that in many situations this is more convenient than to solve the whole eigenvalue problem. This is the case for the transport problem defined by the Hamiltonian and overlap matrices given in the previous subsection, eqs. (2.13) and (2.14).

The matrix $\mathbf{G}_{\alpha\beta}(E) := \langle \alpha | \hat{G}(E) | \beta \rangle$ corresponding to the GF operator in a *non-orthogonal* basis set $\{|\alpha\rangle\}$ is given by:

$$(E\mathbf{S} - \mathbf{H})\mathbf{S}^{-1}\mathbf{G}(E) = \mathbf{S}, \quad (2.28)$$

where \mathbf{S} is the overlap matrix of the NOBS: $S_{\alpha\beta} = \langle \alpha | \beta \rangle$. This, however, is a somewhat inconvenient definition for the calculation of the GF since it involves the inversion of the \mathbf{S} matrix. Instead, we define a new GF matrix $\tilde{\mathbf{G}}(E)$ by

$$\tilde{\mathbf{G}}(E) := \mathbf{S}^{-1}\mathbf{G}(E)\mathbf{S}^{-1}. \quad (2.29)$$

This GF can be calculated more conveniently from the much simpler equation

$$(E\mathbf{S} - \mathbf{H})\tilde{\mathbf{G}}(E) = \mathbf{1}. \quad (2.30)$$

For convenience we introduce the following energy-dependent matrix:

$$\mathbf{W}(E) := \mathbf{H} - E\mathbf{S} = \begin{pmatrix} \mathbf{H}_L - E\mathbf{S}_L & \mathbf{H}_{LD} - E\mathbf{S}_{LD} & \mathbf{0} \\ \mathbf{H}_{DL} - E\mathbf{S}_{DL} & \mathbf{H}_D - E\mathbf{S}_D & \mathbf{H}_{DR} - E\mathbf{S}_{DR} \\ \mathbf{0} & \mathbf{H}_{RD} - E\mathbf{S}_{RD} & \mathbf{H}_R - E\mathbf{H}_R \end{pmatrix}. \quad (2.31)$$

Thus we obtain for the GF for the transport problem the following matrix equation which defines a system of equations for each sub-matrix of the total GF.

$$\begin{aligned}
 & - \begin{pmatrix} \mathbf{W}_L(E) & \mathbf{W}_{LD}(E) & \mathbf{W}_{LR}(E) \\ \mathbf{W}_{DL}(E) & \mathbf{W}_D(E) & \mathbf{W}_{DR}(E) \\ \mathbf{W}_{RL}(E) & \mathbf{W}_{RD}(E) & \mathbf{W}_R(E) \end{pmatrix} \times \\
 & \times \begin{pmatrix} \tilde{\mathbf{G}}_L(E) & \tilde{\mathbf{G}}_{LD}(E) & \tilde{\mathbf{G}}_{LR}(E) \\ \tilde{\mathbf{G}}_{DL}(E) & \tilde{\mathbf{G}}_D(E) & \tilde{\mathbf{G}}_{DR}(E) \\ \tilde{\mathbf{G}}_{RL}(E) & \tilde{\mathbf{G}}_{RD}(E) & \tilde{\mathbf{G}}_R(E) \end{pmatrix} = \begin{pmatrix} \mathbf{1} & \mathbf{0} & \mathbf{0} \\ \mathbf{0} & \mathbf{1} & \mathbf{0} \\ \mathbf{0} & \mathbf{0} & \mathbf{1} \end{pmatrix}, \quad (2.32)
 \end{aligned}$$

This matrix equation can be solved for each of the matrix elements (see App. B). For the device part of the GF $\tilde{\mathbf{G}}_D$ we obtain:

$$\tilde{\mathbf{G}}_D(E) = (E\mathbf{S}_D - \mathbf{H}_D - \tilde{\mathbf{\Sigma}}_L(E) - \tilde{\mathbf{\Sigma}}_R(E))^{-1}, \quad (2.33)$$

where we have introduced the *self-energies* of the leads $\tilde{\mathbf{\Sigma}}_L$ and $\tilde{\mathbf{\Sigma}}_R$ which describe the influence of the leads on the electronic structure of the device. They can be calculated from the GFs of the *isolated* left and right semi-infinite lead, $\mathbf{g}_L(E) = (E\mathbf{S}_L - \mathbf{H}_L)^{-1}$ and $\mathbf{g}_R(E) = (E\mathbf{S}_R - \mathbf{H}_R)^{-1}$, respectively:

$$\tilde{\mathbf{\Sigma}}_L(E) = \mathbf{W}_{DL}(E) \tilde{\mathbf{g}}_L(E) \mathbf{W}_{LD}(E) \quad (2.34)$$

$$\tilde{\mathbf{\Sigma}}_R(E) = \mathbf{W}_{DR}(E) \tilde{\mathbf{g}}_R(E) \mathbf{W}_{RD}(E) \quad (2.35)$$

For later use, we also define the so-called coupling matrices:

$$\begin{aligned}
 \tilde{\mathbf{\Gamma}}_L(E) & := i \left(\tilde{\mathbf{\Sigma}}_L(E) - \tilde{\mathbf{\Sigma}}_L^\dagger(E) \right) \\
 & = i \mathbf{W}_{DL}(E) (\tilde{\mathbf{g}}_L(E) - \tilde{\mathbf{g}}_L^\dagger(E)) \mathbf{W}_{LD}(E), \quad (2.36)
 \end{aligned}$$

$$\begin{aligned}
 \tilde{\mathbf{\Gamma}}_R(E) & := i \left(\tilde{\mathbf{\Sigma}}_R(E) - \tilde{\mathbf{\Sigma}}_R^\dagger(E) \right) \\
 & = i \mathbf{W}_{DR}(E) (\tilde{\mathbf{g}}_R(E) - \tilde{\mathbf{g}}_R^\dagger(E)) \mathbf{W}_{RD}(E). \quad (2.37)
 \end{aligned}$$

Thus we have expressed the GF of the device region in terms of the device Hamiltonian and the Green's functions of the *isolated* leads. The term $\mathbf{H}_D + \tilde{\mathbf{\Sigma}}_L(E) + \tilde{\mathbf{\Sigma}}_R(E)$ can be interpreted as an effective Hamiltonian for the device region, and its energy dependence stems from the fact, that the lifetime of an electron in the device region is now finite due to the coupling to the leads. The technique of calculating the GF in parts by dividing the underlying Hilbert space into subspaces is called *partitioning technique* and is shown in more detail in App. B where we also list the other matrix elements of the GF.

Since the coupling \mathbf{H}_{DL} between the left lead and the device is only due to coupling between the last unit cell (-1) of left lead and the unit cell l included in the device region, only the surface GF of the left lead, i.e. the GF projected into the unit cell -1 , is necessary for calculating the self-energy $\tilde{\mathbf{\Sigma}}_L$. The same holds true for the right lead in an analogous manner. Furthermore, $\tilde{\mathbf{\Sigma}}_L$ is different from zero only in the l -region of the device, and analogously $\tilde{\mathbf{\Sigma}}_R$ in the r -region:

$$\tilde{\mathbf{\Sigma}} := \tilde{\mathbf{\Sigma}}_L + \tilde{\mathbf{\Sigma}}_R = \begin{pmatrix} \tilde{\mathbf{\Sigma}}_l & \mathbf{0}_{l,S} & \mathbf{0}_{l,r} \\ \mathbf{0}_{S,l} & \mathbf{0}_S & \mathbf{0}_{S,r} \\ \mathbf{0}_{r,l} & \mathbf{0}_{r,S} & \tilde{\mathbf{\Sigma}}_r \end{pmatrix}, \quad (2.38)$$

2 Quantum theory of electron transport

where the non-zero matrix elements $\tilde{\Sigma}_l$ and $\tilde{\Sigma}_r$ of $\tilde{\Sigma}$ can be expressed in terms of the surface GFs of the left and right lead, $\tilde{\mathbf{g}}_{-1,-1}$ and $\tilde{\mathbf{g}}_{+1,+1}$:

$$\tilde{\Sigma}_l(E) = (\mathbf{H}_1^\dagger - E\mathbf{S}_1^\dagger)\tilde{\mathbf{g}}_{-1,-1}(E)(\mathbf{H}_1 - E\mathbf{S}_1), \quad (2.39)$$

$$\tilde{\Sigma}_r(E) = (\mathbf{H}_1 - E\mathbf{S}_1)\tilde{\mathbf{g}}_{+1,+1}(E)(\mathbf{H}_1^\dagger - E\mathbf{S}_1^\dagger). \quad (2.40)$$

The self-energies can be calculated iteratively by Dyson equations, as shown in App. C:

$$\tilde{\Sigma}_l(E) = (\mathbf{H}_1^\dagger - E\mathbf{S}_1^\dagger)(E\mathbf{S}_0 - \mathbf{H}_0 - \tilde{\Sigma}_l(E))^{-1}(\mathbf{H}_1 - E\mathbf{S}_1), \quad (2.41)$$

$$\tilde{\Sigma}_r(E) = (\mathbf{H}_1 - E\mathbf{S}_1)(E\mathbf{S}_0 - \mathbf{H}_0 - \tilde{\Sigma}_r(E))^{-1}(\mathbf{H}_1^\dagger - E\mathbf{S}_1^\dagger). \quad (2.42)$$

Now we have achieved a description of the electronic structure of the device region in terms of one-body GFs which take into account the effect of the coupling of the leads to the device region. In the next section we will show how to obtain the (reduced) density matrix and subsequently the electron density of the device region from this GF. Thereafter we demonstrate, how to calculate the transmission matrix from the GF of the device region and the self-energies of the leads.

2.2.3 Calculation of density matrix and electron number at equilibrium

The reduced density matrix of first order (in quantum chemistry often called charge density matrix) is obtained by tracing out all but one of the one-particle subspaces from the many-body density matrix $\hat{\rho}$:

$$\hat{P} = N \times \sum_{n_2, \dots, n_N} \langle n, n_2, \dots, n_N | \hat{\rho} | n', n_2, \dots, n_N \rangle | n \rangle \langle n' |, \quad (2.43)$$

where $\{|n\rangle\}$ is a set of one-body states.

At zero temperature the system will be in its (many-body) ground state Ψ , so that the density matrix becomes

$$\hat{\rho}_\Psi = |\Psi\rangle\langle\Psi|. \quad (2.44)$$

It is straight forward to show that in this case the reduced density matrix can be expressed as

$$\hat{P} = \sum_{k,l} |k\rangle \langle\Psi| \hat{c}_k^\dagger \hat{c}_l |\Psi\rangle \langle l|. \quad (2.45)$$

One can obtain a lot of information from the reduced density matrix about a many-body system in spite of the fact that it is actually a one-body operator. For example, one can calculate the expectation value of any one-body observable from the trace of the product of the reduced density matrix and the observable:

$$\langle \hat{A} \rangle = \text{Tr}[\hat{P}\hat{A}]. \quad (2.46)$$

The electron density is given by the diagonal elements of the reduced density matrix in the real space representation:

$$n(\vec{r}) = \langle \vec{r} | \hat{P} | \vec{r} \rangle. \quad (2.47)$$

Finally, the number of electrons is the trace of the density matrix.

In the Landauer approach we consider the electrons as a system of non-interacting quasi-particles, i.e. the Coulomb interaction between the electrons is only taken into account on the mean-field level. In the case of a system of non-interacting particles the many-body ground state of the system $|\Psi\rangle$ is given by a single Slater determinant:

$$|\Psi\rangle = \prod_{k, \epsilon_k \leq \mu} \hat{c}_k^\dagger |0\rangle, \quad (2.48)$$

where $|k\rangle$ are the eigenstates of the one-body Hamiltonian, $|0\rangle$ is the vacuum ground state, and μ the chemical potential, so that the Slater determinant consists of all states with energies less than or equal to the chemical potential. In this case the reduced density matrix is diagonal in the one-body eigenstates $|k\rangle$:

$$\hat{P} = \sum_k n_k |k\rangle\langle k|, \quad (2.49)$$

where the occupation number n_k of the eigenstate $|k\rangle$ is given by the Fermi distribution function, $n_k = f(\epsilon_k - \mu)$, and thus is either one for states below the chemical potential or zero for states above the chemical potential at zero temperature. Since we will make use of the *reduced* density matrix only but not of the full many-body density matrix we will refer to the *reduced* density matrix for the sake of simplicity from here on simply as the density matrix, unless otherwise stated.

Using the eigenstate representation of the GF, eq. (2.24), it is straight forward to show that the density matrix can actually be obtained from the GF of the system by integrating the imaginary part of the GF up to the chemical potential μ of the system:

$$\begin{aligned} -\frac{1}{\pi} \text{Im} \int_{-\infty}^{\mu} dE \hat{\mathbf{G}}(E) &= \lim_{\eta \rightarrow 0} -\frac{1}{\pi} \int_{-\infty}^{\mu} dE \text{Im} \sum_k \frac{|k\rangle\langle k|}{E - \epsilon_k + i\eta} \\ &= \sum_k \int_{-\infty}^{\mu} dE \lim_{\eta \rightarrow 0} \frac{1}{\pi} \frac{\eta}{(E - \epsilon_k)^2 + \eta^2} |k\rangle\langle k| = \sum_k \int_{-\infty}^{\mu} dE \delta(E - \epsilon_k) |k\rangle\langle k| \\ &= \sum_k f(\epsilon_k - \mu) |k\rangle\langle k| \equiv \hat{P}. \end{aligned} \quad (2.50)$$

Subsequently, the (standard) density matrix in a NOBS $\{|\alpha\rangle\}$, is obtained by integration of the standard non-orthogonal GF matrix, $G_{\alpha\beta}(E) := \langle \alpha | \hat{\mathbf{G}}(E) | \beta \rangle$:

$$P_{\alpha\beta} := \langle \alpha | \hat{P} | \beta \rangle = -\frac{1}{\pi} \text{Im} \int_{-\infty}^{\mu} dE G_{\alpha\beta}(E). \quad (2.51)$$

Analogously to the GF matrix $\tilde{\mathbf{G}}$ we can define a new density matrix by

$$\tilde{\mathbf{P}} = \mathbf{S}^{-1} \mathbf{P} \mathbf{S}^{-1}, \quad (2.52)$$

which is thus obtained by integration of the non-standard GF $\tilde{\mathbf{G}}(E)$:

$$\tilde{\mathbf{P}} = -\frac{1}{\pi} \text{Im} \int_{-\infty}^{\mu} dE \tilde{\mathbf{G}}(E). \quad (2.53)$$

2 Quantum theory of electron transport

One can obtain the number of electrons from the trace of the density matrix. However, the trace of an operator has to be taken in an orthogonal basis set, but $\tilde{\mathbf{P}}$ has been defined in terms of the density matrix in a NOBS $\{|\alpha\rangle\}$. The standard procedure for orthogonalizing atomic orbitals is the so-called *symmetric orthogonalization* [70]. A density matrix \mathbf{P} in a NOBS will be transformed to the density matrix \mathbf{P}^\perp in the orthogonalized basis according to:

$$\mathbf{P}^\perp = \mathbf{S}^{-1/2} \mathbf{P} \mathbf{S}^{-1/2} = \mathbf{S}^{+1/2} \tilde{\mathbf{P}} \mathbf{S}^{+1/2}. \quad (2.54)$$

In the last step we have used the definition of the non-standard density matrix $\tilde{\mathbf{P}}$ to obtain the transformation to the orthogonalized density matrix.

Applying the above transformation for the density matrix $\tilde{\mathbf{P}}$ we find for the number of electrons the following expression:

$$\begin{aligned} N_e &= \text{Tr}[\mathbf{S}^{1/2} \tilde{\mathbf{P}} \mathbf{S}^{1/2}] = \text{Tr}[\tilde{\mathbf{P}} \mathbf{S}] = \text{Tr}[\tilde{\mathbf{P}}_D \mathbf{S}_D] + \text{Tr}[\tilde{\mathbf{P}}_{DL} \mathbf{S}_{LD}] + \text{Tr}[\tilde{\mathbf{P}}_{DR} \mathbf{S}_{RD}] \\ &+ \text{Tr}[\tilde{\mathbf{P}}_L \mathbf{S}_L] + \text{Tr}[\tilde{\mathbf{P}}_{LD} \mathbf{S}_{DL}] + \text{Tr}[\tilde{\mathbf{P}}_R \mathbf{S}_R] + \text{Tr}[\tilde{\mathbf{P}}_{RD} \mathbf{S}_{DR}] \end{aligned} \quad (2.55)$$

where we have first exploited the invariance of the trace under commutation of matrices and then applied the above explained division into sub-matrices of the density matrix and the expression (2.14) for the overlap matrix. In analogy to the Mulliken analysis we can identify the number of electrons in the device, N_D , in the left lead, N_L , and in the right lead N_R as follows:

$$\begin{aligned} N_D &= \text{Tr}[\tilde{\mathbf{P}}_D \mathbf{S}_D] + \text{Tr}[\tilde{\mathbf{P}}_{DL} \mathbf{S}_{LD}] + \text{Tr}[\tilde{\mathbf{P}}_{DR} \mathbf{S}_{RD}] \\ N_L &= \text{Tr}[\tilde{\mathbf{P}}_L \mathbf{S}_L] + \text{Tr}[\tilde{\mathbf{P}}_{LD} \mathbf{S}_{DL}] \\ N_R &= \text{Tr}[\tilde{\mathbf{P}}_R \mathbf{S}_R] + \text{Tr}[\tilde{\mathbf{P}}_{RD} \mathbf{S}_{DR}] \end{aligned} \quad (2.56)$$

Thus due to the overlap of the device orbitals with the lead orbitals one also has to calculate the off-diagonal elements DL and DR of the density matrix $\tilde{\mathbf{P}}$ in order to calculate the number of electrons in the device part. However, computing the off-diagonal elements of the density matrix would require calculation of the corresponding off-diagonal elements of the GF matrix $\tilde{\mathbf{G}}(E)$ in terms of the GF matrix of the device and the self-energies (see App. B) which are quite tedious expressions. Instead we will require charge neutrality only for the scattering region and not for the entire device region. That is the reason why we have included one unit cell of each lead into the device region in addition to the scattering region. Since the scattering region does not have an overlap with the two leads it is sufficient to calculate the density matrix of the device region to obtain the number of electrons inside the scattering region:

$$N_S = \text{Tr}_S[\tilde{\mathbf{P}}_D \mathbf{S}_D] = \sum_{\alpha \in S, \beta \in D} \tilde{P}_{\alpha\beta} S_{\beta\alpha} \quad (2.57)$$

Finally, we also have to define an appropriate DOS \mathcal{D} and projected DOS (PDOS) \mathcal{D}_i for the case of non-orthogonal orbitals. In order to be coherent with the above definition of the electron numbers in the respective subspaces of the leads and the device, it is best to adapt a similar Mulliken-like definition for the PDOS:

$$\mathcal{D}_\alpha(E) = -\frac{1}{\pi} \text{Im}(\tilde{\mathbf{G}}(E) \mathbf{S})_{\alpha\alpha} \quad (2.58)$$

where α denotes some of the atomic orbitals of the system. If we are interested in the DOS projected onto some orbital α of the scattering region, it suffices to calculate the GF and overlap matrix for the device region instead for the entire system, $\mathcal{D}_\alpha(E) = -\frac{1}{\pi}\text{Im}(\tilde{\mathbf{G}}_D(E)\mathbf{S}_D)_{\alpha\alpha}$. And the DOS projected onto the entire scattering region is just $\mathcal{D}_S(E) = -\frac{1}{\pi}\sum_{\alpha\in S}\text{Im}(\tilde{\mathbf{G}}_D(E)\mathbf{S}_D)_{\alpha\alpha}$.

2.2.4 Non-equilibrium density matrix

In the previous section we have assumed that the system is in thermal equilibrium, i.e. the chemical potentials of the two electron reservoirs are equal: $\mu_L = \mu_R = \mu$. Although in many cases one can estimate the conductance at small bias from the zero-bias conductance, i.e. in equilibrium, it would be very interesting to study the interplay between an electron current and the electronic structure of the nanoscopic conductor. Thus we have to derive an expression for the density matrix when the system is out of equilibrium, i.e. $\mu_L \neq \mu_R$.

First, we calculate the response $|\psi^+\rangle$ of the entire system to an incoming wave on the left lead $|\psi^i\rangle$ which we assume is a solution of the *isolated* left lead, i.e. $\hat{H}_L|\psi^i\rangle = E|\psi^i\rangle$.

$$\hat{H}(|\psi^+\rangle + |\psi^i\rangle) = E(|\psi^+\rangle + |\psi^i\rangle) \quad (2.59)$$

Because of the non-orthogonality of the lead orbitals with the device orbitals we now switch to a matrix presentation of the problem as done in the previous section. The incoming wave as a solution of the left isolated lead is given as an expansion over the lead orbitals:

$$|\psi^i\rangle = \sum_{\alpha\in L}\psi_\alpha^i|\alpha\rangle \Leftrightarrow \vec{\psi}^i = \begin{pmatrix} \vec{\psi}_L^i \\ \vec{0}_D \\ \vec{0}_R \end{pmatrix} \quad (2.60)$$

The response wave function $|\psi^+\rangle$ on the other hand expands over the whole system:

$$\vec{\psi}^+ = \begin{pmatrix} \vec{\psi}_L^+ \\ \vec{\psi}_D^+ \\ \vec{\psi}_R^+ \end{pmatrix} \quad (2.61)$$

Thus in matrix representation the above Schrödinger equation for the response to an incoming wave reads:

$$\begin{aligned} \mathbf{H}(\vec{\psi}^+ + \vec{\psi}^i) &= E\mathbf{S}(\vec{\psi}^+ + \vec{\psi}^i) \\ \Rightarrow (\mathbf{H} - E\mathbf{S})\vec{\psi}^+ &= (E\mathbf{S} - \mathbf{H})\vec{\psi}^i = \begin{pmatrix} (E\mathbf{S}_L - \mathbf{H}_L)\vec{\psi}_L^i \\ (E\mathbf{S}_{DL} - \mathbf{H}_{DL})\vec{\psi}_L^i \\ \vec{0}_R \end{pmatrix} \\ \Rightarrow \begin{pmatrix} \vec{\psi}_L^+ \\ \vec{\psi}_D^+ \\ \vec{\psi}_R^+ \end{pmatrix} &= -\tilde{\mathbf{G}}(E) \begin{pmatrix} (E\mathbf{S}_L - \mathbf{H}_L)\vec{\psi}_L^i \\ (E\mathbf{S}_{DL} - \mathbf{H}_{DL})\vec{\psi}_L^i \\ \vec{0}_R \end{pmatrix}. \end{aligned} \quad (2.62)$$

Since $|\psi^i\rangle$ is a solution for the isolated left lead,

$$\mathbf{H}_L\vec{\psi}_L^i = E\mathbf{S}_L\vec{\psi}_L^i \Rightarrow (\mathbf{H}_L - E\mathbf{S}_L)\vec{\psi}_L^i = 0 \quad (2.63)$$

2 Quantum theory of electron transport

we obtain finally:

$$\begin{pmatrix} \vec{\psi}_L^+ \\ \vec{\psi}_D^+ \\ \vec{\psi}_R^+ \end{pmatrix} = -\tilde{\mathbf{G}}(E) \begin{pmatrix} \vec{0}_L \\ (\mathbf{E}\mathbf{S}_{DL} - \mathbf{H}_{DL})\vec{\psi}_L^i \\ \vec{0}_R \end{pmatrix} = \begin{pmatrix} \tilde{\mathbf{G}}_{LD}(E) \\ \tilde{\mathbf{G}}_D(E) \\ \tilde{\mathbf{G}}_{RD}(E) \end{pmatrix} \mathbf{W}_{DL}(E) \vec{\psi}_L^i \quad (2.64)$$

The left electron reservoir fills the incoming electron waves $|\psi_{L,n}(k)\rangle$ on the left lead up to the chemical potential μ_L of that reservoir which result in wavefunctions expanded over the whole system $|\Psi_n(k)\rangle = |\psi_n^+(k)\rangle + |\psi_{L,n}(k)\rangle$. Thus the density matrix due to injection of electrons from the left reservoir is given by:

$$\begin{aligned} \hat{P}^{(L)} &= \sum_{n \in N_L, k} f(\epsilon_{L,n}(k) - \mu_L) |\Psi_n(k)\rangle \langle \Psi_n(k)| \\ &= \sum_{n \in N_L, k} \int dE \delta(E - \epsilon_{L,n}(k)) f(E - \mu_L) |\Psi_n(k)\rangle \langle \Psi_n(k)| \\ &= \int dE f(E - \mu_L) \sum_{n \in N_L, k} |\Psi_n(k)\rangle \delta(E - \epsilon_{L,n}(k)) \langle \Psi_n(k)| \end{aligned} \quad (2.65)$$

In matrix representation this density matrix is given as

$$P_{\alpha\beta}^{(L)} = \langle \alpha | \hat{P}^{(L)} | \beta \rangle = \sum_{n \in N_L, k} f(\epsilon_{L,n}(k) - \mu_L) S_{\alpha\alpha'} \tilde{\Psi}_{n\alpha'}(k) \Psi_{n\beta'}(k)^* S_{\beta'\beta} \quad (2.66)$$

Thus the non-standard matrix representation is

$$\tilde{\mathbf{P}}^{(L)} = \mathbf{S}^{-1} \mathbf{P} \mathbf{S}^{-1} = \int dE f(E - \mu_L) \sum_{n \in N_L, k} \tilde{\Psi}_n(k) \delta(E - \epsilon_{L,n}(k)) [\tilde{\Psi}_n(k)]^\dagger. \quad (2.67)$$

From eq. (2.64) we see that the device part is given by

$$\begin{aligned} \tilde{\mathbf{P}}_D^{(L)} &= \int dE f(E - \mu_L) \sum_{n \in N_L, k} \tilde{\Psi}_{D,n}(k) \delta(E - \epsilon_{L,n}(k)) [\tilde{\Psi}_{D,n}(k)]^\dagger \\ &= \int dE f(E - \mu_L) \tilde{\mathbf{G}}_D(E) \mathbf{W}_{DL}(E) \\ &\quad \underbrace{\sum_{n \in N_L, k} \vec{\psi}_{L,n}(k) \delta(E - \epsilon_{L,n}(k)) [\vec{\psi}_{L,n}(k)]^\dagger \mathbf{W}_{LD}(E) \tilde{\mathbf{G}}_D^\dagger(E)}_{\tilde{\mathbf{a}}_L(E)/2\pi = i(\tilde{\mathbf{g}}_L(E) - \tilde{\mathbf{g}}_L^\dagger(E))/2\pi} \\ &= \frac{i}{2\pi} \int dE f(E - \mu_L) \tilde{\mathbf{G}}_D(E) \underbrace{(\tilde{\mathbf{\Sigma}}_L(E) - \tilde{\mathbf{\Sigma}}_L^\dagger(E))}_{\tilde{\mathbf{\Gamma}}_L(E)/i} \tilde{\mathbf{G}}_D^\dagger(E), \end{aligned} \quad (2.68)$$

where in the 2nd step we have made use of the spectral density of the isolated left lead, $\tilde{\mathbf{a}}_L(E) = i(\tilde{\mathbf{g}}_L(E) - \tilde{\mathbf{g}}_L^\dagger(E))$.

For the injection of electrons from the right we obtain an analogous expression. Summing up both contributions we obtain the density matrix out of equilibrium:

$$\tilde{\mathbf{P}}_D^{neq} = \tilde{\mathbf{P}}_D^{(L)} + \tilde{\mathbf{P}}_D^{(R)} = \frac{1}{2\pi} \int dE \tilde{\mathbf{G}}_D(E) [f(E - \mu_L) \tilde{\mathbf{\Gamma}}_L(E) + f(E - \mu_R) \tilde{\mathbf{\Gamma}}_R(E)] \tilde{\mathbf{G}}_D^\dagger(E) \quad (2.69)$$

Finally, we define the non-equilibrium GF matrix $\tilde{\mathbf{G}}^<(E)$ of the device as:

$$\tilde{\mathbf{G}}^<(E) := i\tilde{\mathbf{G}}_D(E)[f(E - \mu_L)\tilde{\mathbf{\Gamma}}_L(E) + f(E - \mu_R)\tilde{\mathbf{\Gamma}}_R(E)]\tilde{\mathbf{G}}_D^\dagger(E) \quad (2.70)$$

Then the non-equilibrium density matrix can be written as:

$$\tilde{\mathbf{P}}_D^{neq} = -\frac{i}{2\pi} \int dE \tilde{\mathbf{G}}^<(E) \quad (2.71)$$

In equilibrium, i.e. when $\mu_L = \mu_R = \mu$, the GF matrix $\tilde{\mathbf{G}}^<(E)$ reduces to the imaginary part of the retarded GF matrix:

$$\begin{aligned} \tilde{\mathbf{G}}^<(E) &= f(E - \mu) i\tilde{\mathbf{G}}_D(E)[\tilde{\mathbf{\Gamma}}_L(E) + \tilde{\mathbf{\Gamma}}_R(E)]\tilde{\mathbf{G}}_D^\dagger(E) \\ &= f(E - \mu) \tilde{\mathbf{G}}_D(E)[(\tilde{\mathbf{G}}_D(E))^{-1} - (\tilde{\mathbf{G}}_D^\dagger(E))^{-1}]\tilde{\mathbf{G}}_D^\dagger(E) \\ &= f(E - \mu)[\tilde{\mathbf{G}}_D^\dagger(E) - \tilde{\mathbf{G}}_D(E)] = -2i f(E - \mu) \text{Im}[\tilde{\mathbf{G}}_D(E)], \end{aligned} \quad (2.72)$$

and one arrives again at the expression for the equilibrium density matrix derived before:

$$\tilde{\mathbf{P}} = -\frac{1}{\pi} \int dE f(E - \mu) \text{Im}[\tilde{\mathbf{G}}_D(E)]. \quad (2.73)$$

The same reasoning shows that for an out of equilibrium situation the density matrix can be calculated using the much simpler expression (2.73) for the energy integration up to the lowest of the two chemical potentials, e.g. for $\mu_L > \mu_R$ we have:

$$\tilde{\mathbf{P}}_D^{neq} = -\frac{1}{\pi} \int_{-\infty}^{\mu_R} dE \text{Im}[\tilde{\mathbf{G}}_D(E)] - \frac{i}{2\pi} \int_{\mu_R}^{\mu_L} dE \tilde{\mathbf{G}}^<(E). \quad (2.74)$$

2.2.5 Current and transmission

Now we derive an expression for the electrical current through the device region in terms of the GFs by calculating the time derivative of the electron charge in the device region. The temporal change of the number of electrons inside the device region is equal to the sum of the currents from the left and from the right lead:

$$\frac{\partial N_D}{\partial t} = \text{Tr}_D \left[\frac{\partial \tilde{\mathbf{P}}}{\partial t} \mathbf{S} \right] = I_L + I_R, \quad (2.75)$$

where we have taken a current as positive when it increases the number of electrons inside the device region, i.e. when the current flows from the leads to the device. Typically we are interested in steady-state situations, so that the electron charge of the device will be conserved, meaning that $I_L = -I_R$. Then the net current I through the device is given by $I \equiv I_L = -I_R$.

We will now derive an expression for the total current into the device $\frac{\partial N_D}{\partial t} = I_L + I_R$ by taking the time derivative of the density matrix $\tilde{\mathbf{P}}$, and divide the obtained expression for the total current $I_L + I_R$ into the device into its individual contributions I_L and I_R . We start from the expression (2.67) in order to calculate the net current through the device

2 Quantum theory of electron transport

due to the injection of electrons from the left electrode:

$$\begin{aligned} \frac{\partial \tilde{\mathbf{N}}_D^{(L)}}{\partial t} := \text{Tr}_D \left[\frac{\partial \tilde{\mathbf{P}}^{(L)}}{\partial t} \mathbf{S} \right] &= \int dE f(E - \mu_L) \sum_{n \in N_{L,k}} \delta(E - \epsilon_{L,n}(k)) \times \\ &\times \text{Tr}_D \left[\mathbf{S} \frac{\partial \tilde{\Psi}_n(k)}{\partial t} [\tilde{\Psi}_n(k)]^\dagger + \tilde{\Psi}_n(k) \frac{\partial [\tilde{\Psi}_n(k)]^\dagger}{\partial t} \mathbf{S} \right]. \end{aligned} \quad (2.76)$$

For the first term of the trace we find:

$$\begin{aligned} \text{Tr}_D \left[\mathbf{S} \frac{\partial \tilde{\Psi}_n(k)}{\partial t} [\tilde{\Psi}_n(k)]^\dagger \right] &= \frac{1}{i\hbar} \text{Tr}_D \left[\mathbf{H} \tilde{\Psi}_n(k) [\tilde{\Psi}_n(k)]^\dagger \right] \\ &= \frac{1}{i\hbar} \text{Tr} \left[\mathbf{H}_{DL} [\tilde{\Psi}_n(k)]_L [\tilde{\Psi}_n(k)]_D^\dagger + \mathbf{H}_D [\tilde{\Psi}_n(k)]_D [\tilde{\Psi}_n(k)]_D^\dagger + \mathbf{H}_{DR} [\tilde{\Psi}_n(k)]_R [\tilde{\Psi}_n(k)]_D^\dagger \right] \end{aligned} \quad (2.77)$$

where we have made use of the invariance of the trace under cyclic permutations and the fact that $\tilde{\Psi}_n(k)$ is an eigenstate of the system, so that $i\hbar \mathbf{S} \frac{\partial \tilde{\Psi}_n(k)}{\partial t} = \mathbf{H} \tilde{\Psi}_n(k)$.

Analogously, we find for the second term of the trace (2.76):

$$\begin{aligned} \text{Tr}_D \left[\tilde{\Psi}_n(k) \frac{\partial [\tilde{\Psi}_n(k)]^\dagger}{\partial t} \mathbf{S} \right] &= -\frac{1}{i\hbar} \text{Tr}_D \left[\tilde{\Psi}_n(k) [\tilde{\Psi}_n(k)]^\dagger \mathbf{H} \right] \\ &= -\frac{1}{i\hbar} \text{Tr} \left[[\tilde{\Psi}_n(k)]_D [\tilde{\Psi}_n(k)]_L^\dagger \mathbf{H}_{LD} + [\tilde{\Psi}_n(k)]_D [\tilde{\Psi}_n(k)]_D^\dagger \mathbf{H}_D + [\tilde{\Psi}_n(k)]_D [\tilde{\Psi}_n(k)]_R^\dagger \mathbf{H}_{RD} \right] \end{aligned} \quad (2.78)$$

When adding up the two contributions to the trace in (2.76), the term involving \mathbf{H}_D in (2.77) cancels with the term involving \mathbf{H}_D in (2.78). For later convenience we add the following term which is equal to zero to the trace:

$$\begin{aligned} 0 &= \frac{1}{i\hbar} \text{Tr}_D \left[E_n(k) \mathbf{S} \tilde{\Psi}_n(k) [\tilde{\Psi}_n(k)]^\dagger \right] - \frac{1}{i\hbar} \text{Tr}_D \left[\tilde{\Psi}_n(k) [\tilde{\Psi}_n(k)]^\dagger E_n(k) \mathbf{S} \right] \\ &= \frac{1}{i\hbar} \text{Tr} \left[E_n(k) \mathbf{S}_{DL} [\tilde{\Psi}_n(k)]_L [\tilde{\Psi}_n(k)]_D^\dagger \right] + \frac{1}{i\hbar} \text{Tr} \left[E_n(k) \mathbf{S}_{DR} [\tilde{\Psi}_n(k)]_R [\tilde{\Psi}_n(k)]_D^\dagger \right] \\ &\quad - \frac{1}{i\hbar} \text{Tr} \left[[\tilde{\Psi}_n(k)]_D [\tilde{\Psi}_n(k)]_L^\dagger E_n(k) \mathbf{S}_{LD} \right] - \frac{1}{i\hbar} \text{Tr} \left[[\tilde{\Psi}_n(k)]_D [\tilde{\Psi}_n(k)]_R^\dagger E_n(k) \mathbf{S}_{RD} \right], \end{aligned}$$

where the two terms involving S_D have canceled out each other. Summing up all contributions to the trace in (2.76) and grouping together on the one hand terms involving hopping between the left electrode and the device and on the other hand terms involving hopping between the right electrode and the device, we get in total:

$$\text{Tr}_D \left[\mathbf{S} \frac{\partial \tilde{\Psi}_n(k)}{\partial t} [\tilde{\Psi}_n(k)]^\dagger + \tilde{\Psi}_n(k) \frac{\partial [\tilde{\Psi}_n(k)]^\dagger}{\partial t} \mathbf{S} \right] = j_{L,n}(k) + j_{R,n}(k) \quad (2.79)$$

where

$$j_{L,n}(k) := \frac{1}{i\hbar} \text{Tr} \left[[\tilde{\Psi}_n(k)]_D^\dagger \mathbf{W}_{DL}(E_n(k)) [\tilde{\Psi}_n(k)]_L - [\tilde{\Psi}_n(k)]_L^\dagger \mathbf{W}_{LD}(E_n(k)) [\tilde{\Psi}_n(k)]_D \right],$$

and

$$j_{R,n}(k) := \frac{1}{i\hbar} \text{Tr} \left[[\vec{\Psi}_n(k)]_D^\dagger \mathbf{W}_{DR}(E_n(k)) [\vec{\Psi}_n(k)]_R - [\vec{\Psi}_n(k)]_R^\dagger \mathbf{W}_{RD}(E_n(k)) [\vec{\Psi}_n(k)]_D \right].$$

The term $j_{L,n}(k)$ gives the current coming from the left lead, while $j_{R,n}(k)$ gives the current coming from the right electrode. We proceed by expressing the states $|\Psi_n(k)\rangle$ in terms of the incoming waves $|\Psi_n^i(k)\rangle$ by the help of expression (2.64) for the response to an incoming wave:

$$[\vec{\Psi}_n(k)]_D = \tilde{\mathbf{G}}_D(E) \mathbf{W}_{DL}(E) [\vec{\Psi}_n^i(k)] \quad (2.80)$$

$$\Rightarrow [\vec{\Psi}_n(k)]_D^\dagger = [\vec{\Psi}_n^i(k)]^\dagger \mathbf{W}_{LD}(E) \tilde{\mathbf{G}}_D^\dagger(E) \quad (2.81)$$

$$\begin{aligned} [\vec{\Psi}_n(k)]_R &= \tilde{\mathbf{G}}_{RD}(E) \mathbf{W}_{DL}(E) [\vec{\Psi}_n^i(k)] \\ &\stackrel{\text{(B.7)}}{=} \tilde{\mathbf{g}}_R(E) \mathbf{W}_{RD}(E) \tilde{\mathbf{G}}_D(E) \mathbf{W}_{DL}(E) [\vec{\Psi}_n^i(k)] \end{aligned} \quad (2.82)$$

$$\Rightarrow [\vec{\Psi}_n(k)]_R^\dagger = [\vec{\Psi}_n^i(k)]^\dagger \mathbf{W}_{LD}(E) \tilde{\mathbf{G}}_D^\dagger(E) \mathbf{W}_{DR}(E) \tilde{\mathbf{g}}_R^\dagger(E) \quad (2.83)$$

where the energy argument of the GFs E is the band energy of the right lead: $E \equiv E_n^R(k)$. Inserting these expressions into the expression for $j_{R,n}(k)$ defined above we get:

$$\begin{aligned} j_{R,n}(k) &= \frac{1}{i\hbar} \text{Tr} \left[[\vec{\Psi}_n^i(k)]^\dagger \mathbf{W}_{LD}(E) \tilde{\mathbf{G}}_D^\dagger(E) \times \right. \\ &\quad \left. \underbrace{\times \mathbf{W}_{DR}(E) \left\{ \tilde{\mathbf{g}}_R(E) - \tilde{\mathbf{g}}_R^\dagger(E) \right\} \mathbf{W}_{RD}(E) \tilde{\mathbf{G}}_D(E)}_{-i\tilde{\mathbf{\Gamma}}_R(E)} \mathbf{W}_{DL}(E) \vec{\Psi}_n^i(k) \right] \\ &= -\frac{1}{\hbar} \text{Tr} \left[\tilde{\mathbf{G}}_D^\dagger(E) \tilde{\mathbf{\Gamma}}_R(E) \tilde{\mathbf{G}}_D(E) \mathbf{W}_{DL}(E) \vec{\Psi}_n^i(k) [\vec{\Psi}_n^i(k)]^\dagger \mathbf{W}_{LD}(E) \right]. \end{aligned} \quad (2.84)$$

Thus summing over all states n resulting from electron injection from the left electrode and integrating over energy we get the contribution $I_R^{(L)}$ to the current $I_R = I_R^{(L)} + I_R^{(R)}$ resulting from electron injection from the left electrode.

$$\begin{aligned} I_R^{(L)} &= \int dE f(E - \mu_L) \sum_{n \in N_L, k} \delta(E - E_n(k)) j_{R,n}(k) \\ &= -\frac{1}{\hbar} \int dE f(E - \mu_L) \text{Tr} \left[\tilde{\mathbf{G}}_D^\dagger(E) \tilde{\mathbf{\Gamma}}_R(E) \tilde{\mathbf{G}}_D(E) \right. \\ &\quad \left. \mathbf{W}_{DL}(E) \sum_{n \in N_L, k} \delta(E - E_n^R(k)) \vec{\Psi}_n^i(k) [\vec{\Psi}_n^i(k)]^\dagger \mathbf{W}_{LD}(E) \right] \\ &= -\frac{1}{\hbar} \int dE f(E - \mu_L) \text{Tr} \left[\tilde{\mathbf{G}}_D^\dagger(E) \tilde{\mathbf{\Gamma}}_R(E) \tilde{\mathbf{G}}_D(E) \tilde{\mathbf{\Gamma}}_L(E) \right]. \end{aligned} \quad (2.85)$$

In a similar way we get for the current $I_L^{(R)}$ through the left lead resulting from electron injection from the right reservoir:

$$I_L^{(R)} = -\frac{1}{\hbar} \int dE f(E - \mu_R) \text{Tr} \left[\tilde{\mathbf{G}}_D^\dagger(E) \tilde{\mathbf{\Gamma}}_R(E) \tilde{\mathbf{G}}_D(E) \tilde{\mathbf{\Gamma}}_L(E) \right]. \quad (2.86)$$

2 Quantum theory of electron transport

In steady-state the contributions to the current due to electron injection from the left reservoir on the one hand and from the right reservoir on the other hand are individually conserved, i.e. $I_L^{(L)} = -I_R^{(L)} \equiv I^{(L)}$ and $I_L^{(R)} = -I_R^{(R)} \equiv I^{(R)}$. Thus in total the net current *through* the device is $I = I^{(L)} + I^{(R)} = -I_R^{(L)} + I_L^{(R)}$, and we finally obtain the famous Landauer formula for the current expressed with GFs.:

$$I = \frac{1}{h} \int dE (f_L(E) - f_R(E)) \text{Tr} \left[\tilde{\mathbf{G}}_D^\dagger(E) \tilde{\mathbf{\Gamma}}_R(E) \tilde{\mathbf{G}}_D(E) \tilde{\mathbf{\Gamma}}_L(E) \right]. \quad (2.87)$$

The trace in (2.87) corresponds to the total transmission function $T(E)$ which is the sum over all channel transmissions $T_n(E)$ defined earlier:

$$T(E) := \sum_n T_n(E) \equiv \text{Tr} \left[\tilde{\mathbf{G}}_D^\dagger(E) \tilde{\mathbf{\Gamma}}_R(E) \tilde{\mathbf{G}}_D(E) \tilde{\mathbf{\Gamma}}_L(E) \right]. \quad (2.88)$$

This is the so-called Caroli expression for the transmission function $T(E)$ named after C. Caroli who first derived it for the simple case of a one-dimensional tight-binding chain [71].

Obviously, the (non-hermitian) expression inside the trace of (2.88) must have to do with the (hermitian) transmission matrix $\mathbf{T}(E)$ defined earlier in eq. (2.11). Exploiting the invariance of the trace under cyclic permutations we find an equivalent expression for the transmission function now involving a hermitian expression that we can identify with the transmission matrix:

$$\mathbf{T}(E) \equiv \tilde{\mathbf{\Gamma}}_L^{1/2}(E) \tilde{\mathbf{G}}_D^\dagger(E) \tilde{\mathbf{\Gamma}}_R(E) \tilde{\mathbf{G}}_D(E) \tilde{\mathbf{\Gamma}}_L^{1/2}(E). \quad (2.89)$$

Now we can also identify the transmission amplitude $\mathbf{t}(E) = (t_{mn}(E))$ with:

$$\mathbf{t}(E) \equiv \tilde{\mathbf{\Gamma}}_R^{1/2}(E) \tilde{\mathbf{G}}_D(E) \tilde{\mathbf{\Gamma}}_L^{1/2}(E). \quad (2.90)$$

The generalized power of a hermitian matrix \mathbf{A} is defined as $\mathbf{A}^q = \mathbf{U} \text{diag}(a_i^q) \mathbf{U}^\dagger$ where the a_i are the eigenvalues of the matrix \mathbf{A} and \mathbf{U} is the unitary transformation that diagonalizes \mathbf{A} .

We note that the dimension of the transmission matrix (2.11) obtained in Sec. 2.1 is equal to either the number of modes of either the left or the right lead, which in turn is equal to the dimension of the unit cell of either lead. But the transmission matrix derived here has the dimension of the device subspace which is bigger than the dimensions of the unit cells of either lead. So the transmission matrix (2.89) derived from the NEGF is strictly speaking not equal to the original one (2.11) of the Landauer formalism. However, both formulations are of course equivalent. In fact, all non-zero matrix elements of the transmission matrix in the NEGF correspond to the original Landauer transmission matrix. All other matrix elements of the NEGF transmission matrix are zero.

2.3 Application to simple models

In order to illustrate some aspects of the NEGF formalism derived above, it is applied here to some simple model systems. We start with the well-known example of the simple tight-binding chain with one orbital per atom. While the standard tight-binding model

neglects the overlap between neighboring atomic orbitals, the overlap is included here as an additional parameter s in order to illustrate its effect on the electronic structure. Thus we have for the matrix elements of the Hamiltonian:

$$\langle m | \hat{H} | n \rangle = H_{mn} = \begin{cases} \epsilon_0 & \text{for } m = n, \\ t & \text{for } |m - n| = 1, \\ 0 & \text{otherwise} \end{cases} \quad (2.91)$$

and for the overlap matrix elements:

$$\langle m | n \rangle = S_{mn} = \begin{cases} 1 & \text{for } m = n, \\ s & \text{for } |m - n| = 1, \\ 0 & \text{otherwise} \end{cases} \quad (2.92)$$

Note, that the representation of the Hamiltonian in operator form in the NOBS is *not* straight forward, since it involves the inversion of the overlap matrix $\mathbf{S} = (S_{mn})$ as pointed out in App. A, eq. (A.2):

$$\hat{H} = \sum_{mn} |m\rangle (\mathbf{S}^{-1} \mathbf{H} \mathbf{S}^{-1})_{mn} \langle n|. \quad (2.93)$$

Thus one introduces hopping terms beyond the first neighbor into the Hamiltonian operator although the corresponding matrix elements are zero. Orthogonalizing the basis set for example by the Löwdin scheme one would also obtain hopping terms beyond the nearest neighbor hopping. But we will not pursue this any further. Instead we will apply the above developed NEGF formalism for a NOBS to the model and study the effect of the overlap on the DOS.

The PDOS for a NOBS is given by eq. (2.58). The PDOS of the tight-binding chain is plotted in Fig. 2.4 for various parameters of the nearest neighbor overlap s , while the on-site energy and the hopping are kept fixed: $\epsilon_0 := 0$ and $t := -1$. We observe, that increasing the overlap leads to a displacement towards higher energies and a simultaneous broadening of the energy band until at $s = 1/2$ the band width becomes infinite. This is due to a singularity of the energy dispersion at the Brillouin zone boundary $ka = \pm\pi$:

$$E(k) = \frac{\epsilon_0 + 2t \cos(ka)}{1 + 2s \cos(ka)} \longrightarrow \infty \text{ for } ka \rightarrow \pm\pi \text{ and } s = \frac{1}{2}. \quad (2.94)$$

Increasing the overlap s beyond this value, the DOS becomes even negative for some values of the energy. This pathological behavior can be traced back to the appearance of singularities inside the first Brillouin zone, and relates to the fact that the tight-binding model is actually pathological for overlaps $s > 1/2$. In fact, it is physically impossible to have a nearest neighbor overlap of $s > 1/2$ but no overlap between second nearest neighbors. The pathological behavior can be repaired quite easily by including overlap beyond the nearest neighbor approximation. This can be seen directly from the energy dispersion of the generalized tight-binding model including hopping and overlaps beyond the first nearest neighbor:

$$E(k) = \frac{\epsilon_0 + \sum_n 2t_n \cos(kna)}{1 + \sum_n 2s_n \cos(kna)}, \quad (2.95)$$

where s_n and t_n denote overlap and hopping, respectively, between n -th nearest neighbors. Thus in order to avoid unphysical results it is important to include overlap between atomic

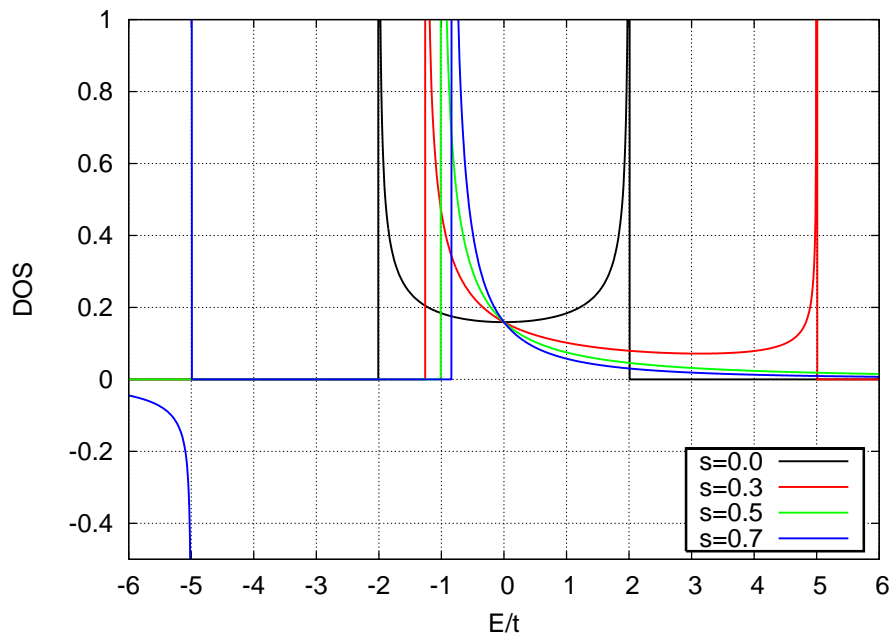


Figure 2.4: PDOS of tight-binding chain with overlap for different values of the overlap parameter s but for fixed on-site energy parameter ϵ_0 and hopping parameter t .

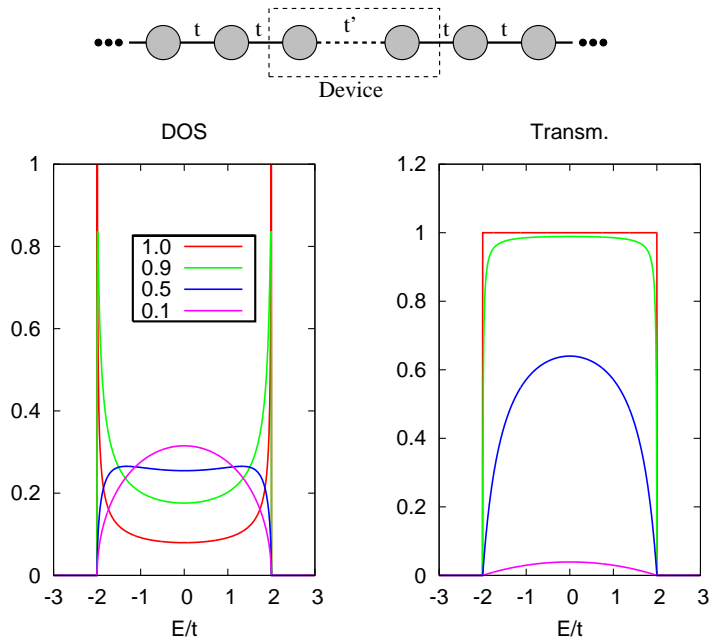


Figure 2.5: Tunneling between two semi-infinite chains. The graphs show the PDOS projected onto a tip atom (left) and the transmission (right) for different values of the hopping t' between the chains in units of the hopping parameter t of the tight-binding chains. Overlap between atomic orbitals is completely neglected.

orbitals up to a sufficiently high degree of neighborhood. This will become very important in the context of combining *ab initio* electronic structure calculations with the NEGF formalism as the the basis sets employed in common quantum chemistry packages like GAUSSIAN [47] are typically highly non-orthogonal.

Next, we will have a look at the electronic structure and the transport properties of two tunnel-coupled semi-infinite tight-binding chains. In Fig. 2.5 the PDOS projected onto one of the tip atoms (bottom left) and the transmission function (bottom right) is shown for the model depicted at the top of the figure for various values of the tunnel coupling t' between the two chains. We observe, how the PDOS is slowly transformed from the DOS of the 1D chain with the characteristic van Hove singularities at the band edges to the semicircular “surface” DOS of the semi-infinite chain when the tunneling coupling t' is decreased. Simultaneously, the perfect transmission of the 1D chain within the energy band is reduced considerably when decreasing the tunnel coupling as is expected. For $t' = 0.1t$ we enter the tunneling regime where the transmission is described by the Bardeen formula for tunneling $T \approx t'/tD(\epsilon_F)$ [72].

Finally, we have a look at a simplified model of a typical situation in mesoscopic physics and molecular electronics: An island (which could be a quantum dot in a mesoscopic system or a molecule in molecular electronics) coupled to two semi-infinite leads. The island in the simple model is a single site coupled to two semi-infinite tight-binding chains

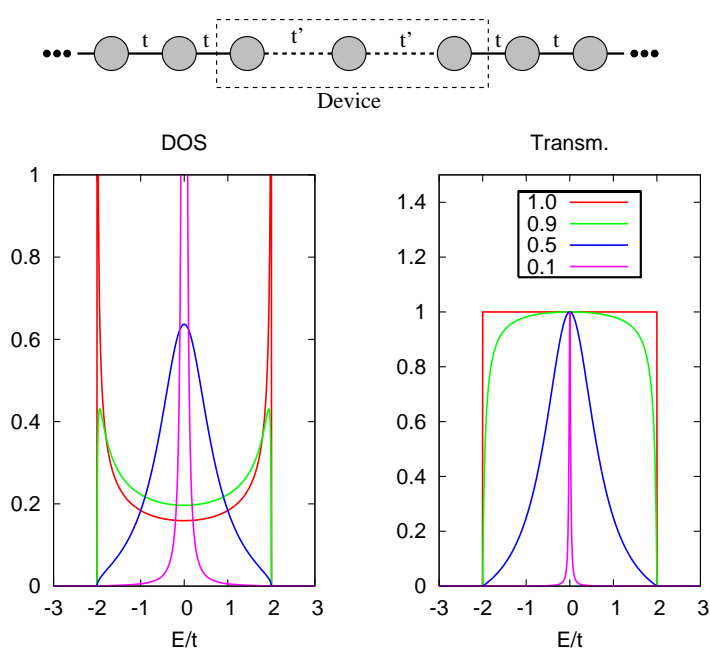


Figure 2.6: Tunneling through a dot connected to two semi-infinite leads. The graphs show the PDOS projected onto the central dot (left) and the transmission (right) for different values of the coupling t' of the dot to the two leads in units of the hopping parameter t of the tight-binding chains.

(see the illustration at the top of Fig. 2.6). We start again with strong coupling to the leads, $t' \equiv t$, and decrease t' . We observe that the PDOS projected onto the island is transformed from the DOS of the perfect 1D chain for ($t' = t$) to a Lorentz peak for weak coupling and also the transmission is now given by a Lorentz peak in that limit. We further note that the transmission remains perfect exactly at the on-site energy of the island although the coupling has decreased by one order of magnitude. This phenomenon is called resonant transmission through a molecular (or atomic) level.

2.4 Discussion of the Landauer approach

The Landauer formalism introduced above, assumes that electron transport in nanoscopic conductors is phase coherent. Inelastic scattering of electrons e.g. in electron-electron or electron-phonon scattering processes is neglected. This turns out to be a rather good approximation for low temperature and small bias voltages. The reason for this is that for small bias voltages the transport properties are principally determined by the conduction electrons at the Fermi level. At low temperatures the conduction electrons at the Fermi level cannot lose energy because the Fermi sea is completely occupied. On the other hand they cannot gain energy because there are no phonons available at low temperatures. Therefore electron transport is elastic, and thus phase coherent at low temperature and for small bias.

A strict generalization of the Landauer formula to interacting electron systems (i.e. including electron-electron interaction and/or electron-phonon interaction) is given by the Meir-Wingreen formula [73] which assumes an interacting device coupled to non-interacting leads. The Meir-Wingreen formula actually reduces to the Landauer formula in the limit of zero temperature and zero bias, thus demonstrating the above considerations strictly. Thus in principle the Landauer formula can be considered a strict result (for low temperature and small bias) under the condition that the GF of the device is the true interacting GF (see e.g. the book by Mahan [74] for an introduction to many-body GFs). However, the GF employed here is the one-body GF describing non-interacting electrons. Thus the electron-electron interaction can only be taken into account on a mean-field level. The task is now to find a one-body GF that approximates the true interacting many-body GF sufficiently well. In Ch. 3 we show how to combine the NEGF formalism with *ab-initio* electronic structure calculations on the level of DFT, i.e. the one-body GF is calculated from the Kohn-Sham Hamiltonian. Although DFT has been quite successful in describing many materials it is not clear *a priori*, whether it can give a reasonable description of the transport properties of nanoscopic conductors. This issue is discussed in Ch. 3.

The effect of inelastic scattering by electron-phonon interaction on the electrical transport through Au nanocontacts [68] and atomic Au wires [75] has been studied recently with microscopic models on the basis of the Meir-Wingreen formula with different approximations for the electron-phonon coupling. Viljas *et al.* treated the electron-phonon interaction in lowest order perturbation theory in combination with a tight-binding model of the electronic structure, while Frederikson *et al.* treated the interaction within the self-consistent Born approximation (SCBA) [74] in combination with an *ab initio* description of the electronic structure on the DFT level.

In principle, it is also possible to introduce decoherence by inelastic scattering into the Landauer formalism phenomenologically by introducing “conceptual voltage probes”

2 *Quantum theory of electron transport*

which act as phase-breaking scatterers as was first realized by Büttiker[63]. However, this can only be done in a meaningful way for very simple models systems [76]. To obtain meaningful results for realistic models of nanoscopic conductors it is necessary to develop a microscopic theory for the effect of inelastic scattering on the transport like the ones mentioned above.

3 *Ab initio* quantum transport

Density functional theory (DFT) has become a standard method for electronic structure calculations in condensed matter physics and quantum chemistry [77]. This chapter explains how the transport theory described in Ch. 2 can be combined with DFT to describe transport through nanostructures from first principles. Therefore, I will first briefly introduce the basic principles of DFT in Sec. 3.1. An extensive review of DFT can be found e.g. in Ref. [78]. Finally, in Sec. 3.2, I will describe how the DFT based quantum transport approach is implemented in the ALACANT package.

3.1 Density functional theory

The electrons in a solid or a molecule are described by a many-body wavefunction $\Psi(\{\vec{r}_i\})$ of the electron coordinates $\{\vec{r}_i\}$, which is a solution of the many-body Schrödinger equation:

$$\hat{\mathcal{H}}|\Psi\rangle = E|\Psi\rangle. \quad (3.1)$$

$\hat{\mathcal{H}}$ is the Hamiltonian of the interacting electron system, containing the kinetic energy $\hat{\mathcal{T}}$, the Coulomb attraction of the atomic nuclei (ion cores) $\hat{\mathcal{V}}_{e-i}$ and the electron-electron interaction $\hat{\mathcal{V}}_{e-e}$:

$$\hat{\mathcal{H}} = \hat{\mathcal{T}} + \hat{\mathcal{V}}_{e-i} + \hat{\mathcal{V}}_{e-e}. \quad (3.2)$$

The many-body Schrödinger equation can in principle be solved by expanding the wavefunction in a basis of Slater determinants, thus converting it to a problem of diagonalizing matrices. However, in practice this can only be done for systems with very few electrons as the dimension of the Slater basis grows with the number N of electrons as $N!$. Instead, before the advent of DFT the standard approach in solid state physics and in quantum chemistry has been to approximate the many-body wave function by a single Slater determinant that minimizes the total energy. This is the Hartree-Fock approximation (HFA) which is the basis for more refined approaches in quantum chemistry, like perturbation theory, or configuration interaction [70]. However, the HFA gives a rather crude description of the electronic structure of solids and molecules. The main reason is that the single-determinant approach neglects electron correlations, but instead describes the electrons as independent of each other interacting via an effective mean field. In particular, the description of metallic solids within the HFA is very bad, describing them often as insulators or semiconductors. The above mentioned systematic improvement of HFA by perturbation theory or configuration interaction on the other hand becomes computationally too expensive for larger number of electrons just as the exact diagonalization approach described above, limiting these methods to systems with a relatively small number of electrons.

An alternative approach is density functional theory (DFT) where the basic variable is

the electron density instead of the full many-body electron wave function $\Psi(\{\vec{r}_i\})$:

$$n(\vec{r}) = \langle \vec{r} | \hat{P} | \vec{r} \rangle = N \int |\Psi(\vec{r}, \vec{r}_2, \dots, \vec{r}_N)|^2 d\vec{r}_2 \dots d\vec{r}_N, \quad (3.3)$$

which is a much simpler quantity to handle than the full many-body wavefunction.

3.1.1 Hohenberg-Kohn theorem

The basis for DFT is the Hohenberg-Kohn (HK) theorem [49] which reduces the fully interacting N -electron problem to determining the ground state electron density $n(\vec{r})$:

1. The non-degenerate ground state energy of an N electron system, E_N , is a unique, universal functional of the electron density $n(\vec{r})$.
2. The electron density that minimizes the energy functional is the exact ground state electron density

So if we know the energy functional of the electron density $E[n]$ then we can determine the electron density of the ground state by simply minimizing the energy functional, which would be much simpler than resolving the many-body Schrödinger equation. It is important to note, that no approximations has been made so far. Thus unlike the HFA, DFT is in principle an exact theory which allows us to calculate the exact ground state density of an interacting electron system. However, the drawback is that the exact energy functional is not known. So one has to come up with approximations for the energy functional. Different approximations to the energy functional are discussed after the next subsection.

3.1.2 Kohn-Sham equations

The HK theorem actually does not give a practical recipe for calculating the energy functional of the electron density, but only states the existence of that functional. A practical way for calculating the energy functional is given by the Kohn-Sham (KS) equations [79] which map the interacting electron system with some electron density $n(\vec{r})$ onto an auxiliary non-interacting system with the same electron density as the interacting system. The KS equations are thus the starting point for any practical implementation of DFT.

We start by decomposing the energy functional into different contributions:

$$E[n] = T[n] + E_H[n] + E_{xc}[n] + E_{ext}[n]. \quad (3.4)$$

$T[n]$ is the kinetic energy for that electron density

$$T[n] = \langle \Psi | \hat{T} | \Psi \rangle, \quad (3.5)$$

where $|\Psi\rangle$ is the many-electron wavefunction corresponding to the electron density n for that system. Note, that there is no explicit formula for computing the kinetic energy from the electron density n . This is one of the reasons why there is no explicit formula for the energy functional. $E_H[n]$ is the Hartree term describing the classical Coulomb repulsion

of the electron cloud. For this term an explicit formula can be written for its functional dependence on the electron density:

$$E_H[n] = \frac{1}{2} \int \frac{n(\vec{r})n(\vec{r}')}{|\vec{r} - \vec{r}'|} d\vec{r}d\vec{r}' \quad (3.6)$$

$E_{xc}[n]$ is the so-called exchange-correlation (XC) term and no explicit exact formula exists for this term either. It is thus the other term besides the kinetic energy term responsible for the impossibility of finding an explicit expression for the total energy functional. The XC term contains pure quantum effects like the exchange interaction due to the Pauli principle and electron correlation effects. This term is usually expressed in terms of an integral over the electron density and an unknown XC energy density $\epsilon_{xc}[n](\vec{r})$:

$$E_{xc}[n] = \int d\vec{r} n(\vec{r})\epsilon_{xc}[n](\vec{r}). \quad (3.7)$$

Finally, the last term $E_{ext}[n]$ is the interaction of the electron cloud with the external potential due to the atomic nuclei. This term can again be written as an explicit functional of the electron density:

$$E_{ext}[n] = \int d\vec{r} n(\vec{r})V_{e-i}(\vec{r}) \quad (3.8)$$

The basic idea of the KS method is to introduce an auxiliary set of one-electron wavefunctions $\{\phi_i(\vec{r})\}$ that give rise to the same electron density $n(\vec{r})$ as the full many-body wavefunction $\Psi(\vec{r}_1, \dots, \vec{r}_N)$:

$$n(\vec{r}) = \sum_{i=1}^N \phi_i^*(\vec{r})\phi_i(\vec{r}) \quad \text{with} \quad \langle \phi_i | \phi_j \rangle = \delta_{ij} \quad (3.9)$$

We can then define a KS energy functional $T_{KS}[n]$ that can easily be calculated from the auxiliary KS wavefunctions ϕ_i :

$$T_{KS}[n] = \sum_{i=1}^N \langle \phi_i | \hat{T} | \phi_i \rangle. \quad (3.10)$$

However, the KS kinetic energy term is not identical with the kinetic energy term of the interacting electron system $T[n]$. The difference between the KS kinetic energy and the true kinetic energy is again unknown, and is absorbed into the also unknown XC functional which is redefined in the KS method as:

$$E_{XC}[n] \rightarrow E'_{XC}[n] = E_{XC}[n] + T[n] - T_{KS}[n]. \quad (3.11)$$

Thus all many-body effects have now been shifted to the XC functional, which is the only contribution to the total energy functional that needs to be approximated. All other terms can be calculated exactly within the KS method. The main advantage of the KS method is that we get a set of effective one-body Schrödinger equations –the KS equations– for the auxiliary KS wavefunctions ϕ_i which in turn give the ground state electron density of the true interacting electron system. From the variational principle

3 *Ab initio* quantum transport

it follows that in the ground state the total energy must be stationary with respect to variations of the KS wavefunctions:

$$\frac{\delta E[n]}{\delta \phi_i} - \epsilon_i \phi_i = 0 \quad (3.12)$$

where the ϵ_i are Lagrange multipliers which ensures the orthogonality of the KS wavefunctions ϕ_i and will give the effective KS eigenenergies. The KS equations follow directly:

$$\left(-\frac{\hbar^2}{2m} \nabla^2 + V_H[n](\vec{r}) + V_{ext}(\vec{r}) + V_{XC}[n](\vec{r}) \right) \phi_i(\vec{r}) = \epsilon_i \phi_i(\vec{r}) \quad (3.13)$$

where

$$V_H[n](\vec{r}) := \int d\vec{r}' \frac{n(\vec{r}')}{|\vec{r} - \vec{r}'|} \quad (3.14)$$

is the Hartree potential due to the direct electron-electron interaction and

$$V_{XC}[n](\vec{r}) := \frac{\delta E_{XC}[n]}{\delta n}(\vec{r}). \quad (3.15)$$

is the effective exchange-correlation potential.

The interacting problem has now been reduced to a set of non-interacting Schrödinger equations. One should emphasize that up until now no approximations have been made. The KS equations are exact if one knows the exact XC functional. The KS Hamiltonian

$$\hat{H}_{KS} = -\frac{\hbar^2}{2m} \nabla^2 + \hat{V}_{ext} + \hat{V}_H[n] + \hat{V}_{XC}[n] \quad (3.16)$$

depends on the electron density $n(\vec{r})$ which is the quantity to be determined by the KS wavefunctions. Thus the KS equations are a non-linear eigenvalue problem which has to be solved self-consistently. The central task of the KS formulation of DFT is to find suitable approximations for the unknown XC functional.

3.1.3 Energy functionals

Local density approximation (LDA). The simplest approximation is to start from the homogeneous electron gas, and assume that the electron density is only slightly modulated by the potential of the ion cores. In this case the XC energy density $\epsilon_{XC}[n](\vec{r})$ at point \vec{r} can be assumed to be that of a homogenous electron gas with the same density as the local density of the non-homogeneous electron gas, i.e. $\epsilon_{XC}^{LDA}[n](\vec{r}) := \epsilon_{XC}^{HEG}(n(\vec{r}))$.

$$E_{XC}^{LDA}[n] = \frac{1}{2} \int n(\vec{r}) \epsilon_{XC}^{HEG}(n(\vec{r})) d\vec{r}. \quad (3.17)$$

Thus in LDA the XC energy density ϵ_{XC}^{LDA} is simply a function of the local electron density $n(\vec{r})$ and not a functional. In spite of its apparent simplicity LDA has been quite successful in describing metallic systems. One of its major shortcomings is that it cannot give a reasonable description of strongly localized electrons like e.g. the *d*- and *f*-states of transition metals. In this case the electron density is strongly modulated and the approximation of a slowly varying density is obviously a bad one.

Generalized Gradient Approximation (GGA). A logical step for improving LDA is to make the XC energy density also a function of the gradient of the electron density in addition to the local electron density:

$$E_{XC}^{GGA}[n] = \frac{1}{2} \int n(\vec{r}) \epsilon_{XC}(n(\vec{r}), \vec{\nabla} n(\vec{r})) d\vec{r} \quad (3.18)$$

While LDA works well for simple metals, GGA improves the description of transition metals considerably. However, in general even GGA does not give a good description of semiconductors and insulators. And in particular, it fails to give a good description of the so-called strongly correlated materials like the transition metal oxides. This is due to the insufficient cancellation of the self-interaction error by the approximate XC functionals of both LDA and GGA (although the self-interaction error is smaller for GGA). This self-interaction error raises artificially the energy of occupied localized states like the d - and f -states which are of outmost importance in the transition metal oxides [80].

Hybrid functionals. As said before the main problem of the LDA and GGA functionals is the spurious self-interaction error for localized electron states like e.g. the d - and f -states of transition metals, and the orbitals of molecules. On the other hand in the HFA the exchange interaction term cancels exactly the self-interaction present in the Hartree-term. Thus a possible way of correcting the spurious self-interaction in the GGA functional is to reintroduce Hartree-Fock exchange (HFX) into the KS theory by mixing some HFX with the GGA exchange functional, an idea that was first put forward by Becke[81]. Although a deeper theoretical justification was given for this ad hoc correction, the exact amount of HFX that needs to be reintroduced in order to give a sufficient correction of the self-interaction error in the GGA functional is unfortunately unknown and thus needs to be fitted to experiments[81]. Thus strictly speaking DFT using hybrid functionals does not really represent an ab-initio method. However, it turns out that the parameterization of the B3LYP hybrid functional which was determined by fitting to experimental results of a certain class of molecules also works surprisingly well for many molecules which had not been included into the fitting data set. Moreover, it also gives a reasonable description of the electronic structure and of the magnitude of the band gap of insulating solids (where GGA normally fails) and even of some strongly correlated materials like e.g. NiO [82].

LDA+U method. The idea behind the LDA+U method [83] is similar to the hybrid functional method: For the strongly localized atomic orbitals of a material e.g. the d -orbitals of the transition metals and the f -orbitals of the rare earth metals, a Hubbard U parameter presenting the screened electron-electron interaction in these orbitals is added to the LDA KS Hamiltonian and treated in the HFA thus correcting the self-interaction error of these orbitals. In principle it is possible to extract the U parameter from a previous LDA calculation. However, in practice this is seldom done since it does not reproduce the experiments sufficiently well. Instead the U parameter is normally fitted in order to reproduce certain material properties just as the amount of HFX in the hybrid functionals has been fitted to reproduce certain properties of molecules. As the hybrid functionals, LDA+U gives a reasonable description of the electronic and magnetic structure of strongly correlated materials like NiO, and improves considerably the magnitude of the band gap of these materials in comparison with LDA [84].

Exact Exchange functionals. Another approach to correct the self-interaction error of standard DFT methods is to derive a local KS exchange potential from the non-local

exact exchange energy of the HFA. The Exact Exchange (EXX) scheme is self-interaction free since the exact exchange energy of the HFA cancels exactly the self-interaction of the Hartree-term. On the other hand, the EXX potential is local as required from the KS theory in contrast to the HFX term added by hand in the Hybrid functional approach which is inherently non-local. Therefore the EXX together with a good approximation of the correlation energy (as is the case in LDA and GGA) comes very close to an exact implementation of DFT within the KS scheme, and thus gives an excellent description of the electron density. Moreover, no empirical parameters are needed so that EXX is a real *ab initio* method. Unfortunately, the computational cost for the calculation of the EXX functional is very high compared to other methods [85, 86, 87].

3.2 Kohn-Sham based NEGF formalism

We now extend the Landauer formalism presented in Ch. 2 to the case of interacting electrons. The system is described in an effective single-particle picture by treating the electron-electron interaction by a mean-field method like the KS scheme or the HFA. The problem treated here, is to apply a mean-field method (established only for finite or periodic systems) to the open (i.e. infinite and non-periodic) system of the transport problem consisting of the leads and the device. The arguments are presented for the KS formalism, but are easily applied to the HFA.

Far away from the scattering region the electronic structure of the leads has relaxed to that of the bulk (perfect) lead. So if the device region is sufficiently big (i.e. a sufficiently big part of the electrodes is included into the device region) the lead electrons can be described as non-interacting quasi-particles moving in the effective potential landscape (generated by the ion-core potentials and the effective mean-field potential of the other electrons of the bulk leads. Thus we describe the leads by the fixed effective one-body Hamiltonians of the bulk leads, and the electron-electron interaction is taken into account explicitly only the device region. The (many-body) device Hamiltonian $\hat{\mathcal{H}}_D$ comprises a single-body term describing the kinetic energy \hat{T}_D and the external potential \hat{V}_{e-i} inside the device, and the electron-electron interaction \hat{V}_{e-e} between the electrons. Applying the KS scheme the resulting KS Hamiltonian for the *entire* system is given by

$$\mathbf{H}_{KS}[n] = \begin{pmatrix} \mathbf{H}_L & \mathbf{H}_{LD} & \mathbf{0} \\ \mathbf{H}_{DL} & \mathbf{H}_D[n] & \mathbf{H}_{DR} \\ \mathbf{0} & \mathbf{H}_{RD} & \mathbf{H}_R \end{pmatrix}, \quad (3.19)$$

and depend on the electron density n of the entire system. In order to keep things simple we will not treat overlap between basis functions explicitly. The arguments presented here are easily generalized to non-orthogonal basis sets by using the formulas presented in Ch. 2.

We define a Green's function (GF) matrix corresponding to the KS Hamiltonian which thus also becomes a functional of the electron density $n(\vec{r})$

$$\mathbf{G}_{KS}[n](E) = (E - \mathbf{H}_{KS}[n] + i\eta^{0+})^{-1}. \quad (3.20)$$

On the other hand, we can obtain the electron density by integrating the GF up to the Fermi energy:

$$n(\vec{r}) = -\frac{1}{\pi} \text{Im} \int_{-\infty}^{\epsilon_F} dE \langle \vec{r} | \hat{G}_{KS}[n](E) | \vec{r} \rangle. \quad (3.21)$$

Thus, by self-consistently calculating the density matrix from the Green's function, we solve the mean-field problem and thus minimize the energy of the entire system.

Up until now we have only restated the KS formalism in terms of GFs instead of wavefunctions. Now we have to apply it to the situation of the open system described by the Hamiltonian (3.19). The difficulty lies in determining the Fermi energy ϵ_F for the open system. However, as we will see now, this is only a conceptual problem, that can be solved in a relatively easy manner.

The Fermi energy is that of the entire system in equilibrium and in general will be different from the Fermi energy of any of the two (isolated) bulk leads due to the electric field caused by charges present in the device region. However, this electric field will only cause a shift in the electrostatic potential of the leads if the device region is chosen sufficiently big, since only the direct Coulomb interaction (i.e. classical electrostatic interaction) between charges is long range while the pure quantum mechanical part of the Coulomb interaction (i.e. exchange and correlation contributions) is relatively short range. On the other hand the Fermi level must be the same throughout the entire system. Thus we can shift the Hamiltonian of the two leads to a common arbitrary Fermi level which we choose to be zero for convenience. The electrostatic shift of the two leads is equivalent to a shift Δ_D of the Hamiltonian of the device region:

$$\mathbf{G}_D[n](E) = (E - \mathbf{H}_D[n] - \Delta_D - \Sigma_L(E) - \Sigma_R(E))^{-1}. \quad (3.22)$$

The negative of that shift corresponds to the real Fermi energy of the entire system: $\epsilon_F = -\Delta_D$. Next, in order to find the real Fermi level of the system we impose charge neutrality on the device region since we have assumed that the device contains a sufficient part of the electrodes so that it has relaxed to its bulk electronic structure. The number of electrons in the device region corresponding to a certain energy shift is found by integrating the Greens function of the device part up to the adjusted Fermi energy of the leads, i.e. zero:

$$N_D(\Delta_D) = -\frac{1}{\pi} \text{Im} \int_{-\infty}^0 dE \text{Tr}[\mathbf{G}_D[n](E)]. \quad (3.23)$$

Thus by imposing charge neutrality on the device region we obtain the energy shift Δ_D of the device Hamiltonian and thus the Fermi energy of the entire system.

The KS Hamiltonian of the device \mathbf{H}_D is given by the single-body term $\mathbf{H}_D^0 = \mathbf{T}_{KS} + \mathbf{V}_{\text{ext}}$ and the effective single-particle potential of the electron-electron interaction comprising the Hartree- and the XC term $\mathbf{V}_C[n] = \mathbf{V}_H[n] + \mathbf{V}[n]$ which are both functionals of the electron density $n(\vec{r})$. But since we have assumed that the electrons do not interact with each other outside the device region the Hamiltonian and consequently the GF only depend on the electron density $n_D(\vec{r})$ inside the device region. In turn ρ_D can be calculated by integrating the device part of the GF:

$$n_D(\vec{r}) = -\frac{1}{\pi} \text{Im} \int_{-\infty}^0 dE \langle \vec{r} | \mathbf{G}_D[n](E) | \vec{r} \rangle. \quad (3.24)$$

The self-consistent calculation of the electron density from the GF to minimize the energy of the whole system can thus be restricted to the device's subspace.

The energy of the system can be calculated by summing up the KS energies ϵ_i corrected for the double-counting:

$$E[n] = \sum_i \epsilon_i - J[n_D] + E_{xc}[n_D] - \int d\vec{r} V_{xc}[n_D](\vec{r}) n_D(\vec{r}). \quad (3.25)$$

3 *Ab initio* quantum transport

where we have made use of the fact that the electrons are assumed to be interacting only inside the device region so that only there we need to account for the double-counting error made in summing up the KS energies. In order to separate the energy contributions of the leads from the energy contribution of the device in the sum we rewrite the sum over the KS energies in terms of the KS Hamiltonian and the corresponding density matrix \hat{P} defined by the KS eigenstates:

$$E'[\mathbf{P}_{KS}] := \sum_i \epsilon_i = \text{Tr}[\mathbf{P}_{KS} \mathbf{H}_{KS}]. \quad (3.26)$$

By dividing the KS Hamiltonian and the density matrix into sub-matrices as before we can separate the different contributions to the energy, and write the total energy as

$$E'[\mathbf{P}_{KS}] = E_L + E_{LD} + E_D + E_{RD} + E_R, \quad (3.27)$$

where we have defined the energy of the device,

$$E_D = \text{Tr}[\mathbf{P}_D \mathbf{H}_D] \quad (3.28)$$

the energies of the left lead and right lead,

$$E_L = \text{Tr}[\mathbf{P}_L \mathbf{H}_L] \quad \text{and} \quad E_R[\mathbf{P}_R] = \text{Tr}[\mathbf{P}_R \mathbf{H}_R] \quad (3.29)$$

and the coupling energies between left lead and device,

$$E_{LD} = \text{Tr}[\mathbf{P}_{LD} \mathbf{H}_{DL}] + \text{Tr}[\mathbf{P}_{DL} \mathbf{H}_{LD}] = 2\text{Re}(\text{Tr}[\mathbf{P}_{LD} \mathbf{H}_{DL}]), \quad (3.30)$$

and right lead and device

$$E_{RD} = \text{Tr}[\mathbf{P}_{RD} \mathbf{H}_{DR}] + \text{Tr}[\mathbf{P}_{DR} \mathbf{H}_{RD}] = 2\text{Re}(\text{Tr}[\mathbf{P}_{RD} \mathbf{H}_{DR}]). \quad (3.31)$$

Since we have assumed that the device region is sufficiently big so that the electronic structure in the leads has relaxed to that of the bulk, \mathbf{P}_L and \mathbf{P}_R remain constant during the self-consistent procedure, and thus also the energy contributions of the leads, E_L and E_R . On the other hand the coupling energies actually do change because the GFs \mathbf{G}_{LD} and \mathbf{G}_{RD} directly depend on \mathbf{G}_D (see eqs. (B.6) and (B.7)). So the two energy terms E_{LD} and E_{RD} always have to be included into the energy calculation.

The arguments presented in this section are easily adapted to the HFA. Instead of the KS Hamiltonian \mathbf{H}_{KS} the Fock matrix \mathbf{F} is used to calculate the GF of the device which depends on the density matrix \mathbf{P} which in turn can be calculated from the Hartree-Fock GF of the device thus defining again an iterative procedure for the self-consistent solution of the HF equation. In the HFA the expression for calculating the total energy from summing up the HF eigenenergies corrected for the double-counting is much simpler than the corresponding expression in the KS scheme.

$$E_{\text{tot}} = \sum_i \epsilon_i - \frac{1}{2} \text{Tr}[\mathbf{P}_D \mathbf{V}_{HF}] = \text{Tr}[\mathbf{P}\mathbf{F}] - \frac{1}{2} \text{Tr}[\mathbf{P}_D \mathbf{V}_{HF}], \quad (3.32)$$

where \mathbf{V}_{HF} is the effective Coulomb interaction in the HFA.

Finally, Fig. 3.1 shows a schematic picture of the implementation of the self-consistent transport method presented in this section. This approach is implemented in the ALACANT package which interfaces the quantum chemistry program GAUSSIAN[47] to implement the NEGF formalism.

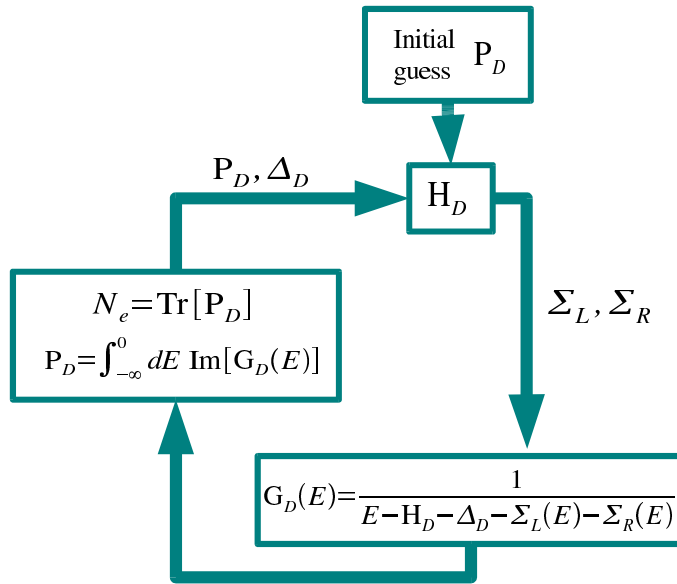


Figure 3.1: Diagram illustrating the ALACANT self-consistent procedure for KS based NEGF formalism as explained in the text.

3.2.1 Modeling of the bulk electrodes

As explained in Ch. 2, part of the electrodes has to be included in the device region, and in the case of nanocontacts the nanoscopic device actually consists only of the atomically sharp tips of the two metal electrodes. In the KS based NEGF described before and implemented in the ALACANT package the electronic structure of the device region and thus the part of the electrodes included in the device is calculated self-consistently within the KS scheme while the electronic structure of the rest of the bulk electrodes is assumed to be fixed. Their effect on the electronic structure of the device region is taken into account via self-energies in the KS GF of the device region, eq. (3.22).

Since the exact atomic structure of the macroscopic electrodes in a real experiment is unknown the question arises how to model the part of the left and right semi-infinite electrodes that has not been included in the device region, and how to calculate the corresponding self-energies. The ignorance of the exact atomic structure of the electrodes in an experiment is a not negligible source of uncertainty in the transport calculations. Therefore an appropriate model for the bulk electrodes should have the property that the calculated conductance does not depend too much on the actual atomic structure of the electrode. A first problem that one encounters is that the self-energy of the bulk electrodes can only be calculate for idealized situations.

A possible choice is to model the electrodes as perfect semi-infinite crystalline leads of some finite thickness, i.e. nanowires [88, 53, 89]. In this case the self-energies can be calculated as shown in Ch. 2 and App. C. However, it has been shown that the results of a transport calculation using nanowires as electrode models depend strongly on the actual thickness of the nanowire and the actual atomic structure [90, 91]. Moreover, the electrodes in real experiments are very far from being perfect nanowires but are actually substantial polycrystalline electrodes. Nevertheless, using perfect nanowires as the electrodes is interesting for performing model calculations, e.g. to study the effect of a single impurity or vacancy on the transport properties of an otherwise perfect nanotube or the effect of a constriction in a perfect graphene nanoribbon [92].

In order to avoid the that the resulting conductance reflects the finite thickness of the nanowire one can go to the crystalline limit by making the wire infinitely thick. In practice this can be done by making the system periodic in the directions perpendicular to the transport direction so that the self-energy matrices become dependent on the wave vector perpendicular to the transport direction [91, 54]. However, this approach is computationally expensive and the resulting conductance still reflects the crystal direction of the electrodes. Alternatively, jellium models have been used in methods based on a description in terms of scattering states[93, 94]. In this case the electrodes are completely featureless and thus do not reflect any of the chemical properties of the material. Thus this choice is also not free from controversy [95].

For these reasons the choice in the original implementation of the ALACANT package (then called GEEM for Gaussian Embedded Cluster Method) [52] was to describe the bulk electrodes with a Bethe lattice parameterized tight-binding model with the coordination and parameters appropriate for the chosen electrode material. The advantage of choosing a Bethe lattice (BL) resides in that, although it does not have long-range order, the short-range order is captured and it reproduces fairly well the bulk density of states of most commonly used metallic electrodes. The right hand side of Fig. 3.2 depicts schematically a BL of coordination 6. The left hand side of that same figure illustrates schematically how the device (depicted here as a nanocontact) is connected to the BL electrodes: For

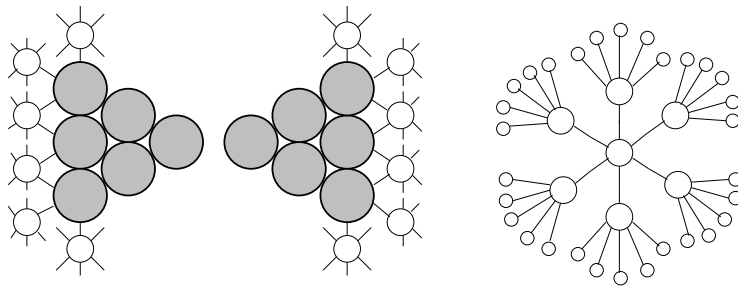


Figure 3.2: Left: Schematic 2D illustration of a nanocontact (big grey circles) with the first atoms of the BL (small white circles) attached to the outer planes of the nanocontact. Right: Finite section of Bethe lattice (BL) with coordination 6. All atoms of the BL have the same coordination as in the corresponding crystalline structure giving rise to short range order. But there is no long range order in the BL due to the absence of closed loops.

each atom in the outer planes of the device, a branch of the BL is added in the direction of any missing bulk atom (including those missing in the same plane). The directions in which tree branches are added are indicated by white small circles which represent the first atoms of the branch in that direction. Assuming that the most important structural details of the electrode are included in the central cluster, the BLs should have no other relevance than that of introducing the most generic bulk electrode for a given metal. In App. D it is explained how to calculate BL self-energies.

Fig. 3.3 shows the result of an actual transport calculation for the Al nanocontact as shown on the left hand side of that same figure. The left hand side of Fig. 3.3 also shows how the surface atoms of the BL electrodes are connected to the outermost atomic planes of the nanocontact. The electronic structure of the device region has been calculated on the LDA level of DFT and the CRENBS minimal basis set and effective core pseudo potential (ECP) by Christiansen and coworkers [96] has been employed.

Apart from giving a reasonable generic description of the bulk electrodes the computation of the self-energies for the BL model is also computationally very efficient compared to computing the self-energies for perfect crystalline systems due to the absence of loops. In this respect the BL model for the description of electrodes is advantageous as compared to the perfect crystalline models of the electrodes. However, if one is interested in studying transport in an idealized model system in order to understand fundamental aspects it might be important to avoid any kind of scattering that occurs at the electrode-device interface, e.g. to study the intrinsic transport properties of nanotubes, graphene nanoribbons or metallic nanowires neglecting the otherwise inevitable scattering at the interface between the bulk electrode and the nanotube or nanowire. Therefore a part of this thesis has been dedicated to the implementation of a module for calculating self-energies of perfect one-dimensional electrodes into the ALACANT package.

In Ch. 2 and App. C we have explained how to calculate the self-energies in the case of ideal one-dimensional leads of some finite width taking into account the overlap between

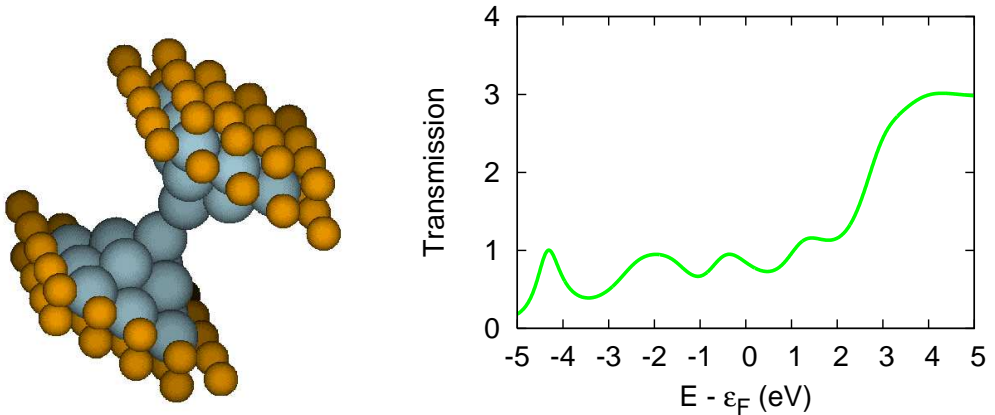


Figure 3.3: Left: Atomic structure of an Al nanocontact consisting of two perfect pyramids along the (001)-direction made up of 14 Al atoms (shown in grey) each. The surface atoms of the BL connected to the outermost planes of the nanocontact are also shown in a gold-like color. Right: Transmission of the Al-nanocontact shown on the left. The electronic structure of the device region was calculated on the LDA level of DFT employing the CRENBBS minimal basis set [96]. The tight-binding parameters of the BL are fitted to reproduce LDA electronic structure calculation of crystalline bulk Al and were taken from the handbook by Papaconstantopoulos [97].

the atomic orbitals of the atoms making up the one-dimensional lead. We now apply the developed theory to calculate the transport properties of an Al nanowire (Fig. 3.4) based on previous DFT electronic structure calculation of the nanowire on the LDA level. We use the CRYSTAL03 *ab initio* program for periodic systems [98] and employ the same CRENBBS minimal basis set with ECP as before [96]. The nanowire is along the 001 direction of the bulk crystal and the atoms have approximately bulk distances (nearest neighbor distance $\approx 2.8\text{\AA}$). The primitive unit cell of the nanowire (colored section in top panel of Fig. 3.4) consists of two planes containing 5 and 4 atoms, respectively. By defining a unit cell for the transport calculations consisting just of one primitive unit cell we can take into account interactions between nearest and next-nearest neighbor planes. With a unit cell consisting of two two primitive unit cells we can take into account inter-plane interactions up to fourth order.

Fig. 3.4 shows the DOS and transmission of the nanowire in the case that a) only interactions between up to next-nearest neighbor layers (red curves) and b) interactions between up to fourth nearest-neighbor layers (green curves) are taken into account. and we observe that DOS and transmission change when taking into account interactions of higher order. However, beyond fourth order the interactions become negligible, so that DOS and transmission do not change further when taking into account interactions beyond fourth order.

In order to compare with transport calculations describing the electrodes with the BL model, we calculate now the transport properties of a similar nanocontact as above but connected to two semi-infinite Al nanowires instead of the BL bulk electrodes. As in the

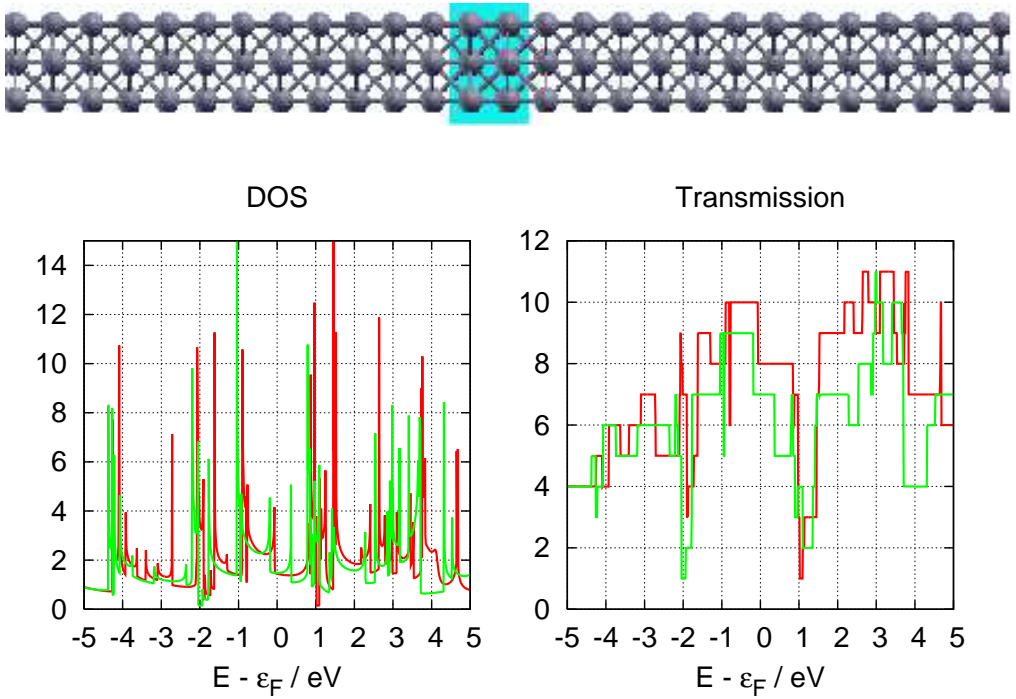


Figure 3.4: DOS and transmission for the infinite Al-nanowire shown above. Red curves in the DOS and transmission have been calculated taking into account interactions between nearest neighbor and next-nearest neighbor planes only while green curves have been calculated taking into account inter-plane interactions up to the fourth order.

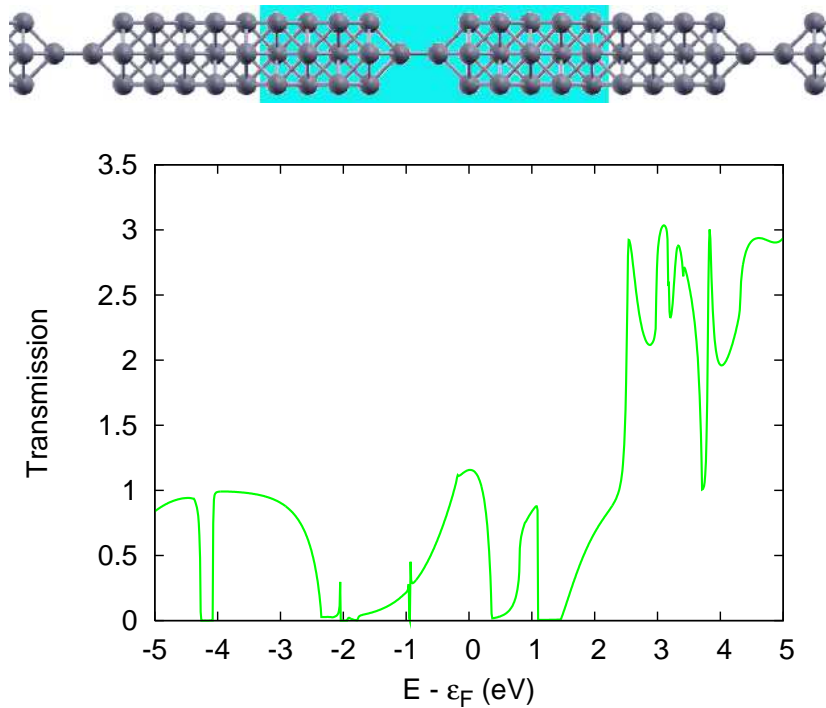


Figure 3.5: Transmission of the Al nanocontact shown above. The electronic structure of the nanocontact was calculated using a super-cell which is periodically repeated in one direction using the CRYSTAL03 package for periodic systems.

case of the perfect nanowire we calculate the electronic structure with the CRYSTAL03 program for periodic systems by defining a super-cell containing the nanocontact as shown at the top of Fig. 3.5. The super-cell has been chosen large enough so that the electronic structure of the outermost atoms of the super-cell has relaxed to its bulk value (i.e. of the perfect nanowire). The device Hamiltonian is then taken as the (on-site) super-cell Hamiltonian of the converged KS calculation. For the calculation of the self-energies of the semi-infinite leads the Hamiltonian of the unit cell and the coupling between neighboring unit cells are extracted from the electronic structure calculation of the perfect infinite nanowire.

From a comparison of Fig. 3.3 and Fig. 3.5 we see that although the two transmission curves differ from each other in the detail, some overall features in the two curves are actually very similar. For example, for energies of 2.5 eV above the Fermi level we observe a plateau of about 3 in the transmission and around the Fermi level the transmission is roughly one. On the other hand, in the case of the nanowire electrodes we see that the transmission function is much more irregular than in the case of the BL electrodes. The strong oscillations of the transmission function in the case of the nanowire electrodes are interference effects due to the finite width of the electrodes which also dependent very strongly on the actual width of the nanowire, so that the transmission curve changes strongly in dependence of the nanowire width. Only in the limit of very thick electrodes do these interference effects disappear [90]. On the other hand the transmission function in the case of the BL electrodes and is essentially independent of the details of the details of the electrode-device interface as long as the interface is not too close to the nanoscopic constriction[99].

3.3 Beyond density functional theory

The methodology presented in this chapter for calculating the transport properties of nanoscale conductors by combining DFT based electronic structure calculations and the NEGF works quite well for simple nanoscale conductors like metallic nanocontacts and nanowires, but has difficulties to cope with more complicated nanoscopic systems, like molecular conductors. One of the problems clearly is the spurious electronic self-interaction inherent in the standard approximations to the density functional like the LDA and GGA as discussed in Subsec. 3.1.3. As explained there, this problem can actually be cured by semi-empirical methods like using hybrid functionals [81] or the LDA+U method [83] that correct the spurious self-interaction, but have the disadvantage of introducing empirical parameters which have to be fitted to the material properties and thus there predictive power is limited.

A further problem of the DFT based quantum transport approach is that DFT is a ground state theory for the electron density while transport properties also involve the excited states of a system. Thus even if we knew the exact density functional (which we don't) it is not clear that the DFT based transport approach could actually give a good description of the transport properties. For the same reason there is no guarantee that an exact DFT would yield the magnitude of the band gap of insulators or the HOMO-LUMO gap of molecules. Indeed, it seems to be the case that EXX functionals which are already very close to an exact implementation of DFT improve only slightly on band gap in comparison with GGA. The hybrid functionals and LDA+U yield reasonable values of the HOMO-LUMO gap and of the band gaps of insulating solids because they go beyond

DFT.

Finally, while DFT is in principle a many-body theory in the sense that DFT yields the exact ground state electron density of the correlated many-body ground state if we knew the exact density functional, our KS based transport theory is ultimately an effective one-body theory as it makes use of the effective one-body KS orbitals and energies. Therefore the KS based transport theory presented here does not capture the true many-body effects due to electron correlations in the transport properties of nanoscopic conductors like the Kondo effect [100, 101].

There are several possibilities to solve these problems. The first is to use the time-dependent density functional theory (TDDFT) [102] which is a time-dependent extension of DFT. TDDFT allows to compute the time-dependent electron density of an interacting electron system in a time-dependent external potential. Since a time-dependent external field gives rise to electron excitations one can obtain the electron densities and energies of the excited many-body states from a TDDFT calculation. Thus TDDFT in combination with a good approximation for the density functional (i.e. self-interaction free) like e.g. EXX should give a very good description of the energy spectrum of metals, semiconductors and insulators as well as of molecules. Accordingly, combining the NEGF transport formalism with the KS formulation of TDDFT [103, 104] should improve systematically the description of the transport properties of molecular conductors where the transport approach based on ground-state DFT with the standard approximations to the functionals normally fails. However, TDDFT is computationally considerably more demanding than ground state DFT, and so is the EXX method in comparison with the standard approximations to DFT as explained before. Consequently, up until now TDDFT transport calculations have only been demonstrated for relatively simple model systems.

Alternatively, one can try to systematically improve the KS GF by many-body techniques. As explained at the end of Ch. 2, the Landauer formula becomes exact in the limit of small bias voltages and low temperatures even in the presence of strong electron correlations if the exact GF calculated from the many-body ground state is known. On the other hand, given a good approximation to the energy functional, DFT only guarantees a good approximation for the electron density but not for the GF of the many body ground-state. Thus it is not clear whether the KS GF calculated from the effective KS Hamiltonian actually gives a good approximation to the exact GF of the many-body ground state. But the KS GF is a good starting point for applying many-body techniques.

A systematic improvement of LDA is the GW perturbation theory where the electron self-energy is approximated by the product of the GF \hat{G} and the screened Coulomb interaction \hat{W} . GW gives an excellent description of many metallic systems and improves considerably the description of semiconductors and insulators improving e.g. the magnitude of the band gap. Therefore, various groups have recently made an effort to implement the GW method for the description of transport in nanoscopic conductors [105, 106].

However, when dealing with strongly correlated materials like e.g. transition metal oxides a perturbative approach like the GW method is no longer appropriate and more sophisticated methods are needed like e.g. the Dynamical Mean Field Theory (DMFT) [107]. The DMFT is based on the observation that electron correlation effects are most important for the strongly localized electrons of the d - and f -shells while they can normally be neglected for the delocalized s - and p -electrons. Therefore it is a good approximation to treat the electrons interactions only locally exact while the interaction with the rest of the system can be described on a mean-field level and thus enters only as an effective bath

3.3 *Beyond density functional theory*

via a self-energy. Thus the DMFT maps the interacting electron problem of an infinite system onto the Anderson impurity model with a single interacting site connected to an infinite systems [101]. In this way the DMFT approach calculates a locally exact GF that neglects the long-range correlations of the electrons which are normally unimportant. By extending the interacting region of the DMFT over atoms of the complete infinite system (Cluster-DMFT) one can in principle make DMFT as exact as necessary. However, the cost in computation increases exponentially with the size of the cluster.

4 Spin transport

We are primarily interested in electron transport through magnetic nanocontacts. Therefore we need to generalize the above formalism to systems without spin-degeneracy. Introducing the spin-degree of freedom the Hamiltonian and the Green's function (GF) of the device are now further subdivided into the following spin-dependent sub-matrices:

$$\mathbf{H}_D = \begin{pmatrix} \mathbf{H}_D^{\uparrow\uparrow} & \mathbf{H}_D^{\uparrow\downarrow} \\ \mathbf{H}_D^{\downarrow\uparrow} & \mathbf{H}_D^{\downarrow\downarrow} \end{pmatrix} \quad \mathbf{G}_D(E) = \begin{pmatrix} \mathbf{G}_D^{\uparrow\uparrow}(E) & \mathbf{G}_D^{\uparrow\downarrow}(E) \\ \mathbf{G}_D^{\downarrow\uparrow}(E) & \mathbf{G}_D^{\downarrow\downarrow}(E) \end{pmatrix} \quad (4.1)$$

The magnetization of the electrodes L and R is assumed to be along the z -direction only. Therefore the spin-mixing parts $\uparrow\downarrow$ and $\downarrow\uparrow$ of the self-energy matrices of the electrodes and hence the coupling matrices become zero:

$$\Sigma_{L,R}(E) = \begin{pmatrix} \Sigma_{L,R}^{\uparrow}(E) & 0 \\ 0 & \Sigma_{L,R}^{\downarrow}(E) \end{pmatrix} \Rightarrow \Gamma_{L,R}(E) = \begin{pmatrix} \Gamma_{L,R}^{\uparrow}(E) & 0 \\ 0 & \Gamma_{L,R}^{\downarrow}(E) \end{pmatrix}. \quad (4.2)$$

Thus the transmission can be resolved into the different spin-channels:

$$\begin{aligned} T(E) &= \text{Tr}[\Gamma_L(E) \mathbf{G}_D^\dagger(E) \Gamma_R(E) \mathbf{G}_D(E)] \\ &= \sum_{\sigma_1} \text{Tr}[(\Gamma_L(E) \mathbf{G}_D^\dagger(E) \Gamma_R(E) \mathbf{G}_D(E))_{\sigma_1 \sigma_1}] \\ &= \sum_{\sigma_1, \sigma_2} \text{Tr}[\Gamma_L^{\sigma_1}(E) (\mathbf{G}_D^{\sigma_1 \sigma_2}(E))^\dagger \Gamma_R^{\sigma_2}(E) \mathbf{G}_D^{\sigma_2 \sigma_1}(E)] \\ &= T^{\uparrow\uparrow}(E) + T^{\uparrow\downarrow}(E) + T^{\downarrow\uparrow}(E) + T^{\downarrow\downarrow}(E). \end{aligned} \quad (4.3)$$

where we have defined the spin-resolved transmission probabilities

$$T^{\sigma_1 \sigma_2}(E) := \text{Tr}[\Gamma_L^{\sigma_1}(E) (\mathbf{G}_D^{\sigma_1 \sigma_2}(E))^\dagger \Gamma_R^{\sigma_2}(E) \mathbf{G}_D^{\sigma_2 \sigma_1}(E)]. \quad (4.4)$$

$T^{\sigma_1 \sigma_2}$ is the probability that an electron enters the device from the left electrode with spin σ_1 and is emitted to the right with spin σ_2 . The meaning of the spin-channels is illustrated in Fig. 4.1.

Obviously, when there are no spin-mixing terms in the device Hamiltonian ($\mathbf{H}_D^{\uparrow\downarrow} = \mathbf{H}_D^{\downarrow\uparrow} = 0$) then the cross terms $T^{\uparrow\downarrow}$ and $T^{\downarrow\uparrow}$ must be zero, in real nanocontacts, leaving only the most important interactions to capture the essential physics of magnetic materials.

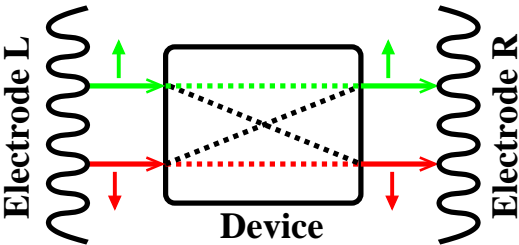


Figure 4.1: Scattering of spin channels. An electron with a certain spin-state σ coming in from the left can be scattered to another spin-state σ' of the right lead or conserve its spin when passing the device.

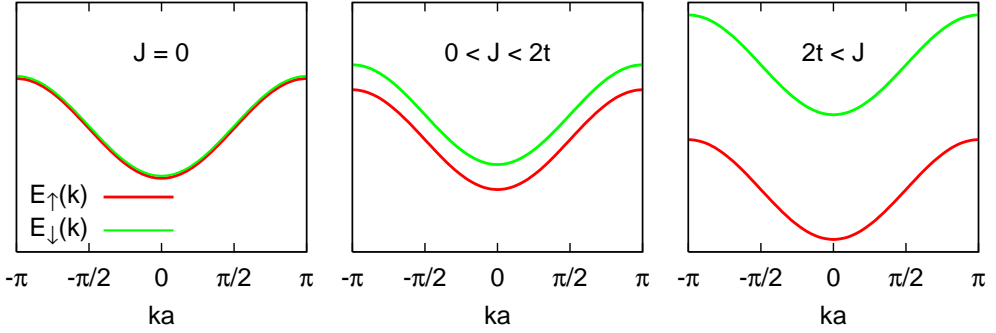


Figure 4.2: Energy dispersion for classical sd -model for homogeneous magnetization and for different limits of the exchange splitting J . For $J = 0$ (left) the chain is paramagnetic and for $J > 0$ it is magnetic. When J becomes larger than half of the band width $2t$ a gap opens between the two spin bands.

4.1 Domain wall scattering in the classical sd -model

What is the effect of a domain wall i.e. a magnetization reversal on a spin-polarized current? And how does this effect depend on the concrete magnetization profile? To answer this question we consider a tight binding chain with an exchange splitting J for the spin, i.e. the so-called classical sd -model:

$$\hat{\mathcal{H}} = -t \sum_{i,\sigma=\uparrow,\downarrow} \left(\hat{c}_{i\sigma}^\dagger \hat{c}_{i+1\sigma} + \hat{c}_{i+1\sigma}^\dagger \hat{c}_{i\sigma} \right) + \sum_i \vec{M}_i \cdot \vec{S}_i, \quad (4.5)$$

where \vec{M}_i is the magnetic moment of site i which interacts with the spin $\vec{S}_i = (\hat{\sigma}_x, \hat{\sigma}_y, \hat{\sigma}_z) \otimes |i\rangle\langle i|$. This gives rise to an exchange splitting for the spin at that site:

$$\vec{M}_i \cdot \vec{S}_i = -J(\sin \theta_i \hat{\sigma}_x + \cos \theta_i \hat{\sigma}_z) \otimes |i\rangle\langle i|. \quad (4.6)$$

To keep things simple we have assumed that the magnetization lies in the xz -plane, i.e. the y -component of the of the magnetization is zero, and that the exchange splitting J is the same for all sites. θ_i is the angle of the local magnetization with the z -axis. For a homogeneous magnetization (e.g. $\theta_i = 0$) we get two spin-bands that are split by an amount $2J$: $E_{\uparrow/\downarrow}(k) = -2t \cos(ka) \mp J$. This situation is depicted in Fig. 4.2 for different values of the parameter J . For $J = 0$ we have of course a the situation of a paramagnetic metal, while for $J > 0$ we have a ferromagnet. For the latter we can further distinguish two situations. For $J < 2t$ the two spin-bands overlap. This is the typical situation in ferromagnetic metals. On the other hand for $J > 2t$ a gap opens between the two spin-bands. And the model either describes a magnetic insulator (at half filling) or a half-metallic conductor where the conduction electrons are 100% spin-polarized.

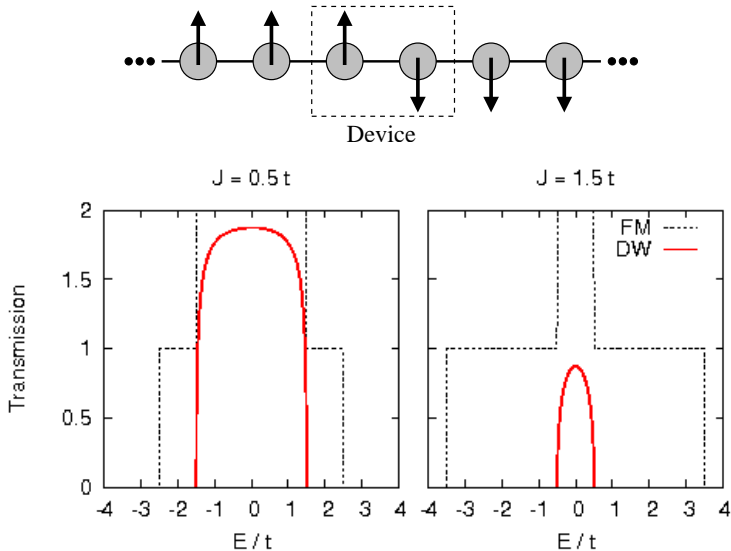


Figure 4.3: Abrupt domain wall in classical sd -model. Top graph: Sketch of model. Bottom left: Domain wall transmission (solid red line) for $J = 0.5t$ compared to transmission of homogeneous ferromagnetic chain for that parameter. Bottom right: The same as left graph but for $J = 1.5t$.

4.1.1 Abrupt domain wall

We now discuss the effect of an abrupt domain wall on the transport properties for the ferromagnetic phase of the classical sd -model, i.e. when $J > 0$. As depicted in Fig. 4.3 the magnetization of each of the leads is homogenous, but aligned opposite to each other so that there is a sharp magnetization reversal in the device region. However, the magnetization axis is the same for all atoms (we choose z , i.e. $\theta_i \in \{0, \pi\}$), so that the spin-mixing term $\propto \hat{\sigma}_x$ in the Hamiltonian (4.5) is zero.

When $J > 2t$ there is no overlap between the two spin bands so that the transmission is simply zero for all energies since an electron coming in on one of the leads cannot be transmitted through the device to the other lead conserving also its spin. But since there is no spin-mixing term in the Hamiltonian the transmission probabilities involving a spin flip are zero, i.e. the spin is conserved. Thus in the case of the abrupt domain wall there can only be a nonzero transmission when the two spin bands do overlap. Note, that even in the case where there is an overlap between the two spin-bands the transmission becomes zero for energies where the two bands do not overlap as can be seen from the two lower panels of Fig. 4.3. Thus for a half-metallic conductor, (i.e. spin-polarization is 100% near the Fermi level), the effect of a domain wall is maximal, giving theoretically an infinite resistance for an abrupt domain wall. This is what makes half-metals the ideal materials for spintronics applications.

4 Spin transport

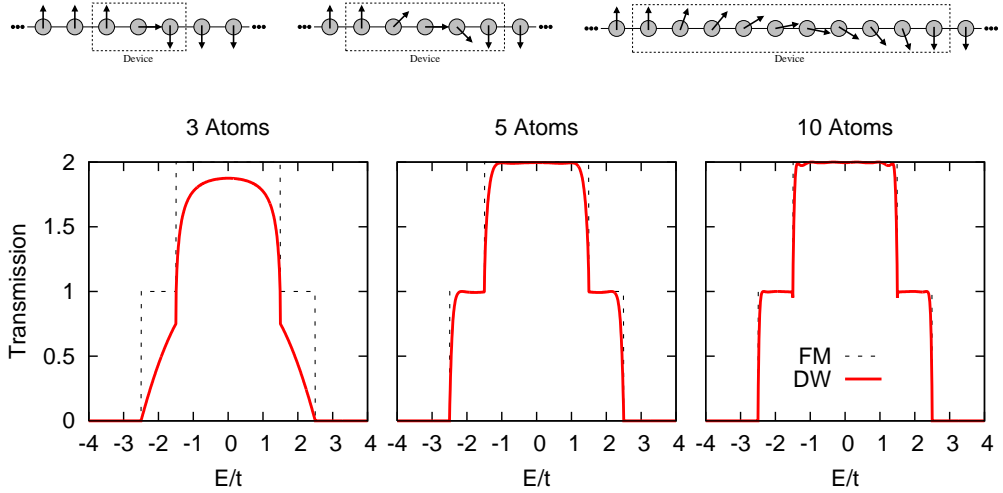


Figure 4.4: Smooth domain walls. The upper panels show 3 domain walls of different lengths. Upper left: Domain wall with 3 atoms. Upper center: Domain wall with 5 atoms. Upper right: Domain wall with 10 atoms. The magnetization angle θ_i changes linearly with the atom position i inside the domain. The lower panels show the corresponding transmissions of the domain walls (solid red lines) in comparison with the homogeneous ferromagnetic chain (dashed black lines) with same parameter J . $J = 0.5t$ in all 3 cases.

4.1.2 Smooth domain walls

Instead of the abrupt magnetization reversal the magnetization could change smoothly, as illustrated in the top panels of Fig. 4.4. What would be the effect of this on the transmission of the domain wall? Due to the smooth change of magnetization in the domain wall, the spin-mixing term $\propto \hat{\sigma}_x$ will not be zero anymore and therefore the spin-flipping channels will open, i.e. $T^{\uparrow\downarrow}$ and $T^{\downarrow\uparrow}$ will become finite. Thus one expects that the domain wall resistance decreases. This is exactly what happens, as can be seen from the bottom panels of Fig. 4.4 which show the transmissions for different lengths of the domain walls when the magnetization angle θ_i changes linearly with the position.

We observe that in general the transmission increases with increasing smoothness (i.e. increasing domain length) of the domain. In particular, it becomes different from zero at energies where there is no overlap between the two spin-bands. This is due to the spin-mixing by the non-collinear magnetization profile of the domain wall which allows electrons to spin-flip when crossing the domain wall. The spin-flip process becomes more and more adiabatic when increasing the smoothness of the domain wall thus resulting in fewer backscattering for incoming electrons. Therefore the perfect transmission of the chain with homogenous magnetization is finally recovered for very smooth domain walls as we can see in Fig. 4.4 for the case of the domain wall with a length of 10 atoms.

4.2 One-dimensional Hubbard model

The classical *sd*-model discussed in the previous section is a rather simplistic model for a magnetic material. There the spin-polarization of the conduction electrons is due to the interaction of the electron spin with a classical magnetic moment localized on an atom that gives rise to an exchange splitting J of the electrons. However, in reality the spin-polarization of the electrons in a ferromagnetic metal does not arise from the interaction with a local magnetic moment but is a direct consequence of the Coulomb interaction between the electrons and the Pauli exclusion principle. The Coulomb interaction gives rise to the so called exchange term when the two spins of the two electrons are both in the same direction. This term is usually negative, i.e. associated with an energy gain for the electrons. If this energy gain is greater than the loss in kinetic energy which is associated with the two electrons occupying the same spin state then usually the electron spin of the material will prefer to align parallel. This is the reason why magnetism in material normally originates from the *d*-electrons which are strongly localized at the atoms so that the hopping to the neighbor atoms is rather small minimizing the loss in kinetic energy.

The most simple model that captures this physics is the Hubbard model. An introduction to the Hubbard model can be found for example in Refs. [108], and [109]. The Hubbard model consists of only two spin-orbitals per atom which can split in energy because of the on-site Coulomb repulsion U . Atoms are coupled only to their nearest neighbors by a hopping t , and Coulomb interactions between atoms are neglected. Thus the Hamiltonian of the one-dimensional Hubbard model is given by

$$\hat{H} = \hat{T} + \hat{V}, \quad \text{where } \hat{V} = U \sum_i \hat{n}_{i\uparrow} \hat{n}_{i\downarrow} \quad \text{and} \quad \hat{T} = -t \sum_{i,\sigma} \hat{c}_{i\sigma}^\dagger \hat{c}_{i+1\sigma} + \text{h.c.} \quad (4.7)$$

\hat{T} is the so-called hopping term, which describes the kinetic energy Hamiltonian in the tight-binding approximation, and \hat{V} is the on-site Coulomb interaction. As pointed out above the Hubbard model is employed to describe *d*-band materials, i.e. materials whose electronic properties are determined by the *d*-electrons which are responsible for magnetism.

In the following we will study the formation of domain walls in one-dimensional ferromagnetic chains with the Hubbard model, and their electronic transport properties. In order to mimic the situation in nanocontacts where it is expected that a domain wall builds up in the atomic-size constriction [39], we will restrict the formation of the domain wall to a finite region of the chain. Outside that region the electronic and magnetic structure is assumed to be that of the homogenous chain. The formation of such a constrained domain wall will be calculated self-consistently following the Hartree-Fock approximation (HFA) as explained in the following section.

4.2.1 Hartree-Fock approximation – the Stoner model

The HFA to the Hubbard model is also called the Stoner model [110]. Here we will treat the one-dimensional Stoner model in the non-collinear unrestricted HFA (NC-UHF, see App. E) in order to allow the formation non-collinear magnetization profiles of the domain wall.

In the NC-UHF we find the following Fock matrix for the Hubbard Hamiltonian (4.7):

$$F_{ij}^{\sigma_1\sigma_2} = T_{ij}\delta_{\sigma_1\sigma_2} + U \delta_{ij} \left(\delta_{\sigma_1\sigma_2} (P_{ii}^{\uparrow\uparrow} + P_{ii}^{\downarrow\downarrow}) - P_{ii}^{\sigma_1\sigma_2} \right). \quad (4.8)$$

4 Spin transport

The first term in the brackets is the Hartree contribution which describes the pure Coulomb repulsion, the second term is the Fock contribution describing the Coulomb exchange interaction. The Fock terms for $\sigma_1 = \sigma_2$ cancel exactly with the Hartree-terms $\propto \rho_{ii}^{\sigma\sigma}$ with $\sigma = \sigma_1 = \sigma_2$ which present an unphysical self-interaction of the electrons, correcting thereby the self-interaction error.

The density matrix can be expressed through the creation and annihilation operators:

$$P_{ij}^{\sigma_1\sigma_2} = \langle \hat{c}_{i\sigma_1}^\dagger \hat{c}_{j\sigma_2} \rangle^* \quad (4.9)$$

so the Fock-operator corresponding to the Fock matrix (4.8) can be expressed in 2nd quantization as:

$$\hat{\mathcal{F}} = \hat{\mathcal{T}} + U \sum_{i,\sigma} \langle \hat{n}_{i\sigma} \rangle \hat{n}_{i\bar{\sigma}} - U \sum_{i,\sigma} \langle \hat{c}_{i\sigma}^\dagger \hat{c}_{i\bar{\sigma}} \rangle^* \hat{c}_{i\sigma}^\dagger \hat{c}_{i\bar{\sigma}} \quad (4.10)$$

In the next subsection we will study the situation of a homogeneous chain in the Stoner model.

4.2.2 Homogeneous Chain

In an infinite chain all sites are equivalent. Therefore the Stoner model Hamiltonian (4.10) becomes homogeneous, i.e. the expectation values $\langle \hat{n}_{i\sigma} \rangle$ are the same at each site i , $\langle \hat{n}_{i\sigma} \rangle = \bar{n}_\sigma$. This allows us to choose the quantization axis for the spin, say z , so the spin-mixing terms in the Fock operator vanish:

$$\hat{\mathcal{F}} = \hat{\mathcal{T}} + U \sum_{i,\sigma} \bar{n}_{\bar{\sigma}} \hat{n}_{i\sigma} \quad (4.11)$$

We can diagonalize the Fock matrix of the homogenous chain by introducing Bloch states, $|k\rangle = \frac{1}{\sqrt{2\pi}} \sum_j \exp(ikj) |j\rangle$:

$$\hat{\mathcal{F}} = \sum_{k,\sigma} F^\sigma(k) \hat{c}_{k\sigma}^\dagger \hat{c}_{k\sigma}, \quad (4.12)$$

with

$$F^\sigma(k) = \sum_{j=-1}^1 \exp(ikj) \langle 0\sigma | \hat{\mathcal{F}} | j\sigma \rangle = \epsilon(k) + U n_{\bar{\sigma}} \quad (4.13)$$

ϵ_k is the kinetic energy of the Bloch wave $|k\rangle$ (Hamiltonian \hat{T}):

$$\epsilon(k) = 2t \cos(k). \quad (4.14)$$

The two resulting spin-bands (energy $F^\sigma(k)$) have the dispersion relation $\epsilon(k)$ of the non-interacting chain but are split by $U(n_\uparrow - n_\downarrow)$ in energy. The corresponding DOS \mathcal{D} can be written as a sum of the spin-up and the spin-down DOS:

$$\mathcal{D}(\epsilon) = \mathcal{D}_\uparrow(\epsilon) + \mathcal{D}_\downarrow(\epsilon). \quad (4.15)$$

where

$$\mathcal{D}_\sigma(\epsilon) = \begin{cases} \frac{1}{\pi} \frac{d}{d\epsilon} \arccos((\epsilon - U n_{\bar{\sigma}})/2t) & ; \text{ if } |\epsilon - U n_{\bar{\sigma}}| \leq 2|t| \\ 0 & ; \text{ elsewhere} \end{cases} \quad (4.16)$$

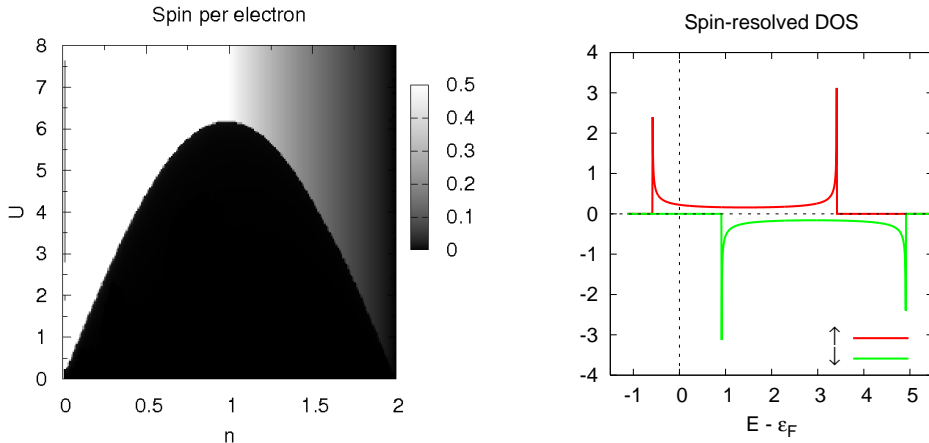


Figure 4.5: Self-consistently calculated magnetization phase diagram for the one-dimensional Stoner model (left) and spin-resolved DOS (right) for the ferromagnetic (FM) phase (filling $n = 0.25$, Coulomb parameter $U = 6$) of the one-dimensional Stoner model. The dotted vertical line indicates the Fermi level.

The spin-dependent occupation numbers n_\uparrow and n_\downarrow are given by integrating the spin-resolved DOS up to the Fermi energy μ :

$$\begin{aligned}
 n_\sigma(\mu) &= \int_{-\infty}^{\infty} d\epsilon \mathcal{D}_\sigma(\epsilon) f(\epsilon - \mu) = \frac{1}{\pi} \int_{Un_{\bar{\sigma}} - 2|t|}^{Un_{\bar{\sigma}} + 2|t|} d\epsilon \frac{d}{d\epsilon} \arccos((\epsilon - Un_{\bar{\sigma}})/2t) f(\epsilon - \mu) \\
 &= \begin{cases} 0 & ; \mu \leq Un_{\bar{\sigma}} - 2|t|, \\ \frac{1}{\pi} \arccos((\mu - Un_{\bar{\sigma}})/2t) & ; |\mu - Un_{\bar{\sigma}}| \leq 2|t|, \\ 1 & ; \mu > Un_{\bar{\sigma}} + 2|t|. \end{cases}
 \end{aligned} \tag{4.17}$$

We fix the number of electrons $n = n_\uparrow + n_\downarrow$ per unit cell (also called filling factor), the hopping parameter t and the Coulomb parameter U . The self-consistent solution of the problem then yields the chemical potential μ , the occupation numbers n_\uparrow and n_\downarrow , and thus the spin-density $s = n_\uparrow - n_\downarrow$ and the total energy per unit cell.

The left hand side of Fig. 4.5 shows the phase diagram of the self-consistently calculated Stoner model for the magnetization (spin per electron) of the chain in dependence of the on-site Coulomb repulsion U and the filling n . Obviously there is a ferromagnetic (FM) and a paramagnetic (PM) phase. Since we want to study transport in magnetic materials we are only interested in the FM phase here. In the FM phase the Stoner model is a so-called half-metal, meaning that the electrons are completely spin-polarized,

as illustrated on the right hand side of Fig. 4.5: Only one of the two spin bands is partially filled, while the other is always empty. The electrons at the Fermi level and thus the conduction electrons are 100% spin-polarized. This has important consequences for the spin transport. First, at the Fermi level only one transport channel (the majority spin channel) is open, leading to a conductivity of $1 G_0$. Second, in the case of a domain, the MR will be 100% for an abrupt DW since all traversing electrons will be blocked. The latter will be discussed in the next section in more detail.

4.3 DW formation and scattering

As said in the beginning of this chapter the DW formation will be restricted to a finite region of the chain - the device region (D). We will make use of the self-consistent procedure described in Ch. 3 for computing the electronic structure of an open system in the HFA. The semi-infinite regions to the left and right of D, i.e. the electrodes L and R, will have bulk electronic structure which does not change during the self-consistent calculation of the DW formation. In order to give the correct magnetic boundary conditions for the formation of a DW the magnetization of L and R will be aligned antiparallel (AP).

Following (2.33), the GF of the device region is given by

$$\mathbf{G}_D(E) = (E - \mathbf{F}_D - \mathbf{\Sigma}_L(E) - \mathbf{\Sigma}_R(E))^{-1}, \quad (4.18)$$

where F_D is the Fock matrix of the device in the NC-UHF approximation for the Stoner model. The self-energy matrices can be subdivided into the spin-resolved self-energy matrices $\mathbf{\Sigma}_{L,R}^\uparrow$ and $\mathbf{\Sigma}_{L,R}^\downarrow$ following (4.2) which can be calculated from electrodes' self-energies following (2.34,2.35).

The left and right lead are described by tight-binding chains with a spin-dependent energy shift of $\epsilon_\sigma = Un_{\bar{\sigma}}$. For this case the Dyson equations (2.41) and (2.42) can be solved analytically and one obtains for the spin-dependent retarded self-energy of the left (l) and right lead (r):

$$\Sigma_{l,r}^\sigma(E) = \begin{cases} \frac{E-\epsilon_\sigma}{2} + \frac{\sqrt{(E-\epsilon_\sigma)^2-4t^2}}{2}; & \text{for } E < \|2t\| \\ \frac{E-\epsilon_\sigma}{2} - \frac{i\sqrt{(E-\epsilon_\sigma)^2-4t^2}}{2}; & \text{for } \|E\| \leq \|2t\| \\ \frac{E-\epsilon_\sigma}{2} - \frac{\sqrt{(E-\epsilon_\sigma)^2-4t^2}}{2}; & \text{for } E > \|2t\| \end{cases} \quad (4.19)$$

We follow the procedure described in Sec. 3.2 adapted to the HFA to calculate self-consistently the formation of a DW in the AP configuration. The magnetization of an atom is defined as the total atomic spin normalized to the number of electrons of the atom:

$$\vec{M}(i) = \frac{\langle \vec{S}(i) \rangle}{n(i)}, \quad (4.20)$$

where the expectation value of the atomic spin is obtained from the density-matrix:

$$\langle \vec{S}(i) \rangle = \frac{1}{2} \begin{pmatrix} 2\text{Re}[\rho_{ii}^{\uparrow\downarrow}] \\ 2\text{Im}[\rho_{ii}^{\uparrow\downarrow}] \\ \rho_{ii}^{\uparrow\uparrow} - \rho_{ii}^{\downarrow\downarrow} \end{pmatrix}. \quad (4.21)$$

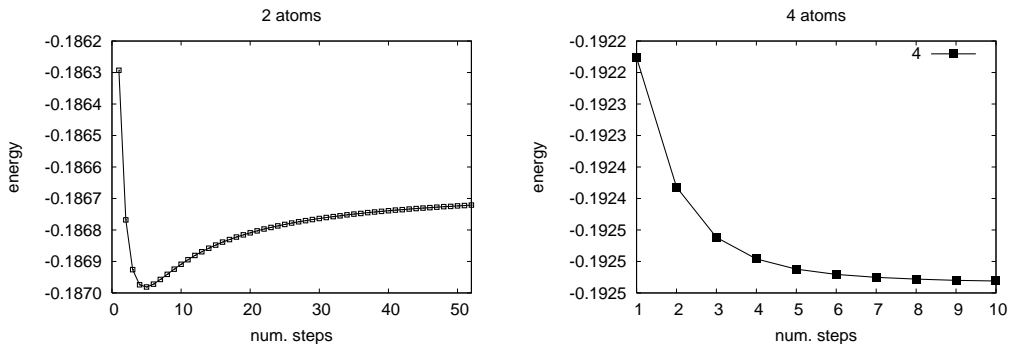


Figure 4.6: Total energy following eq. (3.27) corrected for double-counting following eq. (3.25) in dependence of number of steps in the self-consistent DW formation for a domain length of (a) 2 atoms and (b) 4 atoms. Filling $n = 0.1$ and Coulomb parameter $U = 3$.

For a “smooth” DW, i.e. a DW where the magnetization angle changes smoothly with the position, the initial guess must have non-collinear magnetization vectors. In the following we will start with an initial guess representing a “linear” DW, i.e. a DW where the magnetization angle changes linearly with the position. On the other hand if we want to calculate the formation of an abrupt domain we have to start with an initial guess with only collinear magnetization vectors, i.e. the magnetization of each atom of the domain must be along the same axis (the z -axis) as the magnetization of the electrodes.

Fig. 4.6 shows the total energy of two constrained smooth DWs of different length (2 and 4 atoms) after eqs. (3.25) and (3.27) for each step in the self-consistent procedure until convergence of the density matrix. Obviously, in the case of a domain length of only two atoms the energy is *not* minimized. This is not surprising if we consider that for such a short domain the electronic structure of the electrodes has surely not relaxed to the bulk electronic structure as we have assumed. In order to minimize the energy we would have to recalculate the electronic structure of the electrodes as well, and not let it fixed during the self-consistency as we do here. But here we are interested in the formation of constrained domains, since in real nanocontacts the DW formation is also constrained by the geometry of the contact [39]. Since we have neglected the geometrical part of the problem by considering one-dimensional chains we have to constrain the DW artificially. This of course leads to a constrained variational problem, so that not the energy is minimized but the free energy defined in a proper way. We note that already for a domain of 4 atoms (right panel of Fig. 4.6) the constrained variational search minimizes the total energy of the system. The assumption of a fixed bulk electronic structure in the electrodes becomes better with increasing DW length.

Nevertheless the resulting energies can be compared to each other and to the energy of the bulk chain. Thus we can obtain the cost in energy for the formation of a DW of a certain length. Fig. 4.7 shows the DW formation energy per atom as a function of the DW length in comparison to the energy of the FM bulk chain. The homogeneous chain has of course the lowest energy since the ferromagnetic solution favors the parallel alignment of the electron spins to increase the gain in exchange energy. As the DW length is increased the energy per atom shrinks because locally the ferromagnetic solution is recovered as the

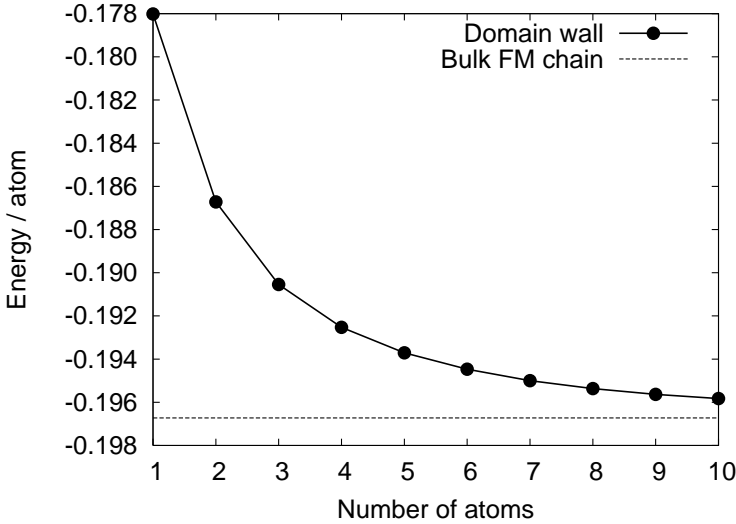


Figure 4.7: Total energy following eqs. (3.25) and (3.27) as a function of the DW length for the self-consistent DW formation. Filling $n = 0.1$ and Coulomb parameter $U = 3$.

DW becomes smoother with increasing domain length.

The smoothing of the DW with increasing domain length is demonstrated in Fig. 4.8. The upper panels of Fig. 4.8 show the angle $\theta(i)$ of the magnetization vector on the i -th atom in the device region (=domain) for a domain length of (a) 6 atoms and (b) 10 atoms, respectively, while the lower panels show the corresponding magnetization vectors. In the first place, one notes that the angle θ for atoms inside the domain (atoms 1 to 6 in (a), and 1 to 10 in (b)) depends almost linear on the position, and that this dependence approaches a perfect line with increasing domain length. In the second place, one observes that the *rotation angle* $\Delta\theta = \theta(i+1) - \theta(i)$ between the last (first) atom of the left (right) electrode and the first (last) atom of the domain is bigger than the rotation angles inside the domain. This difference between the rotation angles $\Delta\theta$ between electrode and device and inside the device becomes also smaller with increasing domain length. Finally, we mention that also the atomic charge $n(i)$ and the length of the magnetization vector $S(i)$ (not shown) varies slightly ¹ with the position, and that the deviation from the bulk values of the atomic charge and the magnetization becomes also smaller with increasing domain length. In summary, the DW becomes smoother with increasing domain length approaching a *linear DW* where the magnetization angle depends linearly on the position and as well the magnitude of the magnetization as the atomic charge are constant and equal to that of the FM bulk chain thereby locally recovering the FM state.

In turn the magnetization profile of the DW affects the electron transport through the DW. Fig. 4.9a shows the total transmission as a function of the energy relative to the Fermi energy in the P case and for some domain lengths (2,4,10 atoms) in the AP case. One observes that the transmission for the AP case deviates globally from the perfect transmission in the P case. The deviation shrinks with increasing length of the domain. For a domain length of 10 atoms the perfect P transmission is almost recovered. The effect is especially strong near the Fermi energy as the close-up in Fig. 4.9a shows. Near

¹ $n(i)$ deviates in both directions by less than 2% from the bulk value $n = 0.1$ for (a) and (b), while $S(i)$ is smaller by 4-10% for (a) and by 2-4% for (b) than the bulk magnetization $S = n/2$.

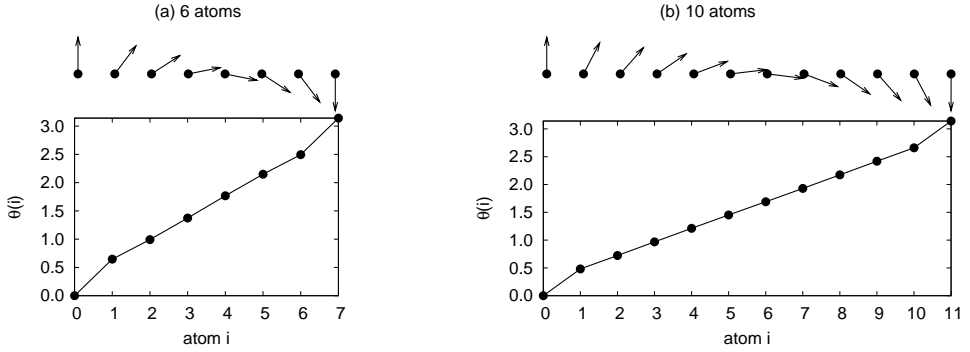


Figure 4.8: DW profiles for (a) 6 atoms and (b) 10 atoms in the device region. The upper panel shows the magnetization vector for each atom in the xz -plane, and the lower panel the rotation angle $\theta(i)$ of the magnetization vector as a function of the atom position i . The leftmost (0) and the rightmost (7 in (a) and 11 in (b), respectively) atom belong to the left and right electrode, respectively, which have bulk electronic structure. Filling $n = 0.1$ and Coulomb parameter $U = 3$.

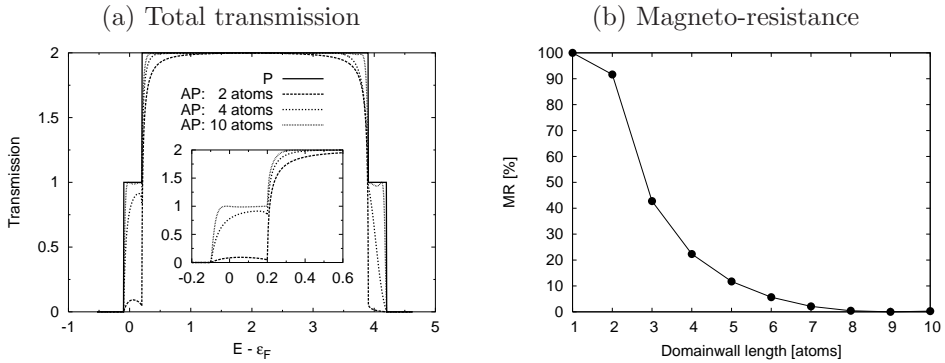


Figure 4.9: (a) Total transmission in dependence of the energy (relative to the Fermi energy ϵ_F) of one-dimensional chain in the Stoner model for some domain lengths in the AP configuration compared to the perfect transmission in the P configuration. (b) Magneto-resistance (using def. $MR_1 = (T_P - T_{AP})/T_P$) as a function of the domain length. Filling $n = 0.1$, Coulomb parameter $U = 3$ for both (a) and (b).

4 Spin transport

the Fermi energy only one spin-band contributes to the conduction in the P case, since the ferromagnetic chain is a half-metal as explained in the previous section. Thus for an abrupt domain the transmission is completely blocked near the Fermi level: An electron passing the DW has to change its spin to travel on in the other electrode since only one spin-state is allowed near the Fermi level, and the electrodes are oppositely magnetized in the AP case. But an abrupt domain does not allow the electrons to change their spin because of the absence of spin-mixing terms in the spin-polarized Hamiltonian. On the other hand a non-collinear magnetization of the domain gives rise to spin-mixing terms which can rotate the spin state of an incoming electron. The transmission probability becomes higher the smaller the rotation angle of the magnetization vector between neighboring atoms. Therefore in the case of a non-collinear domain of 2 atoms the transmission is nonzero but very small compared to the P transmission. Making the domain larger the rotation angles decrease - the domain becomes more smooth - and the transmission probability creases until recovering the perfect transmission of 1 in the case of an adiabatic DW which locally resembles the ferromagnetic solution. As a consequence the MR decreases with increasing length of the domain, as demonstrated in Fig. 4.9b. For an abrupt domain the MR is 100% as the DW blocks the transmission completely while for a very smooth domain the MR goes to zero: The AP conductance becomes the same as the P conductance.

Finally, we will have a look at the spin-resolved conductance channels. Fig. 4.10 shows the contributions of the individual spin-channels (4.4) to the total transmission. As illustrated in Fig. 4.1 $T_{\uparrow\uparrow}$ ($T_{\downarrow\downarrow}$) gives the probability of an electron coming from the left lead with spin-up (spin-down) and being transmitted to the right electrode conserving its spin while $T_{\uparrow\downarrow}$ ($T_{\downarrow\uparrow}$) is the probability of an electron entering with spin-up (spin-down) and flipping its spin when being transmitted to the right. The $\uparrow\uparrow$ - and $\downarrow\downarrow$ -channel do not contribute anything to the transmission near the Fermi energy, in accordance with the above reasoning that in the half-metallic limit only one spin-band in the electrodes contributes to the conductance, so that in the AP case an electron can not conserve its spin when being transmitted to the other electrode. On the other hand a non-collinear magnetization of the domain opens the $\uparrow\downarrow$ - and $\downarrow\uparrow$ -channels which do not contribute to the transmission in the P case. But only the $\uparrow\downarrow$ -channel gives rise to a non-zero transmission near the Fermi level because of the electrons near the Fermi energy being completely spin-up polarized in the left and spin-down polarized in the right electrodes. The contribution of the $\uparrow\downarrow$ - and $\downarrow\uparrow$ -channels to the total transmission grows with increasing domain length as the spin-mixing becomes more and more important. For the same reason the contribution of the $\uparrow\uparrow$ - and $\downarrow\downarrow$ -channel vanish with increasing domain length. Finally, in the limit of an adiabatic DW only the $\uparrow\downarrow$ - and $\downarrow\uparrow$ -channels contribute and have the same transmission as the $\uparrow\uparrow$ - and $\downarrow\downarrow$ -channel in the P case illustrating once again how the ferromagnetic case is recovered locally for an adiabatic DW.

4.4 Summary

In summary, we have calculated the transmission through domain walls in the classical sd -model and the Stoner model taking into account non-collinear magnetization profile. For the classical sd -model we have assumed a simple linear dependence of the magnetization angle with the position inside the domain like in the work by Tatara *et al.* [111], and obtain similar results. Increasing the length of the domain wall its smoothness increases

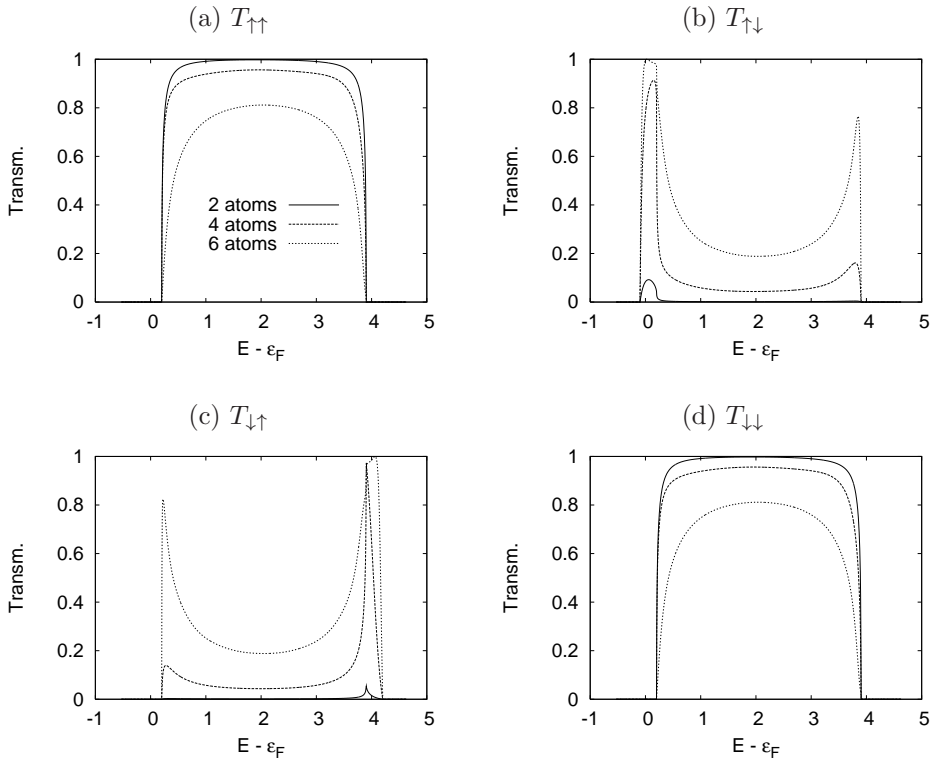


Figure 4.10: Transmission of individual spin-channels in dependence of the energy relative to the Fermi level for AP configuration and domain lengths of 2, 4 and 8 atoms. Filling $n = 0.1$, Coulomb parameter $U = 3$.

4 Spin transport

giving rise to a general increase of the transmission until for very smooth domain walls the perfect transmission of the homogenous ferromagnetic chain is recovered. This can be understood by the fact that a non-collinear magnetization allows electrons to spin-flip while crossing the domain wall, so that electrons can be transmitted elastically even at energies where there is no overlap between spin-bands. In the limit of a perfectly smooth domain wall the spin of an incoming electron is flipped adiabatically while crossing the domain thus eliminating the backscattering by the magnetic structure.

On the other hand, we also calculated the formation of a domain wall in the Stoner model. We find that also here the local magnetization vector changes more smoothly, with increasing domain length, although for a finite domain length the DW is not simply “linear”, i.e. the magnetization angle does not change linearly with the position inside the domain as was assumed for the classical *sd*-model in 4.1 and by Tatara *et al.* [111]. Moreover the magnitude of the magnetization vector is not homogeneous for a finite domain length, but is modulated along the domain, and thus is different from the magnetization of the ferromagnetic bulk. The deviation from the linear DW with respect to the magnetization angles and the modulation of the magnitude of the magnetization becomes bigger the smaller the domain, thus introducing extra-scattering in comparison to the perfect linear DW.

5 Ni nanocontacts

The observation of huge magneto-resistance (MR) in ferromagnetic nanocontacts [28] comparable or even exceeding the celebrated GMR effect [21] has given rise to a strong interest in these systems over the last years because of its possible implications in the context of nanoscale spintronics applications [27, 28, 29, 30, 31, 32, 33, 34, 35, 36, 38, 37]. The observed huge MR was explained theoretically by the following reasoning: It is expected that the magnetizations of the two sections of the wire which are connected via the atomic-size contact align antiparallel (AP), so that the overall magnetostatic energy is reduced. Then a fairly sharp domain-wall (DW) should form at the atomic-size contact, since the cost in exchange energy for the formation of the DW is minimized due to the low coordination of the contact atom [39]. It has been further argued that the sharp DW should give rise to strong ballistic spin scattering resulting in a large extra contribution to the ballistic resistance in the AP configuration [40, 41]. Applying an external magnetic field the magnetizations of the two wires will align parallelly (P) erasing the DW at the neck, and thus eliminating the extra contribution to resistance. The quantity characterizing the effect is the magneto-resistance MR which is defined as the difference between the resistances in the AP configuration R_{AP} and the P configuration R_P normalized to either R_{AP} (MR_1) or R_P (MR_2). The definition of MR as $MR_1 = (R_{AP} - R_P)/R_{AP}$ is bounded, i.e. $MR_1 \leq 100\%$ while the second definition of MR as $MR_2 = (R_{AP} - R_P)/R_P$ has no upper limit, i.e. $MR_2 < \infty$. In the literature both definitions are used. Following the above reasoning high values of MR —named “ballistic” MR (BMR) for its origin in ballistic electron scattering— in ferromagnetic metal nanocontacts could be expected.

However, BMR in nanocontacts has been a controversial topic since its first observation: While some groups have measured huge values of BMR in Ni nanocontacts, comparable to or even exceeding GMR values (typically $MR_2 \approx 225\%$) [28, 30, 32, 33, 35], other groups have obtained moderate BMR values [31, 36], do not measure any MR effect [34], or even obtain negative BMR values [27]. The question of huge BMR in ferromagnetic nanocontacts and its origin is a very important one because of its expected impact on the magneto-electronics industry.

In this chapter electron transport through atomic-size Ni nanocontacts and the effect of the formation of a domain wall in the atomic-size constriction on the transport-properties is investigated theoretically using *ab initio* methods. An atomic-size nanocontact is a constriction of just one atom in diameter connecting two sections of a wire. Within the atomic-size constriction the electrons are confined to effectively one dimension. In order to understand the behavior of the electrons in a material at low dimensions it is therefore reasonable to investigate the electronic structure of perfect one-dimensional monatomic wires before investigating the more complicated situation of a nanocontact with a realistic geometry. The investigation of monatomic nanowires of 3d-transition metals with *ab initio* methods has been performed earlier by Smogunov *et al.* [112, 113]. As a precursor to the work on nanocontacts we have repeated the *ab initio* electronic structure calculations

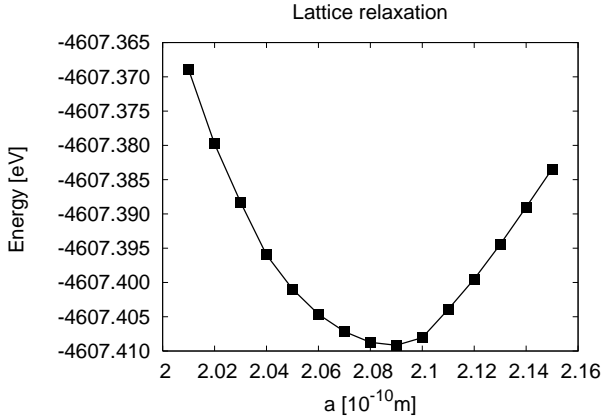


Figure 5.1: Optimization of the lattice spacing a of the ferromagnetic monatomic Ni chain calculated with CRYSTAL using LSDA and the CRENBL pseudo-potential + basis set.

of Ni chains, and fully reproduce their results. The insight gained by the calculations on perfect one-dimensional monatomic wires will help us to analyze and interpret the results for nanocontacts with realistic geometries.

Ni is a 3d-transition metal that crystallizes in the face-centered cubic (FCC) crystal structure. The bulk material is ferromagnetic with an atomic magnetic moment of $0.6\mu_B$ which is considerably less than that of his immediate neighbor to the left in the periodic table, Co ($1.7\mu_B$). The magnetism of Ni originates from the electrons in the d-bands which are spin-split. The s-band is not spin-split and thus the s-electrons do not contribute to the magnetism.

The electronic structure of bulk Ni is quite well described within the local spin density approximation (LSDA)[114] of density-functional theory (DFT) [115]. Therefore we will at first perform *ab initio* calculations of Ni wires and nanocontacts at the LSDA level (Sec. 5.1 and Sec. 5.2). Then in Sec. 5.4 we will compare the LSDA results with results obtained using the hybrid-functional B3LYP which corrects for the self-interaction error inherent in LSDA as discussed in Ch. 3.

5.1 Monatomic Ni chain

In order to illuminate the properties of the electronic structure of Ni at low dimensions we first study the electronic structure of infinite monatomic chains of Ni using the quantum chemistry program CRYSTAL [98], which allows to calculate the electronic structure of periodic systems with standard *ab initio* methods like the Hartree-Fock approximation (HFA) and DFT. However, no evidence of chain formation between Ni nanocontacts have been reported to date in contrast to Au or Pt. This is also supported by our *ab initio* simulations of breaking Ni contacts presented in the next section. Nevertheless the results for the ideal chains will help us to analyze and interpret the more complex results obtained for the more realistic contact geometries of the next section.

First, we optimize the geometry of the chain, i.e. we search for the lattice spacing a of the chain which minimizes the energy. Fig. 5.1 shows the energy in dependence of the lattice spacing a between 2\AA and 2.2\AA obtained with the LSDA functional and the CRENBL basis-set with core pseudopotential. The CRENBL [116] effective core

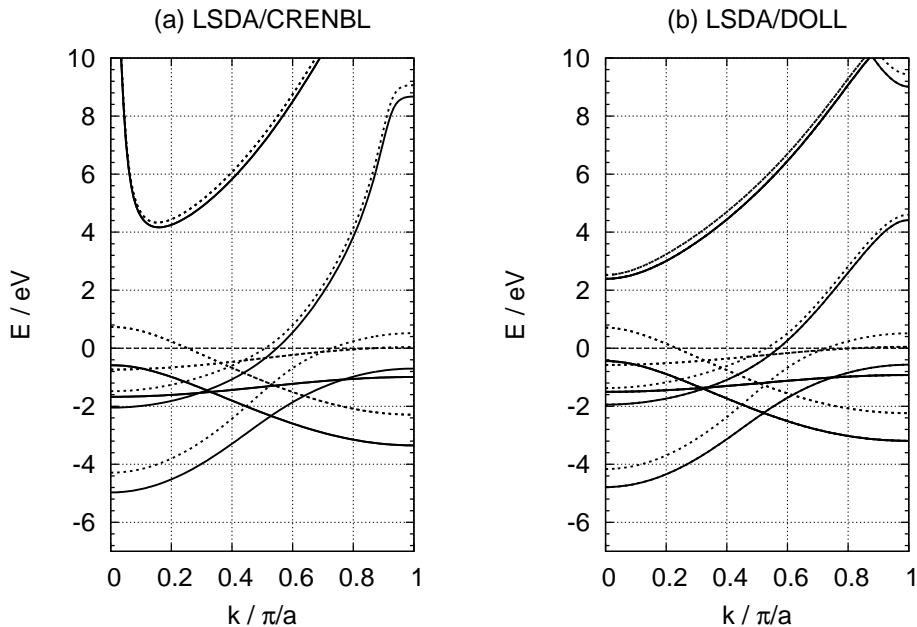


Figure 5.2: Electronic band structure with respect to the Fermi energy (zero line) of monatomic Ni chain at equilibrium lattice spacing $a = 2.9\text{\AA}$ calculated with LSDA functional and CRENBL (a) and DOLL (b) basis set, respectively. The full lines are majority-spin bands, while the dotted lines are minority-spin.

pseudopotential (ECP) is a small core ECP, describing the 10 innermost electrons only. The basis set describes the remaining 18 outer electrons of Ni, and is of very high quality. The optimum lattice constant of 2.09\AA is in agreement with that obtained by Wierzbowska *et al.* [117], and is significantly higher than the nearest-neighbor distance between bulk atoms of 2.5\AA .

Fig. 5.2 shows the electronic band-structure of the ferromagnetic (FM) Ni chain at equilibrium lattice spacing $a = 2.09\text{\AA}$ calculated with the CRENBL ECP basis-set, and an all-electron basis-set (DOLL) optimized for Ni bulk [115]. The results for the two basis-sets are very similar below the Fermi level and above near the Fermi energy. Only for energies well above the Fermi level deviate the band structures appreciably from each other.

The fact that the band structure of the ECP basis-set CRENBL agrees well with the all-electron basis-set DOLL below the Fermi energy indicates that the the core electrons are very well approximated by the ECP. The reason for the deviation of the band-structures for the two basis-sets at higher energies is that the CRENBL basis-set is far larger than the DOLL basis-set and thus provides a better description of the outer electrons. Since we are above all interested in transport properties which are determined by the electrons near the Fermi energy, the deviation of the ban structures well above the Fermi energy is not important here.

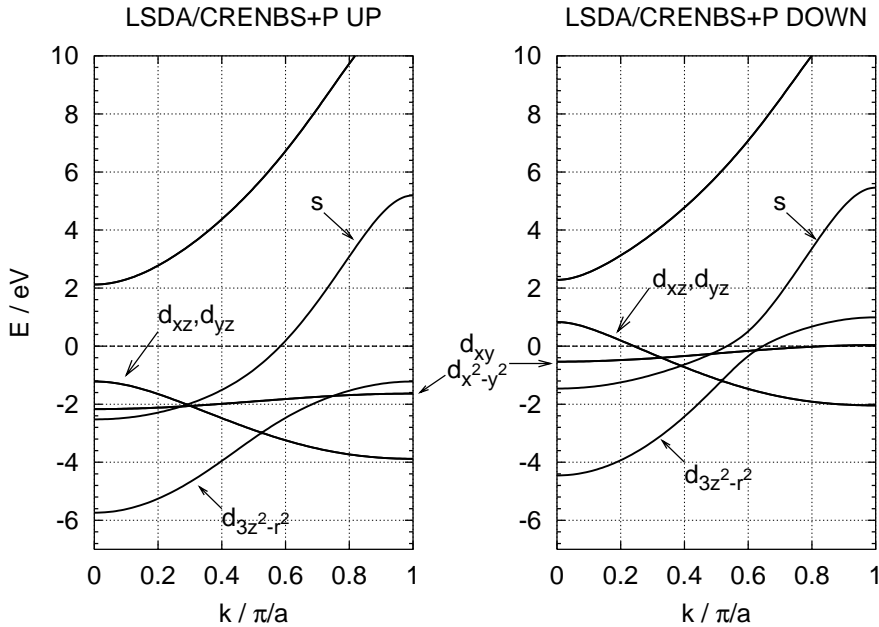


Figure 5.3: Electronic band structure with respect to the Fermi energy (zero line) of monatomic Ni-chain calculated with LSDA functional and CRENBS+P basis set. The left panel shows the majority-spin and the right panel the minority-spin bands.

In a perfect chain no elastic scattering occurs so that all available transport channels at some energy transmit perfectly, i.e. have a transmission of 1. The number of channels available is given by the number of bands at some energy, so the zero-bias conductance is given by the number of bands crossing the Fermi level. Thus in the case of the perfect Ni chain there are one majority-spin channel and six minority-spin channels (two of the bands are doubly-degenerate, see below) contributing to the conductance.

The majority-spin and minority-spin bands are split in energy by up to $\approx 1\text{eV}$ for some bands, and the magnetic moment per atom of the Ni chain is $\approx 1.1\mu_B$ for both basis sets and thus almost twice as high as the magnetic moment of Ni bulk which reflects the low coordination of the chain-atoms compared to the bulk atoms: Due to the lower coordination of the chain atoms, the bands become narrower than in the bulk so that the cost in kinetic energy to pay for the polarization of the bands becomes smaller. This is partially counteracted by the decrease in nearest-neighbor distance with respect to the bulk which leads to a broadening of the bands.

Next, we analyze the orbital nature of the different bands of the Ni chain. Fig. 5.3 shows the band structure of the Ni-chain separately for the two realizations of the spin quantum number. In this case the result was obtained with the CRENBS[116] minimal basis set with large core (the 18 inmost electrons) ECP. Because of the smaller basis-set compared to CRENBL or DOLL and the larger core ECP results obtained with this basis are in general less accurate. However, as Fig. 5.3 shows, the changes in the band structure

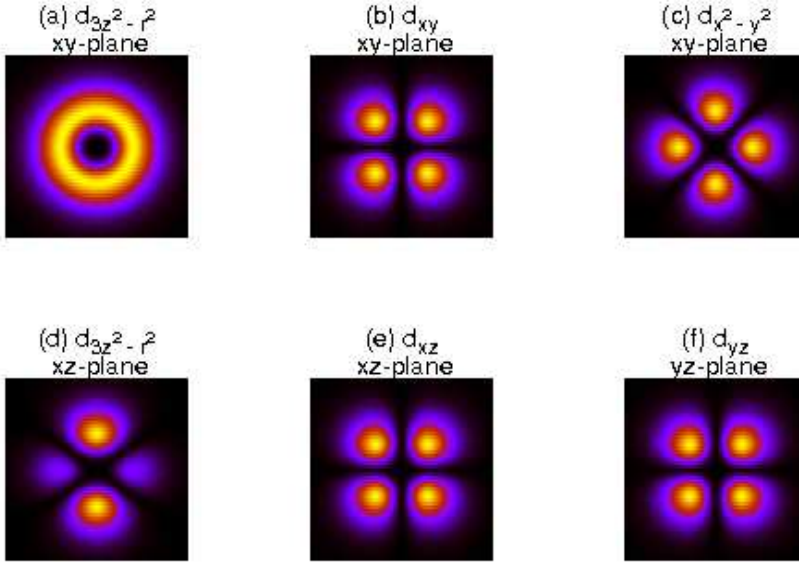


Figure 5.4: Sections of the modulus of the (Cartesian) d -orbitals. The $d_{3z^2-r^2}$ -orbital (a,d) has rotational symmetry around the z -axis (vertical symmetry axis in (d)) and is directed along that axis. All other d -orbitals (b,c,e,f) are shown in their respective planes of extension. In the direction perpendicular to that plane the extension of these orbitals is very small.

compared to the results obtained with CRENB and DOLL are quite moderate, especially near the Fermi level. The number of bands crossing the Fermi level remains the same (1 spin-up band, 6 spin-down bands) and the bands conserve their overall aspect. Only the spin-splitting of some bands has become stronger now (almost 2eV) their bandwidth changes slightly and the magnetic moment per atom now is μ_B . On the other hand the minimal basis-set facilitates the analysis of the band structure a great deal.

The orbital nature of the different bands is determined by the rotational symmetry of the monatomic chain. The eigenstates of the monatomic chain are therefore simultaneously eigenstates of the z -component (for a chain oriented along the z -axis) of the angular momentum operator \hat{L}_z . The s -orbital and the $d_{3z^2-r^2}$ orbital both have angular momentum zero, $l_z = 0$, so there are two bands with angular momentum zero per spin. As shown in Fig. 5.3 the spin-bands with angular momentum zero are the broadest of the s and d -bands. One is mostly s -type (thus labeled s -band in Fig. 5.3) with a small contribution of $d_{3z^2-r^2}$ while the other is mostly $d_{3z^2-r^2}$ -type (labeled $d_{3z^2-r^2}$ -band) with a small contribution of s . The s -bands are only slightly spin-split while the $d_{3z^2-r^2}$ -bands exhibit quite a big spin-splitting of about 1eV (for CRENB, Fig. 5.3a). The s band is by far the broadest as expected, since s -orbitals give rise to highly delocalized electrons. The orbitals d_{xz} and d_{yz} can be combined to the rotationally symmetric orbitals with

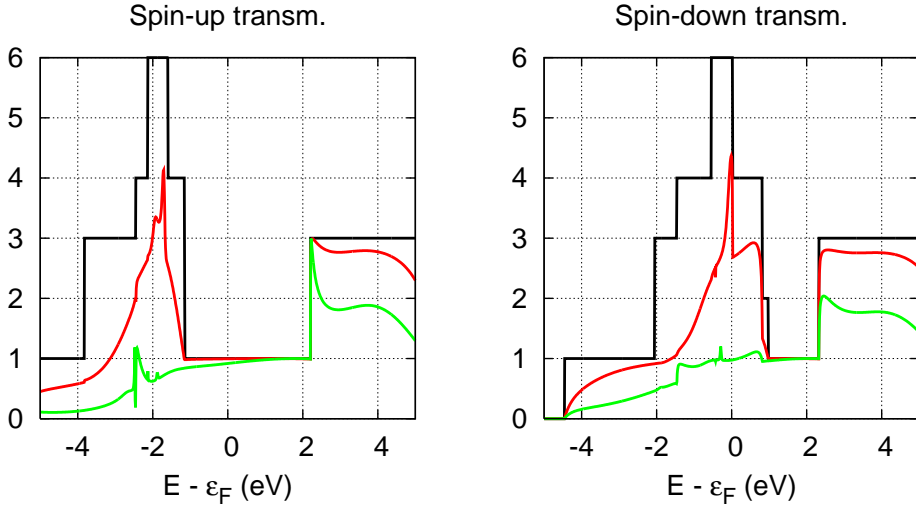


Figure 5.5: Effect of electron scattering in the one-dimensional Ni chain. The length of the gap d between the two semi-infinite Ni chains is larger than the lattice spacing of $a \approx 2.1\text{\AA}$ of the chains and thus gives rise to scattering. The black curves show the spin-resolved transmissions in the case of the perfect chain (no scattering), the red curves in the case of $d = 1.2a = 2.5\text{\AA}$, and the green curves in the case of $d = 1.5a = 3.1\text{\AA}$.

angular momentum ± 1 . Thus two degenerate bands per spin result from the d_{xz} - and d_{yz} -orbitals. These are also spin-split by about 1eV (for CRENLB, Fig. 5.3a) and are a bit narrower than the $d_{3z^2-r^2}$ -bands, since the extension of the d_{xz} - and d_{yz} -orbitals along the z-direction is smaller than that of the $d_{3z^2-r^2}$ -orbital (see graphical representation of d -orbitals in Fig. 5.4) giving rise to a stronger localization of the electrons in these bands. Finally, the two degenerate bands per spin with angular momentum ± 2 are composed of linear combinations of the d_{xy} - and $d_{x^2-y^2}$ -orbitals which are directed perpendicular to the z-axis. This leads to a very small overlap of the orbitals in the z-direction and consequently to very narrow bands giving rise to strong electron localization in these bands. As the other d -bands they are also spin-split by about 1eV.

Finally, we study the effect of electron scattering on the conductance of the Ni chain. Therefore we calculate the transmission of two semi-infinite atomic Ni chains separated by a gap which is larger than the lattice spacing of $a \approx 2.1\text{\AA}$ of the two semi-infinite chains, and compare to the transmission of the perfect chain, Fig. 5.5. We observe that the transmission of the spin-down channel near the Fermi level decreases strongly as we increase the length of the gap d . The spin-up transmission on the other hand is relatively stable near the Fermi level, so that the spin-polarization decreases with increasing length of the gap. This can be understood by the fact that the s -electrons are much less susceptible to scattering than the d -electrons. Therefore the spin-down channel which is composed of s - and d -electrons is much stronger affected by the scattering than the spin-up channel which consists solely of a single s -type channel.

In summary, the d -bands are all spin-split by about 1eV while the s -band is only

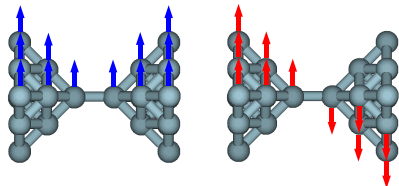


Figure 5.6: Left: Ni nanocontact with parallel (P) magnetization of both electrodes. Right: Ni nanocontact with antiparallel (AP) magnetization of both electrodes.

slightly spin-split due to its hybridization with the $d_{3z^2-r^2}$ -band. The spin-splitting of the d -orbitals gives rise to the filling of the spin-up d -bands while the spin-down d -bands are only partially filled. Thus only the spin-down d -bands and both (spin-degenerate) s -bands contribute to the conduction. Because of the spin-up d -bands being completely filled and the spin-down d -bands being partially filled the d -bands behave like a half-metal and can be modeled by the Stoner model (see Ch. 4). Consequently a sharp domain wall in the monatomic Ni chain would lead to a total blocking of the 5 d -channels, while the s -channels which behave like a paramagnetic metal are not affected by the domain-wall at all. Thus the total transmission of the one-dimensional chain in the AP configuration will be 2, while the transmission in the P configuration is 7. Therefore the MR is given by $(7 - 2)/7 = 5/7 = 71\%$ in def. MR_1 and $5/2 = 250\%$ in def. MR_2 .

These results for the perfect Ni chain have been obtained earlier by Smogunov *et al.* [112, 113] by a full *ab initio* calculation of the magnetization reversal in the chain. This result could explain some early experiments [28], but not recent ones [35]. Furthermore, to date, no evidence of chain formation in Ni has been reported. Even so, scattering at the electrode-chain contact will always be present, and lead to a reduction in the transmissions of the d -channels which are very susceptible to scattering.

5.2 More realistic contact geometries

Now that we have analyzed the perfect one-dimensional case we are prepared to study Ni nanocontacts with more realistic contact geometries. The fact that the electronic structure of the one-dimensional chain near the Fermi level is quite well described employing the CRENBs minimal basis-set with large-core ECP justifies that we restrict our calculations here to that basis.¹ The bulk electrodes will be described by a Bethe lattice (BL) model as described in Ch. 3 which provides a geometry independent description of the electrodes with a Bulk DOS which is smoother than the DOS of the perfect bulk crystal and mimics an average over both disorder realizations and the actual electrode crystal orientations

A reference atomic structure of the contact region has been initially taken like that shown in Fig. 5.6. Following Viret *et al.* [31], we consider the narrowest region to consist of two pyramids facing each other, formed along the (001) direction, and with the two tip Ni atoms 2.6 Å apart forming a dimer. Bulk atomic distances and perfect crystalline order are assumed otherwise. *Ab initio* simulations of the breaking process as the one shown in Fig. 5.8 support this choice. We stress that the section of the nanocontacts varies in the direction of the current flow. This is the situation in real nanocontacts and differs from perfect 1-dimensional systems, studied in Refs. [112, 113], and from bulk systems studied by Van Hoof *et al.* [118]. In this regard, the geometries proposed by

¹We actually performed also calculations with the DOLL and CRENBs basis-set which confirmed that the results do not change essentially.

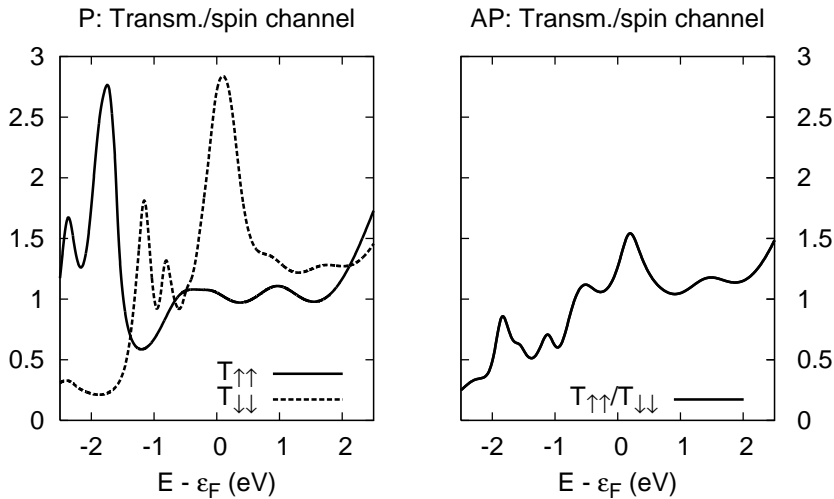


Figure 5.7: Left: Transmission per spin channel of Ni nanocontact for parallel (P) magnetization of both electrodes as shown on left hand side of Fig. 5.6. Right: Same as before but for the Ni nanocontact with antiparallel (AP) magnetization of the two electrodes as shown on right hand side of Fig. 5.6.

Bagrets *et al.* [119] are closer to real nanocontacts, but are not backed up by experiments or simulations.

Figure (5.7) shows the LSDA conductance as a function of energy for both up and down spin channels in two situations: (a) Parallel (P) and (b) antiparallel (AP) bulk magnetic arrangements. In both cases the self-consistent solution has been forced to respect the high symmetry of the nanocontact. In the AP case the self-consistent magnetization reverses abruptly between tip atoms. The resulting magnetic moment for the contact atoms is $\approx 1.0\mu_B$ in both situations. This value is significantly larger than that obtained for bulk or surface atoms ($\approx 0.6\mu_B$) and reflects the low coordination of the tip atoms forming the contact.

The eigenchannel analysis restricted to the contact atoms as explained in the next section reveals that in the P case the majority channel is, for the most part, composed of a single *sp* orbital channel and conducts perfectly around the Fermi energy (set to zero) while the minority channel is composed of three orbital channels (one *s*- and two *d*-like, which conduct roughly the same), and exhibits a transmission strongly dependent on the scattering energy. In the AP case the system is invariant under the combined transformations that exchange L with R and \uparrow with \downarrow , resulting in identical values for the conductance of the two spin channels, which now are composed of a dominant *s* channel and a strongly diminished contribution of the *d* channels. The conductance ratio for this particular case is $x = 2.8/3.65 = 0.77$. This yields $MR_1 = 23\%$ and $MR_2 = 30\%$, which is clearly below large MR claims[28, 35].

Since the minority channel conductance evaluated at the LSDA level exhibits a strong dependence on the scattering energy, we study now whether or not different geometries

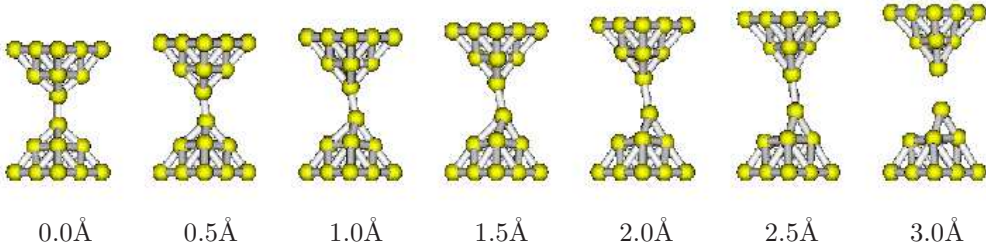


Figure 5.8: Ab-initio simulation of stretching of atomic-size Ni contact. The outer planes ($9+9=18$ atoms) are displaced in steps of 0.5\AA starting from a slightly compressed contact as compared to the ideal contact geometry in Fig. 5.7. The inner atoms of the nanocontact (10 in total) are allowed to relax to local minimum energy in each step of the stretching while the outer planes are kept fixed during the relaxation.

can change the above results qualitatively. In an attempt to explore other realizations of the self-consistent potential compatible with the magnetic boundary conditions and the experimental information, we perform *ab initio* structural relaxations as a function of the displacement between outer planes in the core cluster. To do so, we consider a cluster like that shown in Fig. 5.7. The inner atoms in the cluster (10 in total) are allowed to relax to local minimum energy configurations as we stretch. This results, logically, in lower energy solutions and in the loss of symmetry, so that the transmission in the AP case now becomes slightly spin-dependent.

In Fig. 5.9 the transmission at the Fermi energy per spin channel for the P and the AP configurations are shown as a function of the stretching up to the break-up point, starting from a slightly compressed nanocontact. From this figure we see that the conductance of the minority channel for the P configuration changes significantly upon small changes while the transmission of the majority channel is quite stable against geometrical changes. This behavior reflects the fact that the majority channel is mostly *s*-type, and therefore is quite insensitive to geometrical changes. On the other hand the minority channel has a strong contribution from the *d*-orbitals which are very sensitive to geometrical changes due to their high directionality (see Fig. 5.4). In the AP configuration the transmission of the two spin-channels shows an intermediate behavior between the majority and the minority channel of the P configuration upon stretching of the contact. This can be understood by considering that the two spin-channels are now composed of *s*- and *d*-type orbitals, where the contribution from the *d*-orbitals is weaker than in the minority channel of the P case, but not negligible as for the majority channel in the P configuration. Consequently, the MR, shown in Fig. 5.9, is small and barely changes as the nanocontact is stretched, oscillating between 14% and 23%.

5.3 Orbital eigenchannel analysis

It is often useful to decompose the total conductance into the contributions of the transport eigenchannels, first introduced by Büttiker[63]. These are defined as the linear

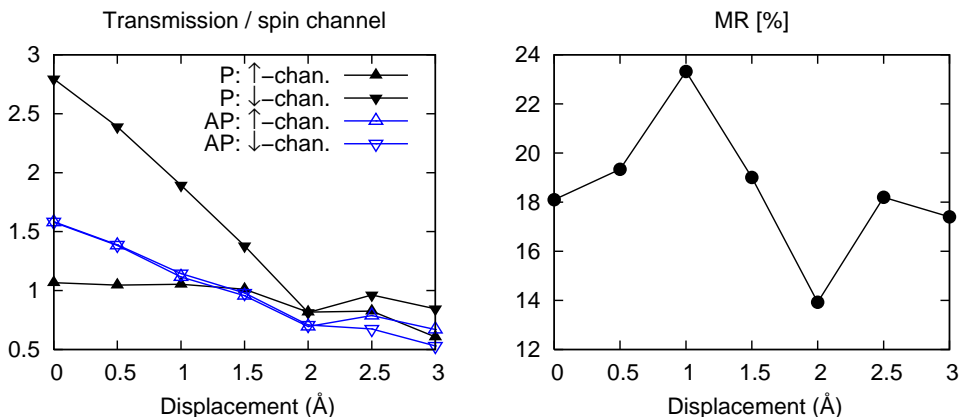


Figure 5.9: LSDA transmission per spin channel at the Fermi energy for P (black) and AP (blue) configuration in dependence of the stretching of the contact (Fig. 5.8).

combinations of the incoming modes in a lead that do not mix upon reflection on the scattering region and present a unique transmission value[45]. The decomposition of the measurable total transmission in terms of the transmissions of these eigenchannels simplifies considerably the interpretation of the results. Knowledge and analysis of the eigenchannel wavefunctions would, in turn, allow one to make predictions regarding the behavior of the conductance upon distortions of the geometry or other perturbations of the scattering region[55]. Unfortunately, in the NEGF approach it is not straightforward to extract the orbital composition of the transport eigenchannels. Only the eigenchannel transmissions can be obtained easily in the NEGF approach from the non-negligible eigenvalues of the transmission matrix. However, the associated eigenvectors turn out to be useless as obtained. The reason is that these eigenvectors contain the contributions to the eigenchannel wavefunctions of the atomic orbitals at one of the borders of the scattering region immediately connected to the leads, but not inside.

In this chapter we present a method for analyzing the orbital contributions to the transport eigenchannels at an arbitrary cross-section of a nanoscopic conductor by calculating the transmission matrix projected onto that cross-section. Our approach generalizes previous work by Cuevas *et al.* [120] for tight-binding-type Hamiltonians to non-orthogonal atomic orbitals basis sets as those commonly used in quantum chemistry packages. An alternative approach to investigate the contributions of certain atomic or molecular orbitals to the conductance consists in directly removing the respective orbitals from the basis set [121].

For the sake of clarity we will repeat here some of the important formulas of the NEGF presented in Ch. 2. Fig. 5.10, shows a sketch of a nano-constriction connecting two bulk leads. We assume that the leads are coupled only to the constriction but not to each

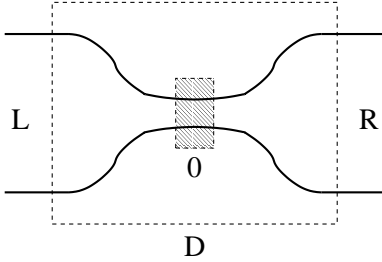


Figure 5.10: Sketch of the scattering problem. L: Left lead. D: device. R: right Lead. 0: cross-section of interest.

other. The Hamiltonian describing this situation is then given by the matrix

$$\mathbf{H} = \begin{pmatrix} \mathbf{H}_L & \mathbf{H}_{LD} & \mathbf{0} \\ \mathbf{H}_{DL} & \mathbf{H}_D & \mathbf{H}_{DR} \\ \mathbf{0} & \mathbf{H}_{RD} & \mathbf{H}_R \end{pmatrix}. \quad (5.1)$$

Since many density functional theory (DFT) codes work in non-orthogonal basis sets, we also allow explicitly for overlap between atomic-orbitals given by the following overlap matrix:

$$\mathbf{S} = \begin{pmatrix} \mathbf{S}_L & \mathbf{S}_{LD} & \mathbf{0} \\ \mathbf{S}_{DL} & \mathbf{S}_D & \mathbf{S}_{DR} \\ \mathbf{0} & \mathbf{S}_{RD} & \mathbf{S}_R \end{pmatrix}. \quad (5.2)$$

The standard approach to calculate the conductance is to calculate the self-energies of the leads from the Green's functions (GF) of the isolated leads, i.e., for the left lead $\mathbf{\Sigma}_L(E) = (\mathbf{H}_{DL} - E\mathbf{S}_{DL})\mathbf{g}_L(E)(\mathbf{H}_{LD} - E\mathbf{S}_{LD})$ where $\mathbf{g}_L(E) = (E\mathbf{S}_L - \mathbf{H}_L)^{-1}$ is the GF of the isolated left lead and analogously for the right lead. From this we can calculate the GF of the device:

$$\mathbf{G}_D(E) = (E\mathbf{S}_D - \mathbf{H}_D - \mathbf{\Sigma}_L(E) - \mathbf{\Sigma}_R(E))^{-1}, \quad (5.3)$$

which, in turn, allows us to calculate the (hermitian) transmission matrix

$$\mathbf{T}(E) = \mathbf{\Gamma}_L(E)^{1/2}\mathbf{G}_D^\dagger(E)\mathbf{\Gamma}_R(E)\mathbf{G}_D(E)\mathbf{\Gamma}_L(E)^{1/2}, \quad (5.4)$$

where $\mathbf{\Gamma}_L = i(\mathbf{\Sigma}_L - \mathbf{\Sigma}_L^\dagger)$ and $\mathbf{\Gamma}_R = i(\mathbf{\Sigma}_R - \mathbf{\Sigma}_R^\dagger)$. Typically the leads are only connected to the left and right borders of the device and are sufficiently far away from the scattering region so that they can be described by a bulk electronic structure. From the structure of eq. (5.4) it follows that only the sub-matrix of \mathbf{T} representing the subspace of the device immediately connected to one of the leads are non-zero. Thus the eigenvectors obtained by diagonalizing \mathbf{T} only contain the atomic orbital contributions to the eigenchannels at one border of the device region but not at the center where the resistance is ultimately determined.

To investigate the orbital nature of the eigenchannels at an arbitrary part of the device we can simply calculate the transmission matrix associated to this part. By choosing this region to be a cross-section, like that indicated in Fig. 5.10, current conservation guarantees that the so-calculated conductance is *approximately* equal to the conductance calculated from the transmission matrix of the whole device. We want to emphasize here that this is really only approximately true for a Hamiltonian beyond the tight-binding approximation since hoppings between atoms on both sides beyond the selected region

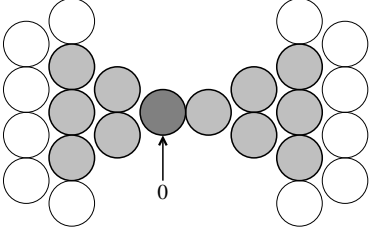


Figure 5.11: Sketch of Ni nanocontact consisting of two pyramids facing each other along the (001) direction with the two tip atoms forming a dimer bridge. The device region (grey circles) consists of 28 Ni atoms and the left and right electrodes (empty circles) are modeled by BLs with appropriate tight-binding parameters to reproduce Ni Bulk DOS.

are neglected. Of course this approximation becomes better the thicker the chosen cross-section is. We proceed by further subdividing the device region. The cross-section of interest will be referred to as 0 while the regions on either side will be denoted as l and r, respectively:

$$\mathbf{H}_D = \begin{pmatrix} \mathbf{h}_l & \mathbf{h}_{l0} & \mathbf{h}_{lr} \\ \mathbf{h}_{0l} & \mathbf{h}_0 & \mathbf{h}_{0r} \\ \mathbf{h}_{rl} & \mathbf{h}_{r0} & \mathbf{h}_r \end{pmatrix} \quad \mathbf{S}_D = \begin{pmatrix} \mathbf{s}_l & \mathbf{s}_{l0} & \mathbf{s}_{lr} \\ \mathbf{s}_{0l} & \mathbf{s}_0 & \mathbf{s}_{0r} \\ \mathbf{s}_{rl} & \mathbf{s}_{r0} & \mathbf{s}_r \end{pmatrix} \quad (5.5)$$

As mentioned above we will neglect the hoppings (and overlaps) between the left and right layers outside the region of interest so we set $\mathbf{h}_{lr} = \mathbf{h}_{rl} = \mathbf{s}_{lr} = \mathbf{s}_{rl} = 0$. With this approximation the GF matrix of the cross-section 0 can be written as

$$\mathbf{G}_0(E) = (E\mathbf{s}_0 - \mathbf{h}_0 - \Sigma'_l(E) - \Sigma'_r(E))^{-1}. \quad (5.6)$$

The self-energy matrices representing the coupling to the left and right lead, $\Sigma'_l(E) = (\mathbf{h}_{0l} - E\mathbf{s}_{0l})\mathbf{g}_l(E)(\mathbf{h}_{l0} - E\mathbf{s}_{l0})$ and $\Sigma'_r(E) = (\mathbf{h}_{0r} - E\mathbf{s}_{0r})\mathbf{g}_r(E)(\mathbf{h}_{r0} - E\mathbf{s}_{r0})$, are given by the GF of the left layer l connected only to the left lead L and the right layer r connected only to the right lead R, respectively:

$$\mathbf{g}_l(E) = (E\mathbf{s}_l - \mathbf{h}_l - \Sigma_L(E))^{-1} \quad (5.7)$$

$$\mathbf{g}_r(E) = (E\mathbf{s}_r - \mathbf{h}_r - \Sigma_R(E))^{-1}. \quad (5.8)$$

The *reduced transmission matrix* (RTM) with respect to the chosen cross-section is now given by

$$\mathbf{T}'(E) = \Gamma'_l(E)^{1/2} \mathbf{G}_0^\dagger(E) \Gamma'_r(E) \mathbf{G}_0(E) \Gamma'_l(E)^{1/2} \quad (5.9)$$

with $\Gamma'_l = i(\Sigma'_l - \Sigma_l^\dagger)$ and $\Gamma'_r = i(\Sigma'_r - \Sigma_r^\dagger)$. Diagonalizing $\mathbf{T}'(E)$ now yields the contribution of the atomic orbitals within the cross-section 0 to the eigenchannels.

In the following we apply the above described method to analyze the orbital nature of the conducting channels of Ni nanocontacts which have recently attracted a lot of interest because of their apparently high magneto-resistive properties [28, 31]. We consider the nanocontact to consist of two ideal pyramids facing each other along the (001) direction and with the two tip atoms being 2.6 Å apart. Bulk atomic distances (2.49 Å) and perfect crystalline order are assumed for each pyramid. Just as in our previous work on Ni nanocontacts[55] we perform *ab initio* quantum transport calculations for this idealized geometry. To this end we use our code ALACANT (ALicante Ab initio Computation Applied to Nano Transport). The electronic structure is computed on the LSDA level

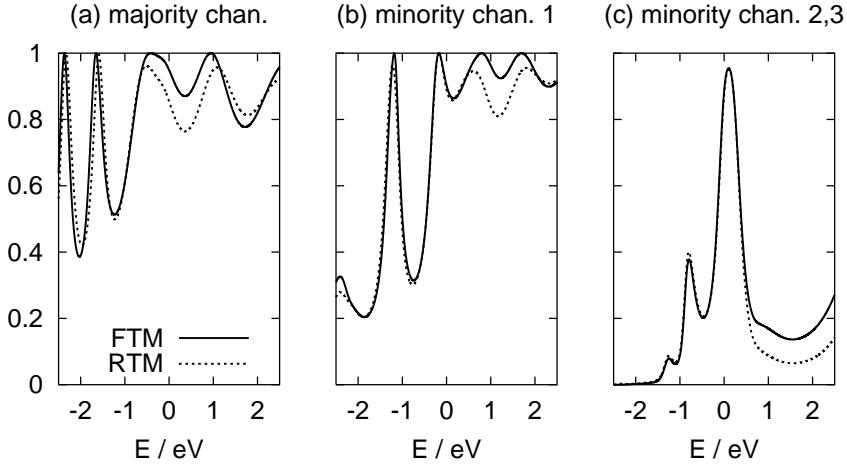


Figure 5.12: Transmission functions of open transport channels for the Ni nanocontact sketched in Fig. 5.11 as calculated from the FTM $\mathbf{T}(E)$ (solid line) and from the RTM $\mathbf{T}'(E)$ (dashed lines). (a) shows the only contributing M channel and (b)-(c) the three m channels. See text for further discussion.

AO	majority	minority 1	minority 2	minority 3
s	97%	62%	0	0
p_x	0	0	28%	0
p_y	0	0	0	28%
p_z	3%	23%	0	0
$d_{3z^2-r^2}$	0	15%	0	0
d_{xz}	0	0	72%	0
d_{yz}	0	0	0	72%
$d_{x^2-y^2}$	0	0	0	0
d_{xy}	0	0	0	0

Table 5.1: Eigenvectors of the RTM at the Fermi level for the contact sketched in Fig. 5.11. Each column gives the weights of the atomic orbitals (AO) given in the left column on the tip atom in each eigenchannel shown in Fig. 5.12.

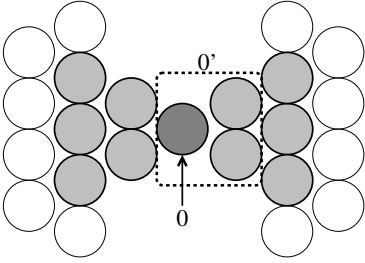


Figure 5.13: Sketch of Ni nanocontact (27 atoms). As in Fig. 5.11 the contact consists of two pyramids along the (001) direction but now both pyramids share the same atom at the tip. The device region (grey circles) consists of 27 Ni atoms and the left and right electrodes (empty circles) are modeled by BLs with appropriate tight-binding parameters to reproduce Ni bulk DOS.

of DFT with a minimal basis set and the electrodes are described by means of a semi-empirical tight-binding BL model.

As indicated in Fig. 5.11 we calculate the RTM $\mathbf{T}'(E)$ for one of the tip atoms of the contact (labeled with 0) and diagonalize it to obtain the eigenchannels and the corresponding transmissions projected on the tip atom. In Fig. 5.12 we compare the individual channel transmissions calculated on the one hand from the full transmission matrix (FTM) $\mathbf{T}(E)$ and on the other hand from the RTM $\mathbf{T}'(E)$. Though the electron hopping between regions l and r of the contact has been neglected in calculating the RTM the so calculated channel transmissions approximate very well those calculated using the FTM so that it is very easy to relate the RTM channel transmissions with the FTM channel transmission. This shows that the hopping between the regions l and r on both sides of the tip atom is almost negligible. Only for the one majority (M) channel we see a small deviation near the Fermi energy indicating that here 2nd neighbor hopping contributes to the transmission of that channel. As the eigenvectors of the RTM (see Table 5.1) reveal, this channel is mainly s-type. Since s-electrons are strongly delocalized there is a small but finite contribution from second-neighbor hopping explaining the deviation between the FTM and RTM transmission in that channel. The first minority (m) channel is also mainly s-type but now it is hybridized with $d_{3z^2-r^2}$ and p_z orbitals. The other two m channels are degenerate and mainly d_{xz} - and d_{yz} -type strongly hybridized with p_x - and p_y -orbitals, respectively.

As discussed in our previous work[55] the five d-type transport channels for the m electrons available in the perfect Ni chain[112] are easily blocked in a contact with a realistic geometry like that in Fig. 5.11 because the d-orbitals are very sensitive to geometry. We have referred to this as *orbital blocking*. It is not so surprising that the $d_{x^2-y^2}$ - and d_{xy} -channel which are very flat bands just touching the Fermi level in the perfect chain are easily blocked in a realistic contact geometry. These bands represent strongly localized electrons which are easily scattered in geometries with low symmetry. Interestingly, even the $d_{3z^2-r^2}$ -channel, which for the perfect chain is a very broad band crossing the Fermi level at half band width, does not contribute to the conduction as our eigenchannel analysis shows. This channel is blocked because the $d_{3z^2-r^2}$ -orbital lying along the symmetry axis of the contact is not “compatible” with the geometry of the two pyramids. On the other hand the d_{xz} - and d_{yz} -channels are both open in that geometry because their shape is compatible with the pyramid geometry of the contacts. This illustrates how the geometry of a contact can effectively block (or open) channels composed of very directional orbitals. Of course, for different geometries we can expect different channels to be blocked or opened.

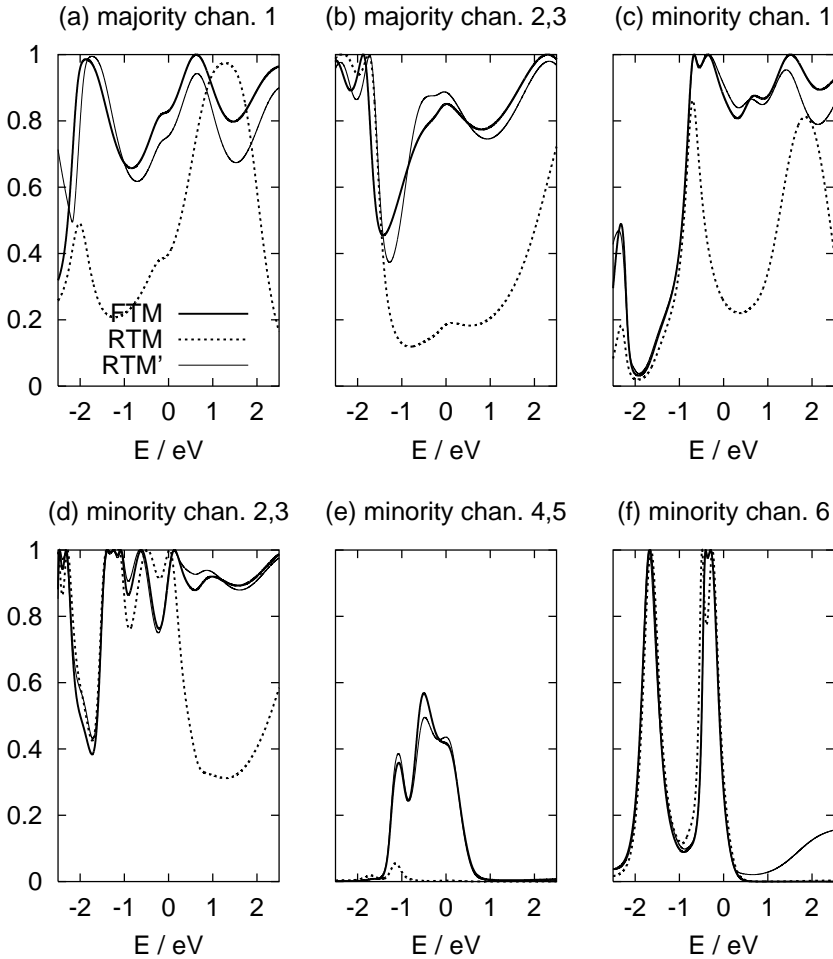


Figure 5.14: Transmission functions of open transport channels for the Ni nanocontact sketched in Fig. 5.3 as calculated from the FTM $\mathbf{T}(E)$ (solid lines) and from the RTM $\mathbf{T}'(E)$ (dashed lines). The RTM transmissions calculated for the cross-section labeled with $0'$ in Fig. 5.3 are given by the thin solid curves (labeled RTM').

Obviously, the approximation made in the calculation of the RTM becomes worse the bigger the hopping between the regions l and r is. For example, in the contact geometry shown in Fig. 5.3 electron hopping from the layers immediately connected to the central atom (labeled 0) is certainly bigger than in the geometry of Fig. 5.11. Indeed, Fig. 5.14 shows that for almost all channels the RTM transmissions differ appreciably from FTM transmissions, making it difficult in some cases to relate them to each other. Fortunately, we can judge by exclusion which RTM transmission relates to which FTM transmission since for the other channels at least the RTM transmission function mimics the overall behavior of the FTM transmission function. However, for more complicated situations it might be impossible to match the RTM transmission with the FTM transmission for all channels. The cure to this problem is obvious: One has to choose a bigger cross-section, i.e., add an atomic layer to the cross-section so that the hopping between l and r becomes small again. If we choose, e.g., the cross-section labeled with 0' in Fig. 5.3 (including the atomic layer to the right of the central atom) the so calculated RTM transmissions now approximate very well the FTM transmissions as can be seen in Fig. 5.14.

In summary, we have shown how to obtain the orbital contributions to the eigenchannels at an arbitrary cross-section of a nanoscopic conductor. The method has been implemented into our *ab initio* quantum transport program ALACANT and we have illustrated the method by exploring the orbital nature of the eigenchannels of a Ni nanocontact. The method works very well when the chosen cross-section is thick enough so that hopping from the layers left and right to the cross-section becomes negligible. Hence in some cases an additional atomic layer has to be included to the cross-section we are actually interested in. Taking this into account the method has no limitations and can be readily applied to *ab initio* transport calculations in all types of nanocontacts [59] and molecular junctions.

5.4 The self-interaction problem

LDA provides a commonly accepted description of the electronic structure of bulk and surface ferromagnetism in transition metals. However, the low coordination of the atoms in nanocontacts might give rise to a further localization of the *d*-electrons (compared with bulk). But as discussed in Ch. 3, LDA fails to describe localized electrons properly due to the spurious self-interaction. And although GGA improves somewhat on LDA with regard to the self-interaction problem by taking into account derivatives of the electron density, this is still not sufficient for materials with strongly localized *d*-electrons like e.g. the transition metal oxides. As explained at the end of Sec. 3.1 an alternative approach to the electronic structure comes from the use of a hybrid functionals which reintroduce some Hartree-Fock exchange (HFX) in order to correct the spurious self-interaction. B3LYP for example combines HFX with a certain GGA exchange functional [81], and happens to give a reasonable description of the electronic structure and local magnetic moments in NiO [82] and La₂CuO₄ [122]. Popular alternatives to using hybrid functionals are e.g. LDA+U [83] and SIC [123].

Here, we explore how the use of different functionals which improve on LDA with regard to the spurious self-interaction affects the transport properties of Ni nanocontacts. We start by considering again the perfect monatomic Ni chain. Fig. 5.15 shows the transmission functions of both spin-channels for different density functionals. We note that the transmission of the perfect chain barely changes when using a GGA functional

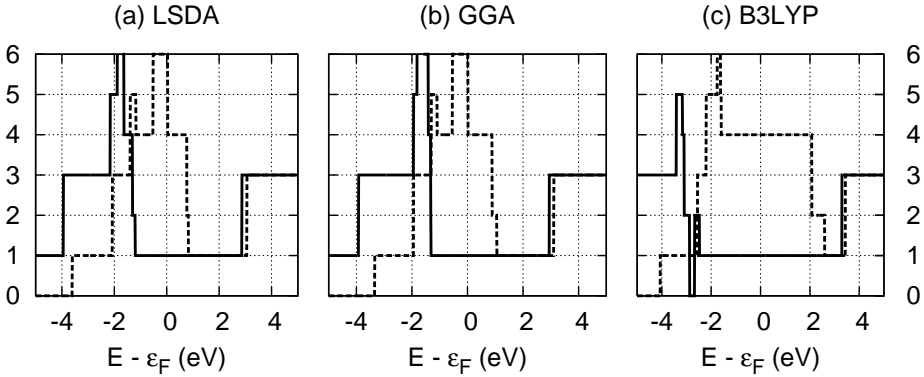


Figure 5.15: Spin resolved transmission function of perfect Ni chain for different functionals: (a) LSDA, (b) GGA, (c) hybrid functional with 10% of HFX and (d) hybrid functional with 20% of HFX. Solid lines are majority-spin and dashed lines minority-spin transmissions.

(b) instead of the LSDA functional (a). Only when introducing HFX by using the B3LYP hybrid functional does the transmission change appreciably. With B3LYP, the number of conduction channels is reduced to 1 majority + 4 minority spin-channels at the Fermi level compared to the LSDA results. This agrees with recent LSDA+U calculations reported by Wierzbowska *et al.* [117] where the two degenerate flat minority bands $d_{xy}, d_{x^2-y^2}$ are shifted downwards in energy because of the exchange interaction canceling part of the self-interaction of the strongly localized electrons in these flat bands.

As can be from Fig. 5.16(a) computing the conductance of the Ni nanocontact shown in Fig. 5.6 with a GGA functional, again the result does not change very much with respect to the LSDA result (compare with Fig. 5.6). However, we should note that when using GGA more elaborate basis sets than the minimal basis set employed in the previous calculations on the LSDA level are required in order to recover the LSDA result. If the same minimal basis set as in the LSDA calculations is used with the GGA functional the conductance of the d -type minority-channel is considerably reduced. This seems to have to do with the fact that due to its dependence on the gradient of the electron density the GGA functional is more sensitive to the geometry than the LSDA functional and more complete basis sets are required to get reliable results. With B3LYP the results for the conductance (see Fig. 5.16(b)) are remarkably different in regard to the minority channel conductance which is strongly reduced at the Fermi level. The minority d -channels are most strongly affected by this reduction of the transmission. Why the minority-spin channel transmission is so strongly suppressed when using the B3LYP functional in the case of the nanocontact but not in the case of the perfect infinite chain might have to do with the d -electrons of the tip atoms becoming very localized so that they are more strongly affected by the HFX, but further investigation of this issue is needed. However, by comparison with the Ni conductance histogram [34] one can see that the results obtained with LSDA and GGA are in very good agreement with the first peak in the histogram at $\sim 2.4 - 3.0e^2/h$ while the B3LYP value is not. So LSDA and GGA

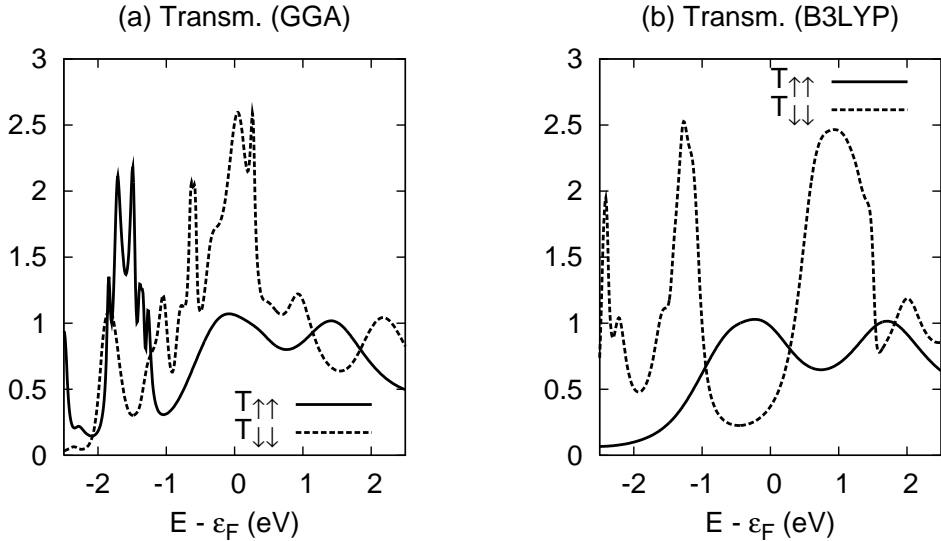


Figure 5.16: (a) Transmission per spin channel calculated with GGA density functional in the P configuration for the model nanocontact shown in Fig. 5.6. (b) same as (a) but calculated with B3LYP hybrid functional.

functionals might be more appropriate for describing purely metallic nanocontacts than B3LYP. However, this might be different when oxygen adsorbates are present in the contact region, as will be discussed in the next Chapter. Clearly, LSDA and GGA are not appropriate for describing the conduction through a molecule contacted by atomic tips as they do not reproduce well the energy levels of molecules. On the other hand B3LYP does reproduce molecular energy levels extremely well. So the question of the appropriate functional to use in DFT based transport calculations is an open one, and it seems that depending on the application one has to employ different functionals and justify their use by comparison with experiments. This however limits severely the predictive power of DFT based transport calculations. A systematic improvement of the DFT based transport calculations can only be achieved by employing many-body techniques on top of the DFT calculations like the GW perturbation theory or DMFT as explained in Sec. 3.3.

5.5 Discussion of results

As a rule of thumb, the maximum number of conduction channels in atomic-size contacts is roughly determined by the number of valence electrons of the contact atom(s) [124]. However, as shown above, this hypothetical upper limit is never reached in Ni nanocontacts since the transmission of the minority-spin channel being composed of *s*- and *d*-orbitals is strongly reduced by scattering due the contact geometry. This result is impossible to predict without a full atomistic self-consistent calculation. The majority channel is *s*-type. Thus, this channel transmits almost perfectly and evolves smoothly

with the stretching of the contact giving a stable contribution of $T_{\uparrow\uparrow} \approx 1$ (see Fig. 5.9). The s -orbitals in the minority channel are strongly hybridized with d -orbitals and, therefore, are more sensitive to the contact geometry. The contribution to the conductance of the latter, which form narrower bands, disappears with the stretching and disorder, as expected (see Fig. 5.9). On the other hand, in the AP configuration mostly one s -orbital channel per spin contributes. In the AP case the conductance *per spin channel* lies thus in the vicinity of e^2/h , giving $\approx 2e^2/h$ in total and is fairly stable during the last stage of the breaking of the nanocontact.

Comparing the nature of the eigenchannels contributing to the transmission of the nanocontact in the P case with the orbital nature of the bands of the one-dimensional chain helps to understand why 3 of the d -channels are blocked in the contact which transmit perfectly in the one-dimensional case. An eigenchannel analysis restricted to the tip atom (see Sec. 5.3) for the symmetric cluster (Fig. 5.7) reveals that in the P case the only majority channel contributing to the conductance is s -type, while of the 3 minority channels contributing appreciably to the conductance, one is s -type (with a small contribution of the $d_{3z^2-r^2}$ -orbital), one is d_{xz} and one is d_{yz} -type. The three other minority channels that contribute in the perfect chain, namely the doubly-degenerate $d_{xy}, d_{x^2-y^2}$ -channel and the $d_{3z^2-r^2}$ -channel do not contribute to the conductance. It is worth noting that these channels have not “vanished” at the Fermi level, as can be seen from the local DOS (not shown), only their transmission has become practically zero. The reason for this lies in the geometry of the d -orbitals. As is already clear from the discussion of the perfect chain, the d_{xy} - and $d_{x^2-y^2}$ -orbitals have very small overlap in the direction of the z -axis which is the main axis of the contact and of the chain. Therefore the electrons in this channel are very localized (flat band in the perfect chain) and thus very easily scattered by the geometry. On the other hand, it is a bit surprising at first glance, that the $d_{3z^2-r^2}$ -channel which is the second-broadest band (and thus the electrons in that band are almost as delocalized as the s -electrons) in the perfect chain does not contribute either to the conductance in the nanocontact. However, in the pyramid-geometry this orbital which is directed along the z -direction (Fig. 5.4a,d) does not connect well to the orbitals in the pyramid and thus is geometrically blocked for transmission. On the other hand the minority bands of d_{xz} - and d_{yz} -type contribute appreciably to the conductance of the nanocontact since these orbitals connect well to the corresponding orbitals in the pyramids. Only by distorting the nanocontact upon stretching the geometrical matching is destroyed quite rapidly, leading to a rapid decrease in the conductance of the minority channel. The reason behind the very small MR values is thus the orbital (or geometric) blocking of most of the *a priori* available minority channels in the P configuration due to the non-ideal geometry of the nanocontacts.

The results presented in this chapter have been confirmed by recent experiments on Ni nanocontacts under very controlled conditions [37, 38], and also by recent theoretical work employing slightly different methodologies [125, 54, 126]. Moreover, the total conductance of $\approx 2.5 - 3.5e^2/h$ for the single-atom nanocontact agrees fairly well with the broad peak in the Ni conductance histogram [34]. So what else could be the reason behind the huge MR values observed in some experiments when ballistic domain wall scattering can be excluded? First, as will be shown in the next chapter, the BMR effect can be enhanced considerably (by more than one order of magnitude) due to the presence of oxygen surface adsorbates in the contact region [56]. Indeed, just the experiments that obtain huge MR values have not been performed in ultra-high vacuum conditions in

5 *Ni nanocontacts*

contrast to the more recent ones that do not obtain high MR [34, 37, 38]. But this cannot explain the highest MR results obtained [32, 33, 35] which are several orders of magnitude higher. Another likely explanation for very high MR values are magnetostriction and magnetostatic effects which lead to a distortion of the contact geometry in dependence of the relative magnetization of the two sections [36, 127].

6 NiO chains in Ni nanocontacts

In going from bulk to lower dimensions material properties often change drastically. A recent example is that of interfaces between different insulators which can become metallic [128, 129]. Even more recently, it has been predicted theoretically that certain oxygen surfaces of some insulating ceramic oxides can exhibit magnetism and half-metallicity [130]. The ultimate limit in this respect can be found in atomic chains formed in metallic nanocontacts which allow to study the transport properties of one-dimensional systems of atomic size [131]. Due to the lower coordination of the atoms the properties of metallic atomic chains formed in nanocontacts can be remarkably different from those in the bulk.

However, not all metals form atomic chains in nanocontacts, although recently, it has been found that the presence of oxygen favours their formation [132]. For example, experiments with Ni nanocontacts [28, 35, 31, 34, 38, 37] have never shown evidence of chain formation. Nevertheless, the presence of oxygen in the contact region could possibly lead to the formation of NiO chains. In this context it has also been proposed that the rather moderate magnetoresistive properties of pure Ni nanocontacts [55, 133, 125, 54] could be enhanced considerably by the presence of oxygen adsorbates on the surface of the Ni electrodes [134]. On the other hand, bulk NiO is a common example of a correlated insulator with antiferromagnetic (AF) order (see e.g., Ref. [135, 82]), which remains insulating even above the Néel temperature when the AF order is lost. Thus it is not at all obvious whether or not oxidized Ni nanocontacts or NiO chains should be conductors.

In this chapter we investigate the electronic and magnetic structure and the transport properties of one-dimensional NiO chains, both idealized infinite ones and more realistic short ones suspended between Ni nanocontacts. Anticipating our most important results our *ab initio* quantum transport calculations show that short NiO chains suspended between Ni nanocontacts can become half-metallic conductors, i.e., carry an almost 100% spin-polarized current. This result holds true even for a single O atom in between Ni electrodes. Consequently, for antiparallel alignment of the electrode magnetizations the transport through the contact is strongly suppressed resulting in very large MR [difference in resistance between antiparallel and parallel alignment of the magnetizations of the electrodes normalized either to the higher resistance value (MR_1) or to the lower one (MR_2): $MR_1 \approx 90\%$ and $MR_2 \approx 700\%$, respectively].

6.1 Electronic and magnetic properties of bulk NiO

Bulk nickel monoxide (NiO) is an example of a strongly correlated material with insulating character and antiferromagnetic (AF) order, which has been studied extensively in the past, both experimentally and theoretically (see e.g. [136, 135, 137, 80, 84, 138, 139, 140, 141, 82] and Refs. therein). It is now understood that the measured optical gap of $\sim 4\text{eV}$ is due to charge-transfer excitations from the O $2p$ band (which overlaps with the filled Ni $3d$ band) to the unfilled Ni $3d$ band [135]. Thus it is not a pure Mott-Hubbard insulator where the gap is solely determined by excitations from filled to unfilled Ni $3d$

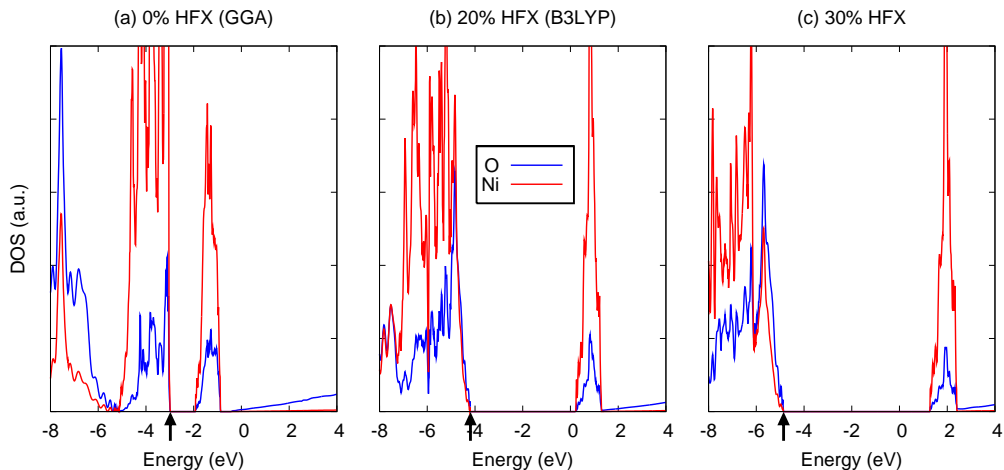


Figure 6.1: DOS of bulk NiO projected onto O atomic orbitals (red lines) and Ni atomic orbitals (green lines) for different density functionals. (a) GGA functional, (b) B3LYP hybrid functional with 20% HFX, and (c) hybrid functional with 30% HFX. The black arrow marks the top of the valence band in each panel. For the calculations the CRYSTAL *ab initio* package has been employed [98]. See text and Ref. [82] for further discussions.

bands. Though the AF coupling in bulk NiO is strong, it is found experimentally that the magnetic order seems not to affect the electronic structure significantly. Even above the Néel temperature when the magnetic order is lost, bulk NiO remains an insulator and preserves the charge-transfer character and the magnitude of the gap [140].

Due to the strong electron correlations of the Ni $3d$ -electrons, NiO presents a challenge for *ab initio* electronic structure calculations. In fact, the standard approximations of DFT —LDA and GGA— do not give a satisfying description of the electronic structure of bulk NiO. Because of the insufficient cancellation of the self-interaction in the local exchange functional of the LDA, the occupied narrow $3d$ -bands are raised in energy. As a result LDA severely underestimates the gap of bulk NiO [80]. The GGA exchange functional improves somewhat the description of NiO but the energy gap is still too small and also the charge-transfer character is not captured correctly [80], as can be seen from Fig. 6.1(a).

As explained in Ch. 3, the self-interaction error inherent in LDA and GGA can be corrected by using hybrid functionals like e.g. the B3LYP functional [81] which happens to give a reasonable description of the electronic and magnetic structure of bulk Ni [82]. As we can see from Fig. 6.1(b), the B3LYP functional which mixes 20% of HFX to the GGA exchange functional gives just the right magnitude of the gap of ~ 4 eV. Also the charge transfer character of the band gap is somewhat improved although there is still a strong contribution of Ni $3d$ -states at the upper band edge of the valence band. Increasing the amount of HFX beyond the 20% of the B3LYP functional the O $2p$ -states become yet more dominant but also the band gap increases to about 6eV which is above the experimental value (Fig. 6.1(c)). With regard to the magnetic structure of NiO,

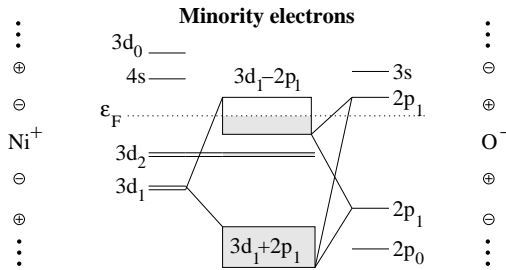


Figure 6.2: Schematic one-electron energies of a one-dimensional NiO chain in z -direction for minority-spin. To the left and right the orbital energies of an individual Ni^+ cation and O^- anion in the crystal field of a one-dimensional Ni^+O^- chain are shown. In the center the formation of valence and conduction bands by hybridization of Ni $3d$ and O $2p$ orbitals is shown.

B3LYP predicts the correct antiferromagnetic (AF) order, but slightly underestimates the magnetic moments and coupling constants. On the other hand a hybrid functional with 30% of HFX gives the correct magnetic moment and coupling constants and also predicts the correct AF order. A more detailed discussion can be found in Ref. [82]. Other approaches for correcting the self-interaction like the LDA+U method the self-interaction-corrected LDA (SIC-LDA), and the GW approximation lead to similar results as those obtained from the hybrid functional approach [83, 139, 82].

For the above electronic structure calculations of bulk NiO we have employed elaborate all-electron basis sets for Ni and O [115, 142] similar to those employed for reported HF and B3LYP calculations of bulk NiO [82], but extended with a diffusive sp -function in the case of Ni and a d -polarization function in the case of O which makes them suitable also for the description of metallic systems in contrast to the original basis set which have been developed for the description of insulating NiO. As can be seen from Fig. 6.1 we reproduce previous GGA and B3LYP results for bulk NiO [82] with these basis sets.

Given the uncertainty with respect to the functional we will employ for the calculation of NiO chains in the following both a GGA functional and the B3LYP functional. We would like to emphasize here that it is not clear from the outset how much HFX is necessary in order to give a reliable description of atomic NiO chains since the electronic structure of the one-dimensional NiO chain is quite different from the one of bulk NiO as we will see in the following.

6.2 One-dimensional NiO

The electronic properties of bulk NiO are, to a large extent, determined by the atomic scale properties, like the crystal field splitting of the Ni and O energy levels and the amount of electron charge transferred from Ni to O. The latter, in turn, is determined by the interplay between Madelung binding energy, the ionization potential of Ni, and the electron affinity of O. Due to the lower coordination and the corresponding decrease in Madelung binding energy the electron transfer from Ni to O is less favourable in an atomic chain than in bulk (where the electron transfer is almost complete resulting in an ionic configuration of $\text{Ni}^{2+}\text{O}^{2-}$). The proper starting point to discuss the formation of energy bands in the one-dimensional NiO chain are therefore the univalent ions Ni^+ and O^- .

In order to understand how the low coordination affects the atomic properties of the

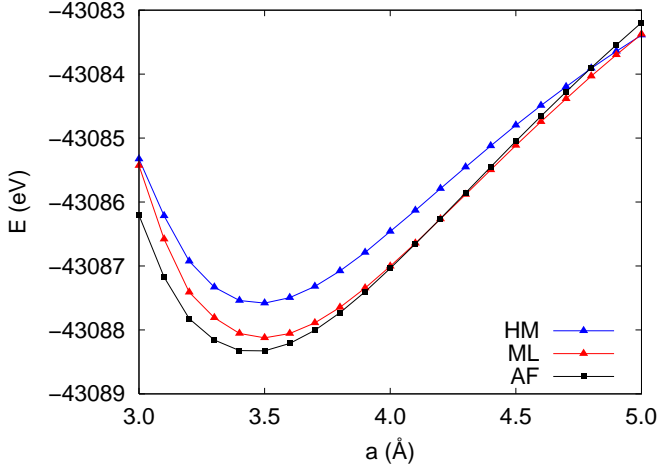


Figure 6.3: Energy per unit cell of infinite NiO chain in dependence of lattice spacing a calculated with B3LYP hybrid functional. Blue triangles indicate the half-metallic state (HM), red triangles the molecule-like insulating state with FM order (ML), and black boxes the insulating state with AF order (AF).

constituting ions we have first performed B3LYP calculations of both a single Ni^+ ion and a single O^- ion each in the field of point charges that mimic the crystal field of a one-dimensional chain of univalent Ni and O ions. We find that for both ions the spin-doublet state ($S = 1/2$) minimizes the energy as is the case for the free ions. In Fig. 6.2 we show schematically the energy levels of Ni^+ and O^- in the presence of the point charges for minority spin only. Interestingly, for minority spins, the occupied Ni $3d_1$ orbitals (d_{xz} and d_{yz}) of the Ni^+ ion fall energetically in between the occupied and unoccupied O $2p_1$ orbital (p_x and p_y) of the O^- ion. Thus the $3d_1$ and $2p_1$ orbitals can form two filled degenerate bonding bands and two degenerate partially filled antibonding bands as indicated in the middle part of Fig. 6.2. The $3d_2$ (d_{xy} and $d_{x^2-y^2}$) doublet is somewhat above in energy to the $3d_1$ but cannot hybridize with the oxygen $2p$ orbitals. The Ni $3d_0$ ($d_{3z^2-r^2}$) and $4s$ are empty while the O $2p_0$ (p_z) and $2s$ orbitals are filled and much lower in energy so that no hybridization takes place though symmetry would allow for it.

On the other hand, for majority-spin electrons (not shown) all five Ni $3d$ orbitals are filled while the $4s$ is also empty, i.e., the Ni^+ valence configuration is $3d^9$ and not $4s^1 3d^8$ as for the free Ni^+ ion. Moreover, all of the O $2p$ orbitals are filled so that the Ni^+ and O^- ions can only form either completely filled or completely empty bands for the majority spin. Thus the ionic picture suggests that a one-dimensional NiO chain should become a half-metallic conductor where only the minority-spin levels form conducting bands.

Not surprisingly, our calculations for infinite one-dimensional NiO chains (Fig. 6.2) show that a univalent ionic configuration as an initial guess results in a half-metallic state for large separation of the individual chain atoms (i.e., large lattice spacing of 5\AA) as suggested by the ionic picture. However, as can be seen from Fig.6.2(a), the half-metallic state is only a metastable state for most values of the lattice spacing. This half-metallic state is “shadowed” by a second state with FM order and insulating character. By successively decreasing the lattice spacing a of the chain and using the (half-metallic) state of the previous step for the initial guess, the half-metallic state can be generated also for smaller inter-atomic distances which points towards its metastability. Around the equilibrium lattice spacing ($a \sim 3.4\text{\AA}$) the ground state of the chain has AF order and is of insulating character with a substantial gap of $\sim 4\text{eV}$ like in bulk. When stretched out

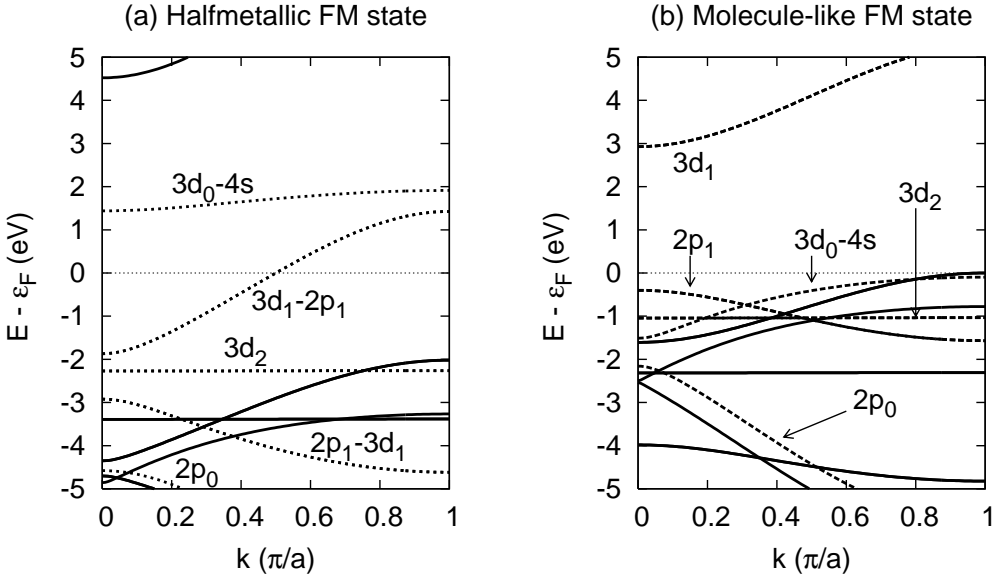


Figure 6.4: (a) B3LYP band structure of HM state for a lattice spacing of 3.6\AA . Solid lines indicate majority-spin bands and dashed lines indicate minority-spin bands. (b) Same as (a) but for ML FM state.

of equilibrium the FM state and the AF state become comparable in energy until finally, at a lattice spacing of $\sim 4.2\text{\AA}$, the FM state becomes the ground state.

The band structure diagram in Fig. 6.4(c) shows that the metastable state with FM order corresponds indeed to the half-metallic state suggested by the ionic picture: The half-filled doubly-degenerate conduction band is formed by minority-spin Ni $3d_1$ orbitals hybridized with O $2p_1$ orbitals while the Ni $3d_2$ orbitals do not hybridize with O $2p$ orbitals and thus form a flat valence band. The lowest-lying empty band is formed by the minority-spin Ni $3d_0$ orbital which is slightly hybridized with the Ni $4s$ orbital. On the other hand the stable state with FM order and insulating character (see band structure in Fig. 6.4(b)) actually corresponds to the ground state of the NiO molecule which is a ${}^3\Sigma^{-1}$ state[143]. The main difference with the half-metallic state is that now the *non-degenerate* Ni $3d_0$ and $4s$ orbitals form a minority-spin valence band while the minority-spin *doubly degenerate half-filled* antibonding band composed of Ni $3d_1$ and O $2p_1$ bands is emptied and a substantial gap of $\sim 3\text{eV}$ opens. Thus the infinite chain behaves like an insulator for reasonable values of the chain stretching.

On the other hand using a GGA functional, the one-dimensional NiO chain is always conducting for FM order in contrast to the previous B3LYP results. In Fig. 6.6, we show the GGA band structure of an ideal one-dimensional NiO chain in the ferromagnetic (FM) phase. Compared to the B3LYP band structure for the half-metallic state at same lattice spacing shown in Fig. 6.4(a) we see that the occupied bands have been raised considerably in energy. In particular, the doubly-degenerate flat minority-spin band of type (d_2)

composed of Ni $3d_{xy}$ and $3d_{x^2-y^2}$ orbitals (well below the Fermi level with B3LYP), now actually crosses the Fermi level. Also the doubly-degenerate and previously half-filled minority-spin band of type (d_1) composed of Ni $3d_{xz}$ and $3d_{yz}$ orbitals hybridized with O $2p_x$ and $2p_y$ orbital (the only conduction band with B3LYP) calculation are raised somewhat in energy. Consequently, the previously empty minority-spin band of type (d_0) composed of Ni $3d_{3z^2-r^2}$ orbitals is lowered in energy with respect to the other filled or partially filled $3d$ bands, and becomes a conduction band.

On the other hand also the majority-spin bands are raised in energy. The doubly-degenerate majority-spin band composed of Ni $3d_{xz}$ and $3d_{yz}$ orbitals hybridized with O $2p_x$ and $2p_y$ orbitals which was well below the Fermi level in the B3LYP calculation now also crosses the Fermi level near to its upper band edge. Thus in GGA the ideal case of the infinite NiO chain in the FM phase does not represent a half-metallic conductor, although the spin-polarization of the conduction bands is quite strong (5 minority-spin bands vs. 2 majority-spin bands).

The change in the electronic structure of the one-dimensional NiO chain on the GGA level with respect to the B3LYP results can be explained by the insufficient cancellation of the self-interaction by the GGA exchange functional, which causes the occupied Ni $3d$ orbitals to artificially rise in energy.

6.3 O-bridge in Ni nanocontacts

Atomic chains formed in break junctions have a finite length and are suspended between electrodes. It is well known that the contact between the atomic chain and the electrode tip will have considerable effect on the electronic structure of the chain, especially when d -orbitals are involved like is the case here[55].

We have thus calculated the electronic structure and transport properties of both a single oxygen atom and a O-Ni-O chain bridging the two tips of a Ni nanocontact as shown in the insets of the right panels of Fig. 6.5 and Fig.6.7. In the case of the single oxygen atom (Fig. 6.5) the electron transport is almost 100% spin-polarized around the Fermi level for parallel (P) alignment of the magnetizations of the two Ni electrodes. Moreover, an orbital eigenchannel analysis [56] reveals that the transport is mainly due to two almost perfectly transmitting minority-spin channels composed of Ni $3d_1$ and O $2p_1$ orbitals, i.e. they correspond to the doubly-degenerate conduction band of the metastable half-metallic state in the perfect chain. Thus the half-metallic state which was suppressed in the idealized case of the infinite chain emerges in the more realistic situation of a short suspended chain. We can understand this phenomenon in terms of the orbital blocking mechanism proposed earlier in the context of Ni nanocontacts[55, 56]. The highest minority-spin valence band of the insulating state with FM order in the infinitely long chain has a strong contribution from the Ni $3d_0$ orbital which is not “compatible” with the geometry of the pyramid shaped Ni contacts, so that this band is blocked and thus cannot be occupied. Instead, the doubly-degenerate band composed of Ni $3d_1$ orbitals hybridized with O $2p_1$ orbitals is partially filled resulting in the half-metallic state which in the perfect chain is only metastable. Thus the orbital blocking by the contacts actually turns the chain into a half-metallic conductor. Consequently, the conductance is strongly suppressed in the case of antiparallel (AP) alignment of the magnetizations of the Ni electrodes as can be seen from the right panel of Fig. 6.5 and the MR becomes very large: $MR_1 \approx 90\%$ and $MR_2 \approx 700\%$.

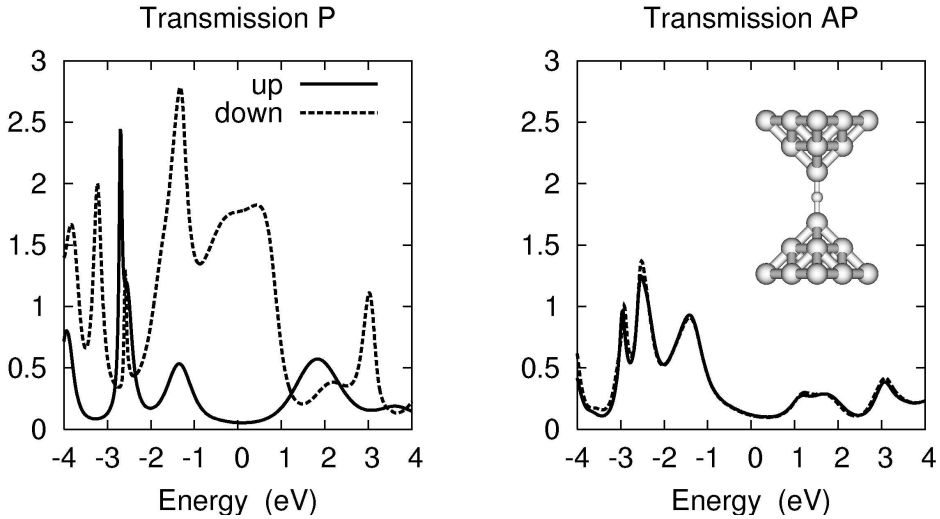


Figure 6.5: Transmission per spin channel in the case of P (left) and AP (right) alignment of the electrode magnetizations for NiO chain consisting of one oxygen atom bridging the two Ni tip atoms of the Ni electrodes as shown on the inset in the right panel. The separation of the two Ni tip atoms is 3.6\AA .

Fig. 6.6(b) shows the transmission per spin-channel for the Ni-O-Ni nanobridge calculated with GGA. Surprisingly, the transmission does not look very different from the transmission calculated with B3LYP for that case. Near the Fermi level the transmission is strongly spin-polarized: The transmission of the majority-spin channel is strongly suppressed while in the minority-spin channel essentially two perfectly transmitting channels contribute to the conductance.

This seems to be at odds with the band-structure calculated for the infinite one-dimensional chain, which suggests that there should be 5 minority- and 2 majority-spin channels contributing to the overall conductance. However, the geometry of the Ni nanocontact blocks the transmission of just these channels which due to the unphysical self-interaction of GGA have been raised to the Fermi level. Indeed, an orbital eigenchannel analysis [56] of the transmission reveals that only the doubly-degenerate band of type (d_1) contributes to the conductance of the minority-spin channel just as in the case of the B3LYP functional. The electrons in the flat minority-spin band of type (d_2) which actually crosses the Fermi level in the ideal case of the infinite chain are easily scattered as they present strongly localized electrons, and thus do not contribute to the overall conductance. The other minority-spin channel composed of Ni $3d_{3z^2-7r^2}$ orbitals does not contribute either to the conductance since the symmetry of the orbital is not compatible with the geometry of the two Ni electrodes - a mechanism to which we have referred to in previous work as *orbital blocking* [55]. The small but finite conductance in the majority-spin channel relates to the doubly-degenerate majority-spin band of type (d_1) of the infinite NiO chain raised to the Fermi level due to the self-interaction error.

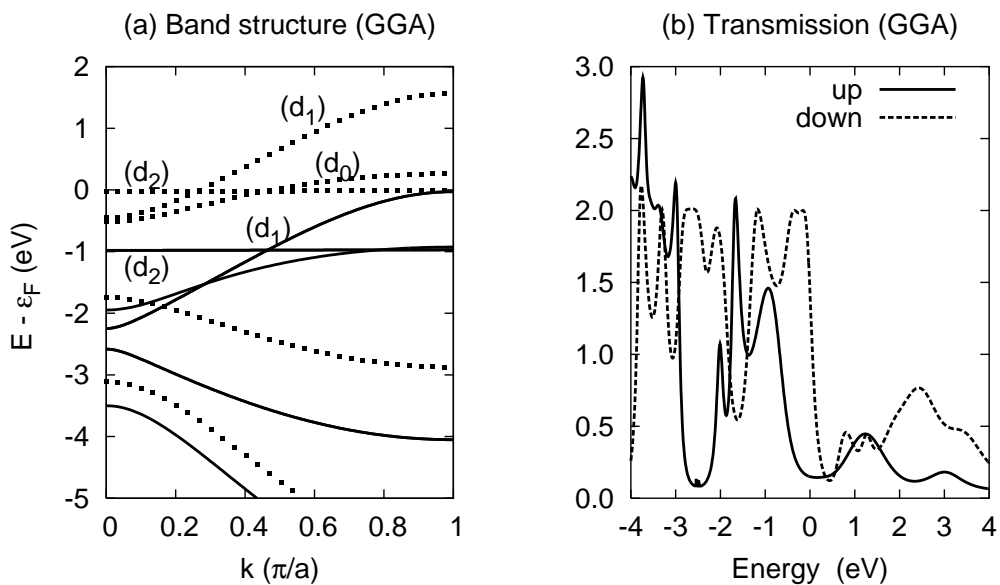


Figure 6.6: (a) GGA band structure of FM groundstate for a lattice spacing of 3.6\AA . Solid lines indicate majority-spin bands and dashed lines indicate minority-spin bands. (b) GGA Transmission per for NiO chain consisting of one oxygen atom bridging the two Ni tip atoms of the Ni electrodes as shown on the inset in the right panel of Fig. 6.5. The separation of the two Ni tip atoms is 3.6\AA .

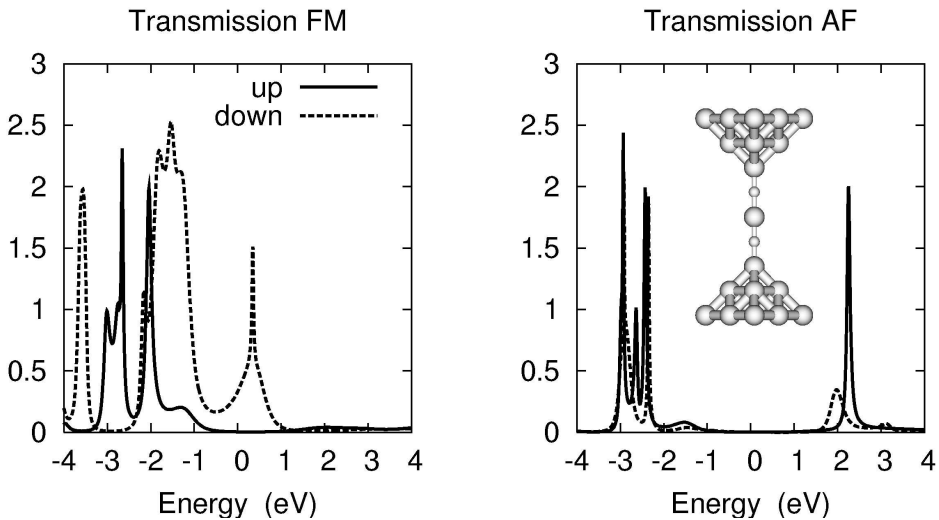


Figure 6.7: Transmission per spin channel for suspended chain consisting of a O-Ni-O bridge and the Ni tip atoms shown in inset of right panel in the case of FM order (left) and of AF order (right). For AF order the magnetization of the Ni atom in the center of the chain is reversed with respect to the two Ni tip atoms. Distance between a Ni tip atom and the center atom is 3.6\AA .

The (d_1) band only crosses the Fermi energy near the upper band edge where the band becomes flat. Thus the electrons in this channel are quite susceptible to scattering near the Fermi level resulting in a low transmission.

Varying the distance d between the Ni tip atoms leads to similar results as those shown in Fig. 6.5. For the P case the current through the chain is almost 100% spin-polarized with two open minority channels composed of Ni $3d_1$ and O $2p_1$ orbitals, while for the AP case it is strongly suppressed, resulting in very high MR values between 80% and 90% for MR_1 for d between 3.0\AA and 5.0\AA . Geometry relaxations for different values of the tip-tip distance show that for small distances the oxygen atom goes into a zigzag position. The bonding angle decreases with increasing distance until it becomes zero at 3.6\AA . Finally, the chain breaks for $d > 4.8\text{\AA}$. Thus the scattering is strong for small distances $d < 3.6\text{\AA}$ when the bonding angle is appreciable and for large stretching, $d > 4.2\text{\AA}$, resulting in a considerable reduction in the conduction of the two minority channels.

6.4 O-Ni-O bridge in Ni nanocontacts

In longer suspended chains the insulating state with FM order starts to emerge inside the chain and a way from the contacts. As a result the conductance is reduced as can be seen already in the case of the O-Ni-O bridge (Fig. 6.7). The minority-spin conduction is reduced considerably ($\sim 30\%$) compared to the case of the single oxygen bridge. On the other hand the conduction of the majority-spin channel becomes practically zero ($< 0.2\%$).

This can be understood by the fact that the residual majority-spin channel conductance of the single oxygen bridge is due to direct hopping of Ni s electrons between the electrodes and therefore vanishes when the distance between the electrodes is large. The finite minority-spin conductance opens up the possibility to an interesting phenomenon: When the middle Ni atom reverses its spin, the conductance drops to nearly zero (see right panel of Fig. 6.7) since the AF chain is insulating. In other words, this system behaves as a *single atom spin valve* which presents an extremely large MR even higher than that reported above for the single oxygen bridge: $MR_1 \approx 99\%$ and $MR_2 \approx 10,000\%$. Apart from controlling the magnetization direction of the central atom by a magnetic field, Fig. 6.4(a) suggests that a mechanical control of the spin valve (by stretching the chain) would also be possible.

6.5 Conclusions

In conclusion, we have shown that ideal one-dimensional infinite NiO chains could be either insulating or halfmetallic depending on the functional used in the calculation. Following the results obtained with the B3LYP hybrid functional one-dimensional NiO-chains are always insulating for all reasonable values of the lattice spacing but change from AF to FM order when stretched slightly out of equilibrium in contrast to bulk NiO which has always AF order. A halfmetallic conducting state which is normally metastable only becomes the ground state when the chain is stretched to unreasonable large values of the lattice spacing. The GGA functional on the other hand predicts NiO chains to be ferromagnetic halfmetallic conductors. Although it seems clear that the GGA results are affected by the insufficient cancellation of self-interaction error it is a priori not clear whether B3LYP predicts the correct ground state as it tends to localize electrons and thus tends to predict insulating behaviour. Thus the question of the electronic structure of infinite NiO chains remains open at the moment, and more sophisticated many-body techniques like GW or DMFT are probably required to answer this question.

However, in the more realistic case of short NiO chains suspended between Ni nanocontacts both B3LYP and GGA predict the chains to become strongly spin-polarized conductors which can be related to the corresponding halfmetallic states of the infinite NiO chain, i.e. the metastable halfmetallic state in the case of the B3LYP functional and the halfmetallic ground state in the case of the GGA functional. The emergence of almost perfect half-metallicity in suspended chains leads to a strong suppression of the current for AP alignment of the electrodes resulting in very large MR values of $MR_1 \approx 90\%$ and $MR_2 \approx 700\%$, respectively. This could perhaps explain to some extent the very large MR values in Ni nanocontacts obtained in some experiments [28, 35] where oxygen is likely to be present. Finally, the O-Ni-O bridge suspended between Ni electrodes operates as a *single atom spin valve* where the currentflow is controlled by the magnetization of a single atom.

7 Transport through magnetic Pt nanowires

Fabrication of metallic nanocontacts permits to probe the electronic and mechanical properties of conventional metals with unconventional atomic coordination[131]. Electron transport in these systems depends on the tiny fraction of atoms in the sample forming the atom-sized neck which have a reduced coordination and are responsible for the two-terminal resistance. Transport experiments can thereby probe the atomic and related electronic structure of these atoms and provide information about a fundamental question: How bulk properties evolve when the system reaches atomic sizes and atoms with full bulk coordination are no longer majority. A bulk property that is susceptible to change is magnetism. Bulk Pt, for instance, is a paramagnetic metal but a transition to a ferromagnetic state could be expected upon reduction of the atomic coordination with the concomitant increase of the density of states (DOS) at the Fermi energy beyond the Stoner limit. Density functional calculations [144, 145, 146] for one-dimensional infinite Pt chains support this hypothetical scenario, resulting in a ferromagnetic transition above a critical lattice spacing which, depending on the computational approach, can be below the equilibrium lattice constant[145]. The formation of local moments in real Pt nanocontacts would not be totally unexpected.

Formation of and electronic transport in finite Pt chains have been extensively studied experimentally [147, 148, 149, 150, 151]. Based upon the appearance of a peak at $G = 0.5 \times 2e^2/h = 0.5G_0$ in the conductance histogram Rodrigues *et al.* suggested that Pt and Pd nanocontacts could be spin polarized[151]. The origin of this peak has been later attributed to adsorbates[34] so that magnetism in Pt and Pd nanocontacts has not been confirmed experimentally yet. Previous theory work has addressed the formation of local moments in Pd nanocontacts[152] and in Co, Pd and Rh short chains sandwiched between Cu planes[153]. To the best of our knowledge theory work on Pt nanocontacts[154, 155, 156, 157] has overlooked the possibility of local magnetic order so far. In this chapter we perform density functional calculations of both the electronic structure and transport. We find that local magnetic order can develop spontaneously in Pt nanocontacts. Local magnetic moments as high as $1.2 \mu_B$ in low-coordination atoms are found. Interestingly, while transport is definitely spin polarized, the calculated total conductance of magnetic and non-magnetic Pt nanocontacts is very similar and in agreement with experimental data, explaining why magnetism has been unnoticed so far.

The electronic structure of various low dimensional structures of Pt which mimic actual nanocontacts are calculated in the density functional approximation, using either CRYSTAL03[98] and our *ab initio* transport package ALACANT that interfaces GAUSSIAN03 to implement the NEGF as explained in based on DFT electronic structure calculations Ch. 3. We use scalar relativistic (SR) pseudopotentials for the 60 inner electrons of the Pt atom and the remaining 18 electrons are treated using generalized gradient approximation (GGA) density functionals. The basis set used for all the calculations has

been optimized to describe bulk Pt as well as Pt surfaces[158]. Other basis sets such as LANL2DZ or SDD[47] have occasionally been employed for comparison. The main results do not depend on the choice of basis set.

7.1 Electronic and magnetic structure of atomic Pt chains

We first consider a perfect one-dimensional mono-strand Pt chain. Such an idealized system serves as a standard starting point to understand lower symmetry geometries. It also permits to test whether our LAO pseudopotential methodology reproduces the results obtained with SR all electron plane-wave calculations reported by Delin *et al.*[145]. In Fig. 7.1(a) we show the energy per atom as a function of the lattice constant a both for the paramagnetic (PM) and the ferromagnetic (FM) chain. They both have a minimum at $a = 2.4\text{\AA}$. The FM chain develops a non-negligible magnetic moment when the lattice constant goes beyond $a \simeq 2.6\text{\AA}$. This configuration is clearly lower in energy above that distance. The energy difference between the FM and the PM configurations is 16 meV per atom for $a = 2.7\text{\AA}$ and 33 meV per atom for $a = 2.8\text{\AA}$. The magnetic moment per atom reaches a saturation value of $1.2\mu_B$. The equilibrium distance, critical spacing, asymptotic magnetic moment and shape of the phase boundary obtained by us are similar to those obtained by Delin *et al.*[145] using a SR all-electron plane-wave calculation. Our results and those of Delin *et al.* underestimate the onset of the magnetic transition compared to calculations including spin-orbit coupling[145, 146] that predict that a magnetic moment forms already below the equilibrium distance.

The magnetic transition in the phase diagram [Fig. 1(b)] is compatible with the Stoner criterion for ferromagnetic instability. As the chain is stretched, the atom-atom coupling becomes weaker, the bands narrow down and so does the DOS ($\mathcal{D}(\epsilon)$). Since the integrated $\mathcal{D}(\epsilon)$ must be equal to the number of electrons per atom, narrowing of the DOS implies an increase of the $\mathcal{D}(\epsilon)$ [see Fig. 7.1(d)] and, therefore, an increase of the spin susceptibility, which is proportional to $\mathcal{D}(\epsilon_F)$. In Fig. 7.1(c) we show how the $\mathcal{D}(\epsilon_F)$ of the PM chain increases as a function of the lattice constant. The remarkable feature of Pt chains is that the Stoner instability occurs close to the equilibrium lattice spacing.

The electronic structure of the ideal Pt chain sheds some light on the electronic structure of the nanocontact. In Fig. 7.2 we show the energy bands for the ideal Pt chain both in the FM (left panel) and PM (right panel) configurations, for a lattice spacing $a = 2.8\text{\AA}$. We notice that the spectrum at $k = 0$ has four resolved energy levels per spin. These correspond to the $6s$ level, and the $5d$ levels which, because of the axial potential created by the neighboring atoms, split into 2 doublets E_1 , E_2 and one singlet A_1 . The E_1 and E_2 are linear combinations of orbitals with $L_z = \pm 1$ and $L_z = \pm 2$, respectively, whereas the A_1 singlet is a $L_z = 0$ orbital that hybridizes with the lower energy $6s$ orbital. The largest contribution to the DOS, and therefore to the magnetic instability, comes from the A_1 -like band at the edge of the Brillouin zone. However, the prominent role played by these bands in the magnetic behavior of Pt chains is in stark contrast with their role on the transport properties of Pt nanocontacts (see below and see also related work on Ni nanocontacts[55]). Four spin-degenerate bands cross the Fermi energy in the PM case whereas 7 spin-split bands do it in the FM chain. In the FM chains the number of spin minority channels is 6, and the number of spin majority channels is 1. Although spin-orbit interaction modifies significantly the bands [145], the number of bands at the Fermi energy is pretty similar in both cases. Therefore, one can anticipate that the number of

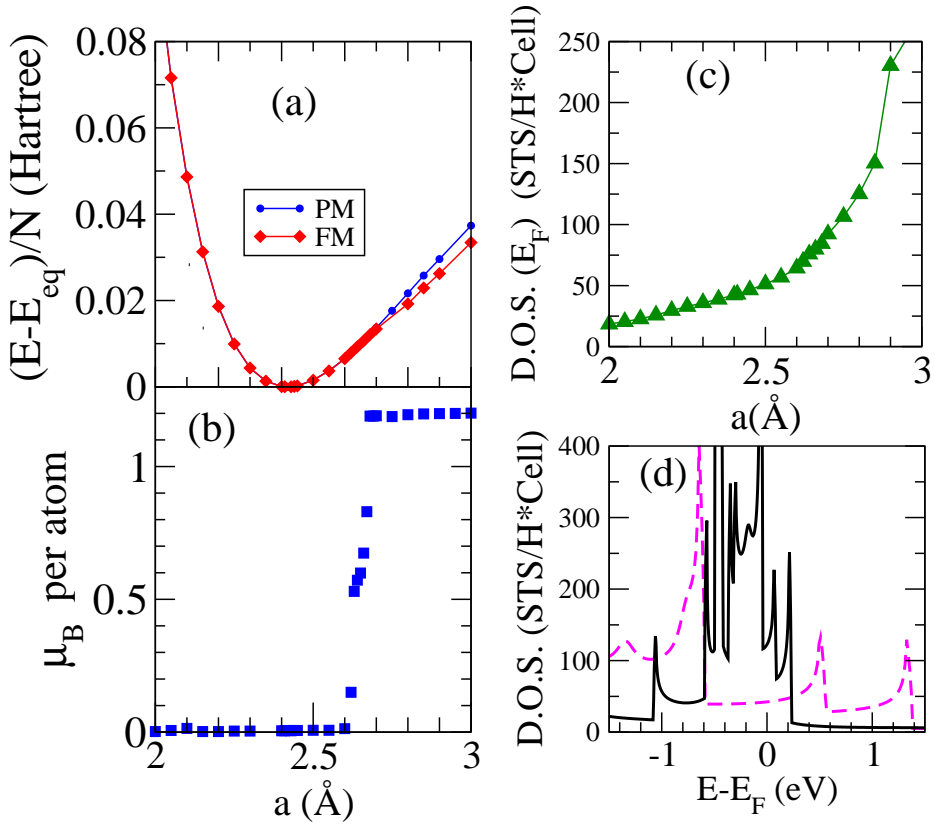


Figure 7.1: (Color online). (a) Energy per atom for a perfect monostrand Pt chain. (b) Magnetic moment per atom as a function of lattice spacing a . (c) DOS of the paramagnetic chain at the Fermi energy as a function of a . (d) D.O.S. as a function of energy for $a = 2.4$ Å (dashed) and $a = 2.8$ Å (solid)

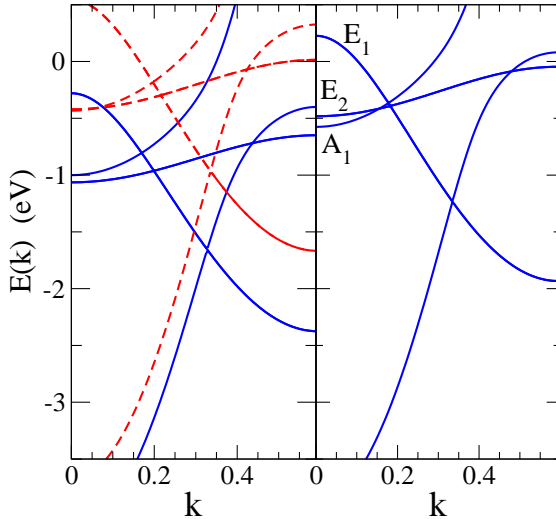


Figure 7.2: (Color online). Energy bands for ideal Pt chain with $a = 2.8\text{\AA}$. Left: ferromagnetic phase. Right: paramagnetic case.

open channels in the magnetic and non-magnetic Pt nanocontacts studied below should be roughly the same and thereby the conductance should be similar, although the spin polarization might well be large in the former case. The conductance of the ideal FM chain is $3.5G_0$, very far from the value of $0.5G_0$ that allegedly signals the emergence of magnetism and also far away from half of the conductance of the PM chain, so it is very unlikely that the celebrated half quantum can be attributed exclusively to magnetism.

Real Pt chains are typically less than five atoms long and are connected to bulk electrodes. Although not surprising, we have verified that magnetism survives in isolated short chains with $N_A = 3, 4$ and 5 Pt atoms. The equilibrium distance is 2.4\AA for all $N_A = 3, N_A = 4$, and $N_A = 5$. Interestingly, the short chains are always magnetic in the $N_A = 3$ and $N_A = 4$ cases and show a non-magnetic to magnetic crossover at $a = 2.6\text{\AA}$ in the $N_A = 5$ case, already similar to the ideal infinite chain. The total magnetic moment of all the $N_A = 3$ chains with $a < 3.0\text{\AA}$ is $4\mu_B$. The outer atoms have a magnetic moment of $1.36\mu_B$ and the central atom with larger coordination has a smaller magnetic moment of $1.29\mu_B$. In the case of $N_A = 4$ the total magnetic moment is $6\mu_B$, and their distribution is similar to the $N_A = 3$ case.

7.2 Transport through suspended Pt chains

The calculations above show that magnetism is present both in finite- and infinite-sized Pt systems with small atomic coordination. It remains to be seen that this holds true in nanocontacts where none or only few atoms have a small coordination (like in the case of formation of short chains), but these are strongly coupled to the bulk. In order to verify whether or not this is the case, we have calculated both electronic structure and transport for a model Pt nanocontact. It is formed by two opposite pyramids grown in the (001) crystallographic orientation of bulk Pt and joined by one atom which presents the lowest

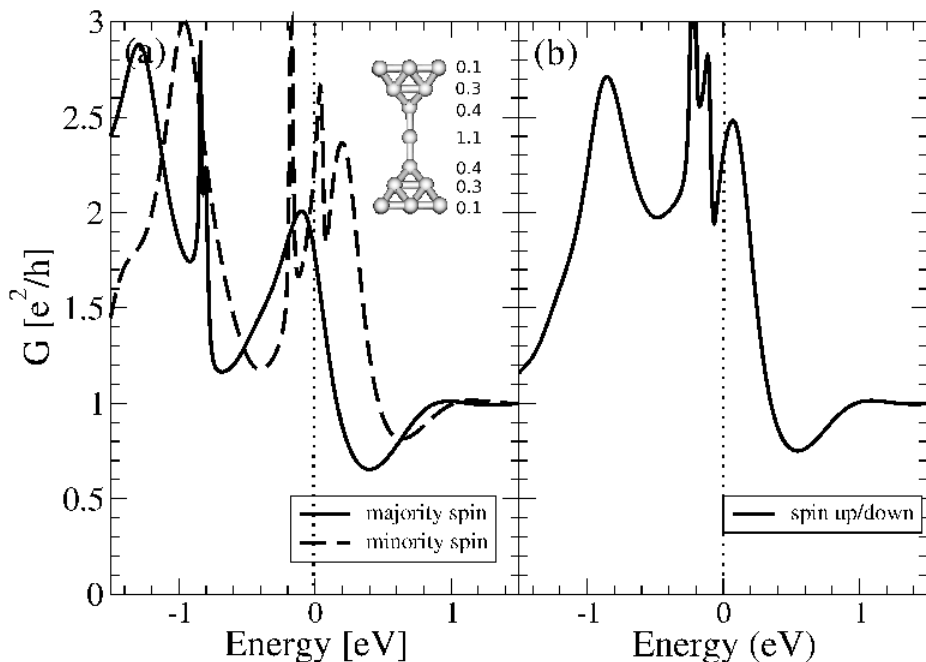


Figure 7.3: Conductance per spin channel for a nanocontact with a 3-atom Pt chain (see inset) for the magnetic solution (a) and the non-magnetic one (b). The atom-atom distance in the chain is 2.8\AA .

possible coordination [see inset in Fig. 7.3(a)]. Relaxation of the 11 inner atoms of the cluster has been performed starting from an equilibrium situation as a function of the distance d of the outer planes. Zig-zag configurations appear in the chain for small values of d (not shown)[157] until the three-atom chain straightens up (see inset in Fig. 7.3(a)) followed by a plastic deformation (not shown). This deformation can be in the form of a rupture or a precursor of the addition of a new atom to the chain which comes from one of the two 4-atom bases[144].

We now compute the transmission before the plastic deformation occurs (left panel in Fig. 7.3), where the atom-atom distance in the short chain is 2.82\AA . The value of the corresponding atomic-plane-averaged magnetic moments are also shown in the inset. As expected, it decreases for atoms in the bulk as the coordination reaches the bulk value. Some atomic realizations in the stretching process (like zig-zag ones) result in nanocontacts with smaller Pt-Pt distance and no magnetism, in agreement with the infinite chain phase diagram in Fig. 1. In contrast to the infinite chain, there are only three channels contributing to the total conductance for minority electrons and there are more than one (three) for majority ones. For the majority electrons these are a perfectly transmitting s -type channel and two partially open ($T = 0.4$) pd -type channels (one $p_x d_{xz}$ - and one $p_y d_{yz}$ - hybridized). The three minority channels have the same character as the majority channels, except that here the s -type channel does not transmit perfectly while the transmission of two pd -type channels is enhanced so that all three minority channels

have a transmission around 0.7. The other two remaining *pd*-like channels are responsible for the sharp resonances that appear around the Fermi level. The total conductance of the nanocontact in the FM case thus turns out to be around $4e^2/h = 2G_0$ which is only slightly larger than the average experimental value corresponding to the last plateau ($1.75G_0$), but, interestingly, barely differs from the value obtained when the possibility of magnetic order is ignored [around $2.3G_0$, see right panel in Fig. 7.3]. As in the case of the ideal chain, the FM conductance is not half of the PM conductance nor half of G_0 . To conclude this discussion we notice that although transport is only weakly spin polarized, magnetism brings the *pd*-like resonances up to the Fermi level compared to the non-magnetic case. These resonances may well give features in the low bias conductance not present if Pt were not magnetic.

7.3 Conclusions and Discussion

The main conclusion of this part is that density functional calculations predict that nanochains formed in Pt nanocontacts can be stretched as to become magnetic. The magnetic moment is localized mainly in the atoms with small coordination and does not modify appreciably the total conductance, although the transmission is moderately spin polarized. How robust are these results? It is well known that both local and gradient-corrected density functionals present some degree of electronic self-interaction, in contrast with the Hartree-Fock approximation. Self-interaction is larger for localized electrons and shifts the *d* bands upwards in energy, as shown in the case of Co, Ni and Pd one dimensional chains[159]. A number of schemes to avoid this problem, like LDA+U and Self-Interaction Correction functionals have been proposed. The method of choice between chemists is hybrid functionals[81] in which local and Hartree-Fock exchange (HFX) are combined and the self-interaction is reduced. We have calculated the magnetic phase diagram of the one dimensional Pt chain using the hybrid B3LYP functional[81] and found, somewhat expectedly, that magnetism is enhanced and that B3LYP infinite Pt chains are ferromagnetic down to the equilibrium distance ($a = 2.4\text{\AA}$). Both non-local exchange and spin-orbit coupling [145] enhance the stability of magnetism in Pt nanocontacts. This and previous results on Ni nanocontacts[55] lead us to believe that self-interaction is an issue in the electronic structure and transport properties of transition metal nanocontacts and further work is necessary along these lines[160].

The mean field picture of the electronic structure describes a static magnetic moment without preferred spatial direction. In reality the nanomagnet formed in the break junction is exchanged coupled dynamically to the Fermi sea of the conduction electrons of the electrodes. In the case of a spin $S = 1/2$ this can result in the formation of a Kondo singlet that would yield an anomaly in the zero bias conductance. For larger spins, the conduction electron sea cannot screen the spin completely so that the magnetic moment survives. The magnetic moment of the nanocontact in Fig. 3 is $S \approx 6$, comparable to that of single molecule magnets [161], making the formation of a Kondo singlet unlikely.

In the absence of spin-orbit interactions and external magnetic field a electronic configuration with total spin S has $2S + 1$ degenerate configurations corresponding to the spin pointing along different directions. However, spin-orbit interaction is strong in Pt and produces spin anisotropy, favoring orientation along the transport direction axis in the case of one dimensional chains[145]. Thermal fluctuations of the magnetic moment between these two configurations are quenched for temperatures smaller than the anisotropy barrier.

Departures from the easy axis orientation will be damped via electron-hole pair creation across the Fermi energy that would also result in small bias features in transport[162]. The application of a sufficiently strong magnetic field in the direction perpendicular to the easy axis moves the local magnetic moments away from their easy axis. This is known to change the number of open channels at the Fermi energy in both the case of Ni ideal chains[163] and in the case of ferromagnetic semiconductor tunnel junctions [164]. This effect, or maybe even larger, can be expected in Pt nanocontacts and could be used to detect the nanomagnetism experimentally.

8 Summary and Outlook

8.1 Overview of developed computational tools

In this thesis, I have studied spin transport through nanocontacts and nanowires, both with calculations of simplified models and with full *ab initio* calculations based on density functional theory (DFT). To this end various computational tools have been developed either from scratch or by extension of already existing code:

i) **SpinTrans**: This program for computing spin transport in simple models with Coulomb interaction (e.g. Hubbard model) in the *non-collinear* unrestricted Hartree-Fock approximation (NC-UHF), see also App.E has been developed from scratch in the first stage of the thesis. This program was applied for the self-consistent calculation of toy models of magnetic nanostructures to study the effect of non-collinear magnetization profiles on the transport presented in Ch. 4.

ii) **ALACANT**: The ALACANT (ALicante Ab-initio Computation Applied to Nano Transport) project was started in the year 2000 by professor J. J. Palacios in the Applied Physics department of the University of Alicante. It implements the NEGF formalism in connection with *ab initio* electronic structure calculations based on DFT, as explained in Ch.3. As a part of this thesis, the ALACANT package has been further developed in various aspects:

- The spin-unrestricted transport formalism was implemented into the package
- The entire program code which had been written in FORTRAN77 has been ported to FORTRAN90 in order to make use of modern programming techniques like the use of modules, dynamic memory allocation etc.
- A module for calculating self-energies for one-dimensional electrodes described by Hamiltonian and overlaps matrices which can be taken from ab-initio calculations has been implemented.
- An interface to the CRYSTAL *ab initio* program for crystalline systems has been developed.

8.2 Summary of results

With the developed computational tools various calculations of the electronic and magnetic structure and the transport properties of nanocontacts and nanowires have been performed. First, we have studied spin transport with simple models, namely a one-dimensional Hubbard chain in the ferromagnetic phase, in order to gain an understanding of the fundamental mechanisms of nanoscale spin transport. Neglecting the geometric aspects as well as the much more complex Hamiltonian and Hilbert space of real nanocontacts allowed to concentrate on the pure spin aspects of electron scattering by the magnetic

structure. We find that domain walls form self-consistently under the appropriate magnetic boundary conditions. Furthermore, we find that the longer the atomic chain the smoother the domain wall becomes, and the scattering by the domain wall is reduced since the spin-mixing transforms the spin of an incoming electron adiabatically into the opposite spin. Vice versa, for short necked nanocontacts (i.e. no chain formation) like is typical for Ni, the domain walls will be rather sharp, and thus the spin scattering by a domain wall formed in the neck of the nanocontact becomes maximal.

In order to investigate the question of the possibly huge BMR values in Ni nanocontacts we have performed *ab initio* calculations of the electronic structure and transport properties of Ni nanocontacts on the level of DFT. By comparing solutions with and without formation of a domain wall in the atomic neck of the nanocontact, we find that BMR is certainly not large in pure Ni nanocontacts, but rather moderate. This is due to the fact that a grand part of the a priori available spin-polarized channels which could in principle give rise to a large BMR are blocked by the geometry of a real nanocontact. On the other hand the spin-unpolarized *s*-type channel which does not give rise to any BMR is not affected by the geometry. Thus even in the DW configuration the conductance is appreciable ($\approx 2e^2/h$ compared to the $< 4e^2$ for the ferromagnetic solution). Another important conclusion that we can draw from our calculations is that disorder of the atoms in the nanocontact strongly reduces the spin-polarization of the current since it has a stronger effect on the transmission of the spin-polarized *d*-type channels than on the unpolarized *s*-type channels. Moderate BMR values for ferromagnetic nanocontacts has been confirmed recently by experiments with very clean samples under controlled conditions (ultra-high vacuum conditions, exclusion of any magnetostriction effects) [38, 37], and also by a number of theoretical papers[125].

Next, we have studied the electronic structure and transport properties of one-dimensional NiO chains, both ideal infinite ones, and short ones suspended between Ni nanocontacts. Indeed, it has been observed experimentally, that Ag which like Ni does not form atomic chains in a nanocontact, actually does form chains when oxygen is present [132], and it has been argued that the incorporation of oxygen atoms into the a chain actually stabilizes the chain [165]. In fact we find that NiO chains bridging the tip atoms of a Ni nanocontact are stable, and so NiO chains could in principle form when nanocontacts are fabricated in an oxygen atmosphere. Most importantly, we have found that short NiO chains can actually become almost perfect half-metallic conductors when suspended between Ni nanocontacts, i.e. the current becomes almost 100% spin-polarized. In fact, already a single oxygen atom bridging the tips of a Ni nanocontact can have such an effect. Consequently, this leads to a huge BMR of the order of the GMR effect, and could perhaps explain to some extent the large MR values obtained in some experiments [28, 35]. Another very important conclusion we can draw is that already a single atom can completely change the conductance behavior of an atomic-scale device.

The emergence of magnetism at the nanoscale in materials that are otherwise paramagnetic in bulk is a fascinating topic of Nano science, and has been observed for example in Au nanoclusters [166], and predicted for atomic chains of Pt and Pd with *ab initio* electronic structure calculations [57, 58]. In order to see whether conduction measurements of Pt nanocontacts could possibly reveal the magnetism of an atomic chain formed between the tip atoms of the nanocontact, we have performed *ab initio* electronic structure and transport calculations of atomic Pt chains suspended between the tips of a Pt nanocontact. We find that although suspended Pt chains are also magnetic, the conduc-

tance is very similar to the case when there would be no magnetism in the chain. Thus it seems not possible to decide experimentally whether Pt chains become magnetic or not by simple conductance measurements of Pt nanocontacts.

Furthermore, we can draw the following general conclusions:

i) The DFT based transport approach on the LDA level at small bias voltages seems to work reasonably well for metallic nanocontacts and nanowires, even when d -electrons are involved in the conduction. This is in agreement with theoretical studies which show that DFT calculations on the LDA or GGA level give a reasonable description of the electronic structure of bulk metals and metallic surfaces [167, 115], and corrections by methods like the GW approximation or DMFT which take into account electron correlations are often relatively small in the vicinity of the Fermi level [168, 169]. However, when going away from the purely metallic systems things become more complicated. NiO for example is a strongly correlated material, and both LDA and GGA fail in describing its electronic structure correctly. Also the problems of LDA/GGA of describing the electronic structure of molecules are notorious. Thus it must be doubted whether LDA or GGA can give a good description of nanoscale NiO e.g. oxidized Ni nanocontacts or one-dimensional NiO chains, or molecular conductors. On the other hand the semi-empirical DFT methods (e.g. hybrid functionals or LDA+U) often describe quite well the electronic structure of some bulk oxides with strongly correlated electron systems, and especially hybrid functionals are extremely successful in describing molecules. However, these methods require an adjustment of the empirical parameters by fitting with experimental results, which limits their predictive power. Also hybrid functionals often do not yield a satisfying description of metallic systems. Thus the electronic structure of a molecule in a molecular electronics device probably needs to be described by a hybrid functional while the metal electrodes for contacting the molecule are not well described by hybrid functionals but needs to be described on the LDA or GGA level.

ii) Magnetic nanocontacts and nanowires are quite sensitive to the atomic structure, i.e. distortions and defects often have a strong effect on the transport properties. This can be understood by the fact that the d -orbitals which are in fact responsible for the magnetism are very sensitive with respect to the geometry and thus d -electrons are easily scattered. On the other hand, the conduction channels composed of d -orbitals are the only channels that are actually spin-polarized and thus are the ones responsible for the magneto-resistive behavior. So exactly the channels that are interesting in the context of spintronics applications are not stable against variation of their atomic structures. Thus it is arguable whether magnetic atomic-size nanocontacts could one day serve as ingredients for nanoscale electronics. But rather they allow us to gain a fundamental understanding of conduction and the interplay with other physical processes at the atomic scale, and to develop an appropriate methodology for the description of nanoscale conductors. This might well prove essential for the development of new electronic devices in the near future.

8.3 Outlook

For the results presented in this thesis the spin-orbit coupling of the electrons has been neglected. This can be justified by the fact that the spin-orbit coupling is relatively small for not too heavy elements like Ni. For heavier elements like Pt on the other hand the spin-orbit coupling becomes comparable to the other energies and thus probably affects the electronic and magnetic structure of the material: As pointed out at the end of Ch. 7

the spin-orbit interaction introduces spin-anisotropy favoring the magnetization of the Pt chain to be oriented along the transport axis. Furthermore the spin-orbit coupling favors the onset of magnetism in atomic Pt chains as has been shown by *ab initio* calculations including the spin-orbit coupling [145, 146].

By applying a sufficiently strong magnetic field, the orientation of the magnetization of the chain atoms can be changed from the one favored by the spin-orbit coupling called the *easy axis*. This however affects the electronic structure of the atomic chain due to the coupling of the orbital degree of freedom to the spin degree of freedom and possibly alters the transport properties of the system resulting in *anisotropic* magneto-resistance (AMR) defined as the maximal change in resistance when rotating the magnetic field [163]. Despite the relatively small spin-orbit coupling of Ni and Fe in the order of 50meV, recent experiments have measured an appreciable AMR of 10-15% in the case of Ni nanocontacts [38, 170] and huge AMR of up to 75% in the case of Fe nanocontacts [171].

We have therefore implemented spin-orbit coupling into our *ab initio* transport program ALACANT and obtained first results for one-dimensional Ni chains with a scattering center as simplified models of real Ni nanocontacts. The calculated AMR values are similar to the experimentally measured AMR values. However, further investigations with more realistic geometries are needed in order to compare with the experiments as the spin-orbit coupling solely affects the *d*-electrons which are very sensitive to geometrical effects as has been discussed extensively in this thesis. Due to the strong spin-orbit coupling of Pt one might also expect that the magnetism of atomic Pt chains should give rise to a strong AMR signal which would thus give experimental evidence for the emergence of magnetism in atomic Pt chains. Thus it could be worthwhile to calculate the AMR of Pt nanocontacts from *ab initio* quantum transport calculations including the spin-orbit coupling.

An important problem for future nanoscale spintronics applications is the injection of spin-polarized currents from magnetic into non-magnetic nanoscopic conductors like paramagnetic nanowires, carbon nanotubes and organic molecules. The possibility of spin-injection into a non-magnetic material will very likely depend strongly on the atomic-scale properties of the contact or between the magnetic and non-magnetic material. It is thus of fundamental importance to study interfaces between magnetic and non-magnetic nanoscale conductors. Related to the question of spin injection is the problem of spin relaxation which designates the phenomenon that the spin-polarization of a current through a non-magnetic material decreases due to the precession of the electron spin caused by the spin-orbit coupling. Studying spin injection and spin relaxation in nanowires, nanotubes and organic molecules with *ab initio* quantum transport calculations thus defines an interesting future line of work.

A Representation of operators in non-orthogonal basis sets

The natural definition for the matrix \mathbf{A} of a one-body operator \hat{A} in a non-orthogonal basis set (NOBS) $\{|\alpha\rangle\}$ is simply by its matrix elements:

$$\mathbf{A} = (A_{\alpha\beta}) = \left(\langle\alpha|\hat{A}|\beta\rangle\right). \quad (\text{A.1})$$

However, the representation of an operator in a NOBS is not that simple:

$$\hat{A} = \sum_{\alpha,\beta} |\alpha\rangle(\mathbf{S}^{-1}\mathbf{A}\mathbf{S}^{-1})_{\alpha\beta}\langle\beta| \quad (\text{A.2})$$

where $\mathbf{S} = (S_{\alpha\beta}) = (\langle\alpha|\beta\rangle)$ is the overlap matrix for the basis set. It is easy to see that this definition leads results in the matrix elements $A_{\alpha\beta}$ defined above. Then the identity operator in the NOBS representation is given by

$$\hat{1} = \sum_{\alpha,\beta} |\alpha\rangle(\mathbf{S}^{-1})_{\alpha\beta}\langle\beta|, \quad (\text{A.3})$$

which is also easy to proof.

Now we define a second matrix

$$\tilde{\mathbf{A}} := \mathbf{S}^{-1}\mathbf{A}\mathbf{S}^{-1}, \quad (\text{A.4})$$

which is the matrix that appears above in the representation of the operator in a NOBS.

One should take care when using the representation of an operator in a NOBS. For example, the matrix element of an operator between two non-orthogonal orbitals $|\alpha\rangle, |\beta\rangle$ can be zero, $\langle\alpha|\hat{A}|\beta\rangle = 0$, but the corresponding matrix element of the matrix $\tilde{\mathbf{A}}$ does not necessarily vanish due to the multiplication with the inverse of the overlap matrix on both sides. Thus there is actually a non-zero contribution of the two orbitals to the operator although the corresponding matrix element of the operator is zero

Orthogonalizing the basis set by the Löwdin orthogonalization scheme [70], the matrices \mathbf{A} and $\tilde{\mathbf{A}}$ are transformed to the matrix $\mathbf{A}^\perp = (\langle i|\hat{A}|j\rangle)$ defined in the new orthogonal basis set $\{|i\rangle\}$ according to:

$$\mathbf{A}^\perp = \mathbf{S}^{-1/2}\mathbf{A}\mathbf{S}^{-1/2} = \mathbf{S}^{+1/2}\tilde{\mathbf{A}}\mathbf{S}^{+1/2}. \quad (\text{A.5})$$

Though there are also other orthogonalization schemes, the Löwdin scheme is particularly useful in the context of quantum chemistry methods based on atomic orbitals as the center of the orthogonalized orbital remains centered on the same atom as the original non-orthogonal orbital.

A Representation of operators in non-orthogonal basis sets

B Partitioning method

As explained in Ch. 2 we model the transport problem by dividing the system in three parts. Two semi-infinite leads (L) and (R) with bulk electronic structure are connected to a finite region called device (D). In a local basis set the Hamiltonian and the overlap matrix of the system are given by (2.13) and (2.14). Dividing the F matrix into submatrices in a similar manner we obtain the following matrix equation:

$$\begin{pmatrix} z\mathbf{S}_L - \mathbf{H}_L & z\mathbf{S}_{LD} - \mathbf{H}_{LD} & \mathbf{0}_{RL} \\ z\mathbf{S}_{DL} - \mathbf{H}_{DL} & z\mathbf{S}_D - \mathbf{H}_D & z\mathbf{S}_{DR} - \mathbf{H}_{DR} \\ \mathbf{0}_{RL} & z\mathbf{S}_{RD} - \mathbf{H}_{RD} & z\mathbf{H}_R - \mathbf{H}_R \end{pmatrix} \times \\ \times \begin{pmatrix} \tilde{\mathbf{G}}_L(z) & \tilde{\mathbf{G}}_{LD}(z) & \tilde{\mathbf{G}}_{LR}(z) \\ \tilde{\mathbf{G}}_{DL}(z) & \tilde{\mathbf{G}}_D(z) & \tilde{\mathbf{G}}_{DR}(z) \\ \tilde{\mathbf{G}}_{RL}(z) & \tilde{\mathbf{G}}_{RD}(z) & \tilde{\mathbf{G}}_R(z) \end{pmatrix} = \begin{pmatrix} \mathbf{1}_L & \mathbf{0}_{LD} & \mathbf{0}_{LR} \\ \mathbf{0}_{DL} & \mathbf{1}_D & \mathbf{0}_{DR} \\ \mathbf{0}_{RL} & \mathbf{0}_{RD} & \mathbf{1}_R \end{pmatrix}. \quad (\text{B.1})$$

This yields 9 equations for the 9 sub-matrices of the GF $\tilde{\mathbf{G}}$. We can resolve this matrix equation columnwise. Multiplying all rows of $ES - \mathbf{H}$ with the first column of $\tilde{\mathbf{G}}$ yields three equations for $\tilde{\mathbf{G}}_L$, $\tilde{\mathbf{G}}_{DL}$ and $\tilde{\mathbf{G}}_{RL}$ which yield:

$$\tilde{\mathbf{G}}_L(z) = (z\mathbf{S}_L - \mathbf{H}_L - \tilde{\Sigma}_{D+R}(z))^{-1} \quad (\text{B.2})$$

$$\tilde{\mathbf{G}}_{DL}(z) = \tilde{\mathbf{g}}_{D+R}(z) (\mathbf{H}_{DL} - z\mathbf{S}_{DL}) \tilde{\mathbf{G}}_L(z) \quad (\text{B.3})$$

$$\tilde{\mathbf{G}}_{RL}(z) = \tilde{\mathbf{g}}_R(z) (\mathbf{H}_{RD} - z\mathbf{S}_{RD}) \tilde{\mathbf{G}}_{DL}(z) \quad (\text{B.4})$$

Similarly we obtain from multiplication with the second column:

$$\tilde{\mathbf{G}}_D(z) = (z\mathbf{S}_D - \mathbf{H}_D - \tilde{\Sigma}_L(z) - \tilde{\Sigma}_R(z))^{-1} \quad (\text{B.5})$$

$$\tilde{\mathbf{G}}_{LD}(z) = \tilde{\mathbf{g}}_L(z) (\mathbf{H}_{LD} - z\mathbf{S}_{LD}) \tilde{\mathbf{G}}_D(z) \quad (\text{B.6})$$

$$\tilde{\mathbf{G}}_{RD}(z) = \tilde{\mathbf{g}}_R(z) (\mathbf{H}_{RD} - z\mathbf{S}_{RD}) \tilde{\mathbf{G}}_D(z) \quad (\text{B.7})$$

And finally from multiplication with the third column, we obtain:

$$\tilde{\mathbf{G}}_R(z) = (z\mathbf{S}_R - \mathbf{H}_R - \tilde{\Sigma}_{D+L}(z))^{-1} \quad (\text{B.8})$$

$$\tilde{\mathbf{G}}_{DR}(z) = \tilde{\mathbf{g}}_{D+L}(z) (\mathbf{H}_{DR} - z\mathbf{S}_{DR}) \tilde{\mathbf{G}}_R(z) \quad (\text{B.9})$$

$$\tilde{\mathbf{G}}_{LR}(z) = \tilde{\mathbf{g}}_L(z) (\mathbf{H}_{LD} - z\mathbf{S}_{LD}) \tilde{\mathbf{G}}_{DR}(z) \quad (\text{B.10})$$

We have introduced the Green's functions of the isolated left and right lead $\tilde{\mathbf{g}}_L$ and $\tilde{\mathbf{g}}_R$ and the corresponding self-energies $\tilde{\Sigma}_L$ and $\tilde{\Sigma}_R$:

$$\tilde{\mathbf{g}}_L(z) := (z\mathbf{S}_L - \mathbf{H}_L)^{-1} \quad (\text{B.11})$$

$$\tilde{\Sigma}_L(z) := (\mathbf{H}_{DL} - z\mathbf{S}_{DL}) \tilde{\mathbf{g}}_L(z) (\mathbf{H}_{LD} - z\mathbf{S}_{LD}) \quad (\text{B.12})$$

$$\tilde{\mathbf{g}}_R(z) := (z\mathbf{S}_R - \mathbf{H}_R)^{-1} \quad (\text{B.13})$$

$$\tilde{\Sigma}_R(z) := (\mathbf{H}_{DR} - z\mathbf{S}_{DR}) \tilde{\mathbf{g}}_R(z) (\mathbf{H}_{RD} - z\mathbf{S}_{RD}) \quad (\text{B.14})$$

B Partitioning method

Furthermore, we have defined the Green's function of the device plus the left lead only, $\tilde{\mathbf{g}}_{D+L}$, of the device plus the right lead only, $\tilde{\mathbf{g}}_{D+R}$, and the corresponding self-energies $\tilde{\mathbf{\Sigma}}_{D+L}$ and $\tilde{\mathbf{\Sigma}}_{D+R}$ each one representing the coupling of one of the leads to the device and the other lead:

$$\tilde{\mathbf{g}}_{D+L}(z) := (z\mathbf{S}_D - \mathbf{H}_D - \tilde{\mathbf{\Sigma}}_L(z))^{-1} \quad (\text{B.15})$$

$$\tilde{\mathbf{g}}_{D+R}(z) := (z\mathbf{S}_D - \mathbf{H}_D - \tilde{\mathbf{\Sigma}}_R(z))^{-1} \quad (\text{B.16})$$

$$\tilde{\mathbf{\Sigma}}_{D+R}(z) := (\mathbf{H}_{RD} - z\mathbf{S}_{RD})\tilde{\mathbf{g}}_{D+L}(z)(\mathbf{H}_{DR} - z\mathbf{S}_{DR}) \quad (\text{B.17})$$

$$\tilde{\mathbf{\Sigma}}_{D+L}(z) := (\mathbf{H}_{LD} - z\mathbf{S}_{LD})\tilde{\mathbf{g}}_{D+R}(z)(\mathbf{H}_{DL} - z\mathbf{S}_{DL}) \quad (\text{B.18})$$

C Self-energy of a one-dimensional lead

Here we will derive the Dyson equation (2.42) for the calculation of the self-energy of the semi-infinite right lead. The derivation of the Dyson equation for the left lead (2.41) goes in a completely analogous way.

The Hamiltonian matrix \mathbf{H}_R of the (isolated) semi-infinite right electrode is defined in eq. (2.16) as:

$$\mathbf{H}_R = \begin{pmatrix} \mathbf{H}_0 & \mathbf{H}_1 & & \mathbf{0} \\ \mathbf{H}_1^\dagger & \mathbf{H}_0 & \mathbf{H}_1 & \\ & \mathbf{H}_1^\dagger & \mathbf{H}_0 & \mathbf{H}_1 \\ \mathbf{0} & & \ddots & \ddots & \ddots \end{pmatrix}. \quad (\text{C.1})$$

and the overlap matrix is given in eq. (2.18) as:

$$\mathbf{S}_R = \begin{pmatrix} \mathbf{S}_0 & \mathbf{S}_1 & & \mathbf{0} \\ \mathbf{S}_1^\dagger & \mathbf{S}_0 & \mathbf{S}_1 & \\ & \mathbf{S}_1^\dagger & \mathbf{S}_0 & \mathbf{S}_1 \\ \mathbf{0} & & \ddots & \ddots & \ddots \end{pmatrix} \quad (\text{C.2})$$

To obtain the self-energy of the lead we have to calculate the GF of the lead from its defining equation:

$$(z\mathbf{S}_R - \mathbf{H}_R)\tilde{\mathbf{g}}_R(z) = \mathbf{1}. \quad (\text{C.3})$$

In the same way as the Hamiltonian and the overlap matrix we subdivide the GF matrix $\tilde{\mathbf{g}}_R$ into sub-matrices corresponding to the unit cells of the lead. Now the above equation for the right lead's GF reads:

$$\begin{pmatrix} z\mathbf{S}_0 - \mathbf{H}_0 & z\mathbf{S}_1 - \mathbf{H}_1 & & \\ z\mathbf{S}_1^\dagger - \mathbf{H}_1^\dagger & z\mathbf{S}_0 - \mathbf{H}_0 & z\mathbf{S}_1 - \mathbf{H}_1 & \\ & \ddots & \ddots & \ddots \end{pmatrix} \begin{pmatrix} \tilde{\mathbf{g}}_{1,1} & \tilde{\mathbf{g}}_{1,2} & \cdots \\ \tilde{\mathbf{g}}_{2,1} & \tilde{\mathbf{g}}_{2,2} & \cdots \\ \vdots & \vdots & \ddots \end{pmatrix} = \begin{pmatrix} \mathbf{1} & \mathbf{0} & \cdots \\ \mathbf{0} & \mathbf{1} & \ddots \\ \vdots & \ddots & \ddots \end{pmatrix}. \quad (\text{C.4})$$

As explained in Sec.2.2 it suffices to calculate the ‘‘surface’’ GF, i.e. $\tilde{\mathbf{g}}_{1,1}$. From multiplication of the 1st, the 2nd and so on until the n -th line of $(z\mathbf{S}_R - \mathbf{H}_R)$ with the 1st column of $\tilde{\mathbf{g}}_R(z)$ we get the following chain of equations:

$$(z\mathbf{S}_0 - \mathbf{H}_0)\tilde{\mathbf{g}}_{1,1}(z) + (z\mathbf{S}_1 - \mathbf{H}_1)\tilde{\mathbf{g}}_{2,1}(z) = \mathbf{1} \quad (\text{C.5})$$

$$(z\mathbf{S}_1^\dagger - \mathbf{H}_1^\dagger)\tilde{\mathbf{g}}_{1,1}(z) + (z\mathbf{S}_0 - \mathbf{H}_0)\tilde{\mathbf{g}}_{2,1}(z) + (z\mathbf{S}_1 - \mathbf{H}_1)\tilde{\mathbf{g}}_{3,1}(z) = \mathbf{0} \quad (\text{C.6})$$

⋮

$$(z\mathbf{S}_1^\dagger - \mathbf{H}_1^\dagger)\tilde{\mathbf{g}}_{n-1,1}(z) + (z\mathbf{S}_0 - \mathbf{H}_0)\tilde{\mathbf{g}}_{n,1}(z) + (z\mathbf{S}_1 - \mathbf{H}_1)\tilde{\mathbf{g}}_{n+1,1}(z) = \mathbf{0} \quad (\text{C.7})$$

C Self-energy of a one-dimensional lead

For $n > 1$ the equations for determining $\tilde{\mathbf{g}}_{n,1}(z)$ all have the same structure:

$$(z\mathbf{S}_0 - \mathbf{H}_0)\tilde{\mathbf{g}}_{n,1}(z) = (\mathbf{H}_1^\dagger - z\mathbf{S}_1^\dagger)\tilde{\mathbf{g}}_{n-1,1}(z) + (\mathbf{H}_1 - z\mathbf{S}_1)\tilde{\mathbf{g}}_{n+1,1}(z). \quad (\text{C.8})$$

We define a transfer matrix for $n > 1$ by:

$$\mathbf{T}_{n-1,n}(z)\tilde{\mathbf{g}}_{n-1,1}(z) = \tilde{\mathbf{g}}_{n,1}(z). \quad (\text{C.9})$$

The transfer matrix thus transfers information from site $n-1$ to site n of the lead, i.e. from the left to the right. Multiplying Eq. (C.8) by $(\tilde{\mathbf{g}}_{n-1,1})^{-1}$ we obtain:

$$(z\mathbf{S}_0 - \mathbf{H}_0)\mathbf{T}_{n-1,n}(z) = (\mathbf{H}_1^\dagger - z\mathbf{S}_1^\dagger) + (\mathbf{H}_1 - z\mathbf{S}_1)\mathbf{T}_{n,n+1}(z)\mathbf{T}_{n-1,n}(z) \quad (\text{C.10})$$

Reordering we obtain the following iterative equation for the transfer matrices:

$$\mathbf{T}_{n-1,n}(z) = (z\mathbf{S}_0 - \mathbf{H}_0 - (\mathbf{H}_1 - z\mathbf{S}_1)\mathbf{T}_{n,n+1}(z))^{-1}(\mathbf{H}_1^\dagger - z\mathbf{S}_1^\dagger) \quad (\text{C.11})$$

Since the electrode is semi-infinite it looks the same from each unit cell when looking to the right. Thus a given $\tilde{\mathbf{g}}_{n-1,1}$, results always in the same $\tilde{\mathbf{g}}_{n,1}$ independent of n . Thus the transfer matrix must be independent of n : $\mathbf{T}_{n-1,n}(z) \equiv \mathbf{T}(z)$, and Eq. (C.11) allows to determine the $\mathbf{T}(z)$ self-consistently.

We define the self-energy as $\Sigma(z) := (\mathbf{H}_1 - z\mathbf{S}_1)\mathbf{T}(z)$, and obtain the Dyson equation for the self-energy:

$$\Sigma(z) = (\mathbf{H}_1 - z\mathbf{S}_1)(z\mathbf{S}_0 - \mathbf{H}_0 - \Sigma(z))^{-1}(\mathbf{H}_1^\dagger - z\mathbf{S}_1^\dagger). \quad (\text{C.12})$$

We will now see that this self-energy is indeed identical to the one defined for the right lead in eq. (2.38), i.e. $\Sigma(z) \equiv \tilde{\Sigma}_r(E)$. By plugging in the definition of the transfer matrix, eq. (C.9), into eq. (C.5) for determining the surface GF, $\tilde{\mathbf{g}}_{1,1}$ we find:

$$\begin{aligned} (z\mathbf{S}_0 - \mathbf{H}_0)\tilde{\mathbf{g}}_{1,1}(z) + (z\mathbf{S}_1 - \mathbf{H}_1)\mathbf{T}(z)\tilde{\mathbf{g}}_{1,1}(z) &= \mathbf{1} \\ \Rightarrow (z\mathbf{S}_0 - \mathbf{H}_0 + \Sigma(z))\tilde{\mathbf{g}}_{1,1}(z) &= \mathbf{1}, \end{aligned} \quad (\text{C.13})$$

where in the last step we have made use of the definition of the self-energy. Thus we obtain for the surface GF of the right lead:

$$\tilde{\mathbf{g}}_{1,1}(z) = (z\mathbf{S}_0 - \mathbf{H}_0 + \Sigma(z))^{-1}. \quad (\text{C.14})$$

And vice-versa the self-energy can be expressed in terms of the surface GF:

$$\Sigma(z) = (\mathbf{H}_1 - z\mathbf{S}_1)\tilde{\mathbf{g}}_{1,1}(z)(\mathbf{H}_1^\dagger - z\mathbf{S}_1^\dagger). \quad (\text{C.15})$$

This proves that the self-energy $\Sigma(z)$ defined above in terms of the transfer matrix is identical to the self-energy $\tilde{\Sigma}_r(z)$ defined earlier in Sec.2.2 so that the self-energy $\tilde{\Sigma}_r(z)$ can be calculated iteratively by the Dyson equation (2.42).

The proof for the left lead runs completely analogously. The surface GF of the left lead is now:

$$\tilde{\mathbf{g}}_{-1,-1}(z) = (z\mathbf{S}_0 - \mathbf{H}_0 + \tilde{\Sigma}_l(z))^{-1}. \quad (\text{C.16})$$

D Bethe lattices

In this appendix we discuss how self-energies for Bethe lattices (BL) used to describe the leads are calculated. A BL is generated by connecting a site with N nearest-neighbors in directions that could be those of a particular crystalline lattice. The new N sites are each one connected to $N - 1$ different sites and so on and so forth. The generated lattice has the actual local topology (number of neighbors and crystal directions) but has no rings, and thus does not describe the long range order characteristic of real crystals. Let n be a generic site connected to one preceding neighbor $n - 1$ and $N - 1$ neighbors of the following shell ($n + i$ with $i = 1, \dots, N - 1$). Dyson's equation for an arbitrary non-diagonal Green's function is

$$(E\mathbf{I} - \mathbf{H}_0)\mathbf{G}_{n,k} = \mathbf{V}_{n,n-1}\mathbf{G}_{n-1,k} + \sum_{i=1,\dots,N-1} \mathbf{V}_{n,i}\mathbf{G}_{i,k} \quad (\text{D.1})$$

where k is an arbitrary site, E the energy, and $\mathbf{V}_{i,j}$ is a matrix that incorporates interactions between orbitals at sites i and j (bold capital characters are used to denote matrices). \mathbf{H}_0 is a diagonal matrix containing the orbital levels and \mathbf{I} is the identity matrix. Then, we define a transfer matrix as

$$\mathbf{T}_{i-1,i}\mathbf{G}_{i-1,j} = \mathbf{G}_{i,j} \quad (\text{D.2})$$

Multiplying Eq. (D.1) by the inverse of $\mathbf{G}_{n-1,n}$ we obtain,

$$(E\mathbf{I} - \mathbf{H}_0)\mathbf{T}_{n-1,n} = \mathbf{V}_{n,n-1} + \left(\sum_{i=1,\dots,N-1} \mathbf{V}_{n,i}\mathbf{T}_{n,i} \right) \mathbf{T}_{n-1,n} \quad (\text{D.3})$$

Due to the absence of rings the above equation is valid for any set of lattice sites, and, thus, solving the BL is reduced to a calculation of a few transfer matrices. Note that a transfer matrix such as that of Eq. (D.2) could also be defined in a crystalline lattice but, in that case it would be useless.

Eq. (D.3) can be solved iteratively,

$$\mathbf{T}_{n-1,n} = \left[E\mathbf{I} - \mathbf{H}_0 - \sum_{i=1,\dots,N-1} \mathbf{V}_{n,i}\mathbf{T}_{n,i} \right]^{-1} \mathbf{V}_{n,n-1} \quad (\text{D.4})$$

If the orbital basis set and the lattice have full symmetry (including inversion symmetry) the different transfer matrices can be obtained from just a single one through appropriate rotations. However this is not always the case (see below).

Before proceeding any further we define self-energies that can be (and commonly are) used in place of transfer matrices,

$$\Sigma_{i,j} = \mathbf{V}_{i,j}\mathbf{T}_{i,j} \quad (\text{D.5})$$

D Bethe lattices

Eq. (D.4) is then rewritten as,

$$\boldsymbol{\Sigma}_{n-1,n} = \mathbf{V}_{n-1,n} \left[E\mathbf{I} - \mathbf{H}_0 - \sum_{i=1,\dots,N-1} \boldsymbol{\Sigma}_{n,i} \right]^{-1} \mathbf{V}_{n-1,n}^\dagger \quad (\text{D.6})$$

where we have made use of the general property $\mathbf{V}_{n,n-1} = \mathbf{V}_{n-1,n}^\dagger$.

As discussed hereafter, in a general case of no symmetry this would be a set of N coupled equations ($2N$ if there is no inversion symmetry). Symmetry can be broken due to either the spatial atomic arrangement, the orbitals on the atoms that occupy each lattice site, or both. When no symmetry exists, the following procedure has to be followed to obtain the self-energy in an arbitrary direction. The method is valid for any basis set or lattice. Let τ_i be the N nearest-neighbor directions of the lattice we are interested in and \hat{V}_{τ_i} the interatomic interaction matrix in these directions. To make connection with the notation used above note that the vector that joins site $n-1$ to site n , namely, $\mathbf{r}_n - \mathbf{r}_{n-1}$ would necessarily be one of the lattice directions of the set τ_i . The self-energies associated to each direction have to be obtained from the following set of $2N$ coupled self-consistent equations,

$$\boldsymbol{\Sigma}_{\tau_i} = \mathbf{V}_{\tau_i} [E\mathbf{I} - \mathbf{H}_0 - (\boldsymbol{\Sigma}_T - \boldsymbol{\Sigma}_{\bar{\tau}_i})]^{-1} \mathbf{V}_{\tau_i}^\dagger \quad (\text{D.7})$$

$$\boldsymbol{\Sigma}_{\bar{\tau}_i} = \mathbf{V}_{\bar{\tau}_i} [E\mathbf{I} - \mathbf{H}_0 - (\boldsymbol{\Sigma}_T - \boldsymbol{\Sigma}_{\tau_i})]^{-1} \mathbf{V}_{\bar{\tau}_i}^\dagger, \quad (\text{D.8})$$

where $i = 1, \dots, N$ and $\bar{\tau}_i = -\tau_i$. \mathbf{V}_{τ_i} is the interatomic interaction in the τ_i direction, and $\boldsymbol{\Sigma}_T$ and $\boldsymbol{\Sigma}_{\bar{T}}$ are the sums of the self-energy matrices entering through all the Cayley tree branches attached to an atom and their inverses, respectively, *i.e.*,

$$\boldsymbol{\Sigma}_T = \sum_{i=1}^N \boldsymbol{\Sigma}_{\tau_i} \quad (\text{D.9})$$

$$\boldsymbol{\Sigma}_{\bar{T}} = \sum_{i=1}^N \boldsymbol{\Sigma}_{\bar{\tau}_i}. \quad (\text{D.10})$$

This set of $2N$ matricidal equations has to be solved iteratively. It is straightforward to check that, in cases of full symmetry, it reduces to the single equation. The local density of states can be obtained from the diagonal Green matrix,

$$\mathbf{G}_{n,n} = \left[E\mathbf{I} - \mathbf{H}_0 - \sum_{i=1,\dots,N} \boldsymbol{\Sigma}_{\tau_i} \right]^{-1} \quad (\text{D.11})$$

E Non-Collinear Unrestricted Hartree-Fock Approximation

The standard Unrestricted Hartree-Fock theory (UHF) only allows for spin-polarized ground states, i.e. the UHF Hamiltonian commutes with one component of the total spin operator, e.g. \hat{S}_z , so that the ground state $|\Psi_0\rangle$ is an eigenstate to \hat{S}_z . For atoms and molecules this is a good property of the UHF Hamiltonian. However, in transport problems, this symmetry might be broken if the magnetizations of the two macroscopic leads are aligned non-collinear or anti-parallel.

Therefore, we will derive a non-collinear formulation of unrestricted Hartree-Fock theory (NC-UHF). As in UHF we want to minimize the total energy of a single Slater-determinant of an N -electron system,

$$|\Psi_0\rangle = |\chi_1, \dots, \chi_N\rangle \quad (\text{E.1})$$

described by the many-body Hamiltonian

$$\hat{H} := \hat{H}_0 + \hat{V}_c := \sum_i \hat{h}_0(i) + \sum_{i<j} \hat{v}_c(i, j). \quad (\text{E.2})$$

Only now the molecular orbitals are a linear combination of atomic orbitals with different spins, i.e. we explicitly allow for spin-mixing:

$$|\chi_a\rangle = \sum_{i,\sigma} c_{ia}^\sigma |\phi_i^\sigma\rangle, \quad (\text{E.3})$$

where $|\phi_i^\sigma\rangle = |\phi_i\rangle \otimes |\sigma\rangle$.

We assume that the molecular orbitals and the atomic orbitals are orthonormal:

$$\langle \chi_a | \chi_b \rangle = \delta_{ab} \text{ and } \langle \phi_i | \phi_j \rangle = \delta_{ij} \quad (\text{E.4})$$

In order to find the molecular orbitals that minimize the total energy with the constrained of orthogonal molecular orbitals we have to minimize the Lagrangian

$$\mathcal{L}[\{\chi_a\}] = E_0[\{\chi_a\}] - \sum_{a,b} \epsilon_{ab} (\langle \chi_a | \chi_b \rangle - \delta_{ab}), \quad (\text{E.5})$$

where $E_0[\{\chi_a\}] = \langle \Psi_0 | \hat{\mathcal{H}} | \Psi_0 \rangle$.

From the minimization condition $\delta\mathcal{L} = 0$ and the expression for the total energy of a single Slater determinant

$$\begin{aligned} E_0 &= \sum_a \langle \chi_a | \hat{h}_0(1) | \chi_a \rangle + \frac{1}{2} \sum_{a,b} \langle \chi_a, \chi_b | \hat{v}(1, 2) | \chi_a, \chi_b \rangle \\ &\quad - \frac{1}{2} \sum_{a,b} \langle \chi_a, \chi_b | \hat{v}(1, 2) | \chi_b, \chi_a \rangle \end{aligned} \quad (\text{E.6})$$

E Non-Collinear Unrestricted Hartree-Fock Approximation

we find the following effective single particle Hamiltonian - the Fock operator

$$\begin{aligned}\hat{\mathcal{F}} &= \hat{\mathcal{H}}_0 + \sum_{i,j,\sigma} \sum_{k,l} \rho_{ik}^{\sigma\sigma} \langle \phi_i, \phi_k | \hat{v}(1,2) | \phi_j, \phi_l \rangle \hat{c}_{i\sigma}^\dagger \hat{c}_{j\sigma} \\ &- \sum_{i,j,\sigma_1,\sigma_2} \sum_{k,l} \rho_{ik}^{\sigma_1\sigma_2} \langle \phi_i, \phi_k | \hat{v}(1,2) | \phi_l, \phi_j \rangle \hat{c}_{i\sigma_1}^\dagger \hat{c}_{j\sigma_2}\end{aligned}\quad (\text{E.7})$$

which depends on the density operator

$$\begin{aligned}\hat{\rho} &= \sum_a |\chi_a\rangle \langle \chi_a| = \sum_{i,j,\sigma_1,\sigma_2} \sum_{a=1}^N c_{ia}^{\sigma_1} (c_{ja}^{\sigma_2})^* |\phi_i^{\sigma_1}\rangle \langle \phi_j^{\sigma_2}| \\ &= \sum_{i,j,\sigma_1,\sigma_2} \rho_{ij}^{\sigma_1\sigma_2} |\phi_i^{\sigma_1}\rangle \langle \phi_j^{\sigma_2}|.\end{aligned}\quad (\text{E.8})$$

The second term in eq. (E.7) is the Hartree-term \hat{v}_H which describes the classical (direct) Coulomb repulsion of the electrons. It depends only on the (local) charge density $\rho^T(x) = \rho^{\uparrow\uparrow}(x) + \rho^{\downarrow\downarrow}(x)$:

$$\hat{v}_H = \int dx \int dy \rho^T(y) v(x,y) \sum_{\sigma} \hat{\psi}_{\sigma}^{\dagger}(x) \hat{\psi}_{\sigma}(x), \quad (\text{E.9})$$

while the third term really depends on the density matrix. This is the Fock-term \hat{v}_F describing the exchange energy:

$$\hat{v}_F = \sum_{\sigma_1,\sigma_2} \int dx \int dy \rho^{\sigma_1\sigma_2}(x,y) v(x,y) \hat{\psi}_{\sigma_1}^{\dagger}(x) \hat{\psi}_{\sigma_2}(y). \quad (\text{E.10})$$

Clearly, only the Fock-term can give rise to non-collinear spin-arrangements. Moreover, only if the initial guess contains non-diagonal terms with respect to the spin, i.e. only if $\rho^{\sigma_1\sigma_2}(x,y) \neq 0$ for $\sigma_1 \neq \sigma_2$, the self-consistent Hartree-Fock solution can have a non-collinear spin configuration.

Bibliography

- [1] B. Doyle *et al.*, Intel Tech. J. **6**, 42 (2002).
- [2] J. R. Black, RADDC Tech. Rep. **243**, (1968).
- [3] J. Kao, S. Narendra, and A. Chandrakasan, in *Proceedings of the 2002 IEEE/ACM international conference on Computer-aided design* (ACM Press, New York, NY, USA, 2002).
- [4] A. Aviram and M. A. Ratner, Chem. Phys. Lett. **29**, 277 (1974).
- [5] G. Binning, H. Bohrer, C. Gerber, and E. Weibel, Phys. Rev. Lett. **49**, 57 (1982).
- [6] C. Joachim, J. K. Gimzewski, R. R. Schlittler, and C. Chavy, Phys. Rev. Lett. **74**, 2102 (1995).
- [7] C. Joachim and J. K. Gimzewski, Chem. Phys. Lett. **265**, 353 (1997).
- [8] M. A. Reed *et al.*, Science **278**, 252 (1997).
- [9] C. K. *et al.*, Phys. Rev. B **59**, 12505 (1999).
- [10] X. D. Cui *et al.*, Science **294**, 571 (2001).
- [11] R. H. M. Smit *et al.*, Nature (London) **419**, 906 (2002).
- [12] A. R. Champagne, A. N. Pasupathy, and D. C. Ralph, Nano Lett. **5**, 305 (2005).
- [13] N. Agrait, A. L. Yegati, and J. M. van Ruitenbeek, Physics Reports **377**, 81 (2003).
- [14] J. K. Gimzewski and R. Möller, Phys. Rev. B **36**, 1284 (1987).
- [15] C. J. Muller, J. M. van Ruitenbeek, and L. J. de Jong, Phys. Rev. Lett. **69**, 140 (1992).
- [16] A. F. Morpurgo, C. M. Marcus, and D. B. Robinson, Appl. Phys. Lett. **74**, 2084 (1999).
- [17] C. Z. Li, A. Bogozzi, W. Huang, and N. J. Tao, Nanotechnology **10**, 221 (1999).
- [18] C. Untiedt *et al.*, Phys. Rev. B **66**, 085418 (2002).
- [19] S. A. Wolf *et al.*, Science **294**, 1488 (2001).
- [20] S. S. P. Parkin *et al.*, J. Appl. Phys. **85**, 5828 (1999).
- [21] M. N. Baibich *et al.*, Phys. Rev. Lett. **61**, 2472 (1988).
- [22] M. Julliere, Phys. Lett. **54A**, 225 (1975).

Bibliography

- [23] W. J. Gallagher and S. S. P. Parkin, IBM J. Res. Dev. **50**, 5 (2006).
- [24] W. H. Butler, X.-G. Zhang, T. C. Schulthess, and J. M. MacLaren, Phys. Rev. B **63**, 054416 (2001).
- [25] J. Mathon and A. Umerski, Phys. Rev. B **63**, 220403 (2001).
- [26] D. D. Djayaprawira *et al.*, Appl. Phys. Lett. **86**, 092502 (2005).
- [27] H. Oshima and K. Miyano, Appl. Phys. Lett. **73**, 2203 (1998).
- [28] N. García, M. Muñoz, and Y. W. Zhao, Phys. Rev. Lett. **82**, 2923 (1999).
- [29] T. Ono, Y. Ooka, H. Miyajima, and Y. Otani, Appl. Phys. Lett. **75**, 1622 (1999).
- [30] S. H. Chung *et al.*, Phys. Rev. Lett. **89**, 287203 (2002).
- [31] M. Viret *et al.*, Phys. Rev. B **66**, 220401(R) (2002).
- [32] H. D. Chopra and S. Z. Hua, Phys. Rev. B **66**, 020403(R) (2002).
- [33] S. Z. Hua and H. D. Chopra, Phys. Rev. B **67**, 060401(R) (2003).
- [34] C. Untiedt *et al.*, Phys. Rev. B **69**, 081401(R) (2004).
- [35] M. R. Sullivan *et al.*, Phys. Rev. B **71**, 024412 (2005).
- [36] M. Gabureac, M. Viret, F. Ott, and C. Fermon, Phys. Rev. B **69**, 100401(R) (2004).
- [37] K. I. Bolotin, F. Kuemmeth, A. N. Pasupathy, and D. C. Ralph, Nano Lett. **6**, 123 (2006).
- [38] Z. K. Keane, L. H. Yu, and D. Natelson, Appl. Phys. Lett. **88**, 062514 (2006).
- [39] P. Bruno, Phys. Rev. Lett. **83**, 2425 (1999).
- [40] G. Tatara, Y. W. Zhao, M. Muñoz, and N. García, Phys. Rev. Lett. **83**, 2030 (1999).
- [41] H. Imamura, N. Kobayashi, S. Takahashi, and S. Maekawa, Phys. Rev. Lett. **84**, 1003 (2000).
- [42] K. Tsukagoshi, B. W. Alpenhaar, and H. Ago, Nature **401**, 572 (1999).
- [43] L. E. Hueso *et al.*, Nature **445**, 410 (2007).
- [44] M. Ouyang and D. D. Awschalom, Science **301**, 1074 (2003).
- [45] M. Brandbyge, M. R. Sørensen, and K. W. Jacobsen, Phys. Rev. B **56**, 14956 (1997).
- [46] J. C. C. *et al.*, Phys. Rev. Lett. **81**, 2990 (1998).
- [47] M. J. Frisch *et al.*, Gaussian 03, Revision B.01, Gaussian, Inc., Pittsburgh PA, 2003.
- [48] P. Ordejón, E. Artacho, and J. M. Soler, Phys. Rev. B **53**, 10441 (1996).
- [49] P. Hohenberg and W. Kohn, Phys. Rev. **136**, B864 (1964).

- [50] J. J. Palacios, A. J. Pérez-Jiménez, E. Louis, and J. A. Vergés, *Phys. Rev. B* **64**, 115411 (2001).
- [51] J. J. Palacios *et al.*, ALACANT ab-initio transport package, ALACANT release 1.0, Condensed Matter Theory Group, Universidad de Alicante, <http://www.guirisystems.com/alacant>.
- [52] J. J. Palacios *et al.*, in *Computational Chemistry: Reviews of Current Trends*, edited by J. Leszczynski (World Scientific, Singapore-New Jersey-London-Hong Kong, 2005), Vol. 9, in press.
- [53] M. Brandbyge *et al.*, *Phys. Rev. B* **65**, 165401 (2002).
- [54] A. R. Rocha *et al.*, *Phys. Rev. B* **73**, 085414 (2006).
- [55] D. Jacob, J. Fernández-Rossier, and J. J. Palacios, *Phys. Rev. B* **71**, 220403(R) (2005).
- [56] D. Jacob and J. J. Palacios, *Phys. Rev. B* **73**, 075429 (2006).
- [57] A. Delin and E. Tosatti, *Surface Science* **566**, 262 (2004).
- [58] A. Delin and E. Tosatti, *J. Phys. Cond. Mat.* **16**, 8061 (2004).
- [59] J. Fernández-Rossier, D. Jacob, C. Untiedt, and J. J. Palacios, *Phys. Rev. B* **72**, 224418 (2005).
- [60] R. Landauer, *IBM J. Res. Dev.* **1**, 233 (1957).
- [61] R. Landauer, *Philos. Mag.* **21**, 863 (1970).
- [62] M. Büttiker, *Phys. Rev. Lett.* **57**, 1761 (1986).
- [63] M. Büttiker, *IBM J. Res. Develop.* **32**, 63 (1988).
- [64] S. Datta, *Electronic transport in mesoscopic systems* (Cambridge University Press, Cambridge, 1995).
- [65] N. W. Ashcroft and N. D. Mermin, *Solid State Physics* (Harcourt College Publishers, Orlando, 1976).
- [66] E. N. Economou, *Green's functions in Quantum Physics*, No. 7 in *Springer Series in Solid State Physics* (Springer, Berlin-Heidelberg-New York-Tokyo, 1970).
- [67] M. Paulsson, cond-mat/0210519 (unpublished).
- [68] J. K. Viljas, J. C. Cuevas, F. Pauly, and M. Häfner, *Phys. Rev. B* **72**, 245415 (2005).
- [69] K. S. Thygesen, *Phys. Rev. B* **73**, 035309 (2006).
- [70] A. Szabo and N. S. Ostlund, *Modern Quantum Chemistry* (McGraw-Hill, New York, 1989).
- [71] C. Caroli, R. Combescot, and P. Dederichs, *J. Phys. C: Sol. State Phys.* **4**, 916 (1971).

Bibliography

- [72] J. Bardeen, Phys. Rev. Lett. **6**, 57 (1961).
- [73] Y. Meir and N. Wingreen, Phys. Rev. Lett. **68**, 2512 (1992).
- [74] G. D. Mahan, *Many-Particle Physics*, 3 ed. (Plenum Press, New York, 2000).
- [75] T. Frederiksen, M. Brandbyge, N. Lorente, and A.-P. Jauho, Phys. Rev. Lett. **93**, 256601 (2004).
- [76] J. L. D'Amato and H. M. Pastawski, Phys. Rev. B **41**, 7411 (1990).
- [77] W. Koch and M. C. Holthausen, *A chemist's guide to density functional theory* (Wiley-VCH, Weinheim, 2001).
- [78] R. O. Jones and O. Gunnarsson, Rev. Mod. Phys. **61**, 689 (1989).
- [79] W. Kohn and L. J. Sham, Phys. Rev. **140**, A1133 (1965).
- [80] T. C. Leung, C. T. Chan, and B. N. Harmon, Phys. Rev. B **44**, 2923 (1991).
- [81] A. D. Becke, J. Chem. Phys. **98**, 5648 (1993).
- [82] I. P. R. Moreira, F. Illas, and R. L. Martin, Phys. Rev. B **65**, 155102 (2002).
- [83] V. I. Anisimov, J. Zaanen, and O. K. Andersen, Phys. Rev. B **44**, 943 (1991).
- [84] V. I. Anisimov *et al.*, Phys. Rev. B **48**, 16929 (1993).
- [85] A. Görling, Phys. Rev. B **53**, 7024 (1996).
- [86] M. Städele, J. A. Majewski, P. Vogl, and A. Görling, Phys. Rev. Lett. **79**, 2089 (1997).
- [87] M. Städele *et al.*, Phys. Rev. B **59**, 10031 (1999).
- [88] J. Taylor, H. Guo, and J. Wang, Phys. Rev. B **63**, 245407 (2001).
- [89] P. S. Damle, A. W. Ghosh, and S. Datta, Phys. Rev. B **64**, 201403(R) (2001).
- [90] S.-H. Ke, H. U. Baranger, and W. Yang, J. Chem. Phys. **123**, 114701 (2005).
- [91] K. S. Thygesen and K. W. Jacobsen, Phys. Rev. B **72**, 033401 (2005).
- [92] F. Muñoz Rojas, D. Jacob, J. Fernández-Rossier, and J. J. Palacios, Phys. Rev. B **74**, 195417 (2006).
- [93] N. D. Lang, Phys. Rev. B **52**, 5335 (1995).
- [94] K. Hirose and M. Tsukada, Phys. Rev. B **51**, 5278 (1995).
- [95] Y. Fujimoto and K. Hirose, Phys. Rev. B **67**, 195315 (2003).
- [96] L. F. Pacios and P. A. Christiansen, J. Chem. Phys. **82**, 2664 (1985).
- [97] A. Papaconstantopoulos, *Handbook of the Band Structure of Elemental Solids* (Plenum Press, ADDRESS, 1986).

- [98] V. Saunders *et al.*, CRYSTAL03, Release 1.0.2, Theoretical Chemistry Group - Universita' Di Torino - Torino (Italy).
- [99] D. Jacob and J. J. Palacios, in preparation (unpublished).
- [100] J. Kondo, Prog. Theor. Phys. **32**, 37 (1964).
- [101] P. W. Anderson, Phys. Rev. **124**, 41 (1961).
- [102] E. Runge and E. K. U. Gross, Phys. Rev. Lett. **52**, 997 (1984).
- [103] M. Koentopp, C. Chang, K. Burke, and R. Car, cond-mat/0703591 (unpublished).
- [104] G. Stefanucci, S. Kurth, E. K. U. Gross, and A. Rubio, cond-mat/0607333 (unpublished).
- [105] K. S. Thygesen and A. Rubio, cond-mat/0609223 (unpublished).
- [106] P. Darancet, A. Ferretti, D. Mayou, and V. Olevano, cond-mat/0611404 (unpublished).
- [107] G. Kotliar *et al.*, Rev. Mod. Phys. **78**, 865 (2005).
- [108] A. Auerbach, *Interacting Electrons and Quantum Magnetism* (Springer-Verlag, New York, 1994).
- [109] A. Montorosi, *The Hubbard Model* (World Scientific, Singapore-New Jersey-London-Hong Kong, 1992).
- [110] P. Fazekas, *Lecture Notes on Electron Correlation and Magnetism*. (World Scientific, Singapore-New Jersey-London-Hong Kong, 1999).
- [111] G. Tatara and H. Fukuyama, Phys. Rev. Lett. **78**, 3773 (1997).
- [112] A. Smogunov, A. DalCorso, and E. Tosatti, Surf. Sci. **507**, 609 (2002).
- [113] A. Smogunov, A. D. Corso, and E. Tosatti, Surf. Sci. **566**, 390 (2004).
- [114] S. H. Vosko, L. Wilk, and M. Nussair, Can. J. Phys. **58**, 1200 (1980).
- [115] K. Doll, Surf. Science **544**, 103 (2003).
- [116] M. M. Hurley *et al.*, J. Chem. Phys **84**, 6840 (1986).
- [117] M. Wierzbowska, A. Delin, and E. Tosatti, cond-mat/0412267 (unpublished).
- [118] J. B. A. N. van Hoof *et al.*, Phys. Rev. B **59**, 138 (1999).
- [119] A. Bagrets, N. Papanikolaou, and I. Mertig, Phys. Rev. B **70**, 064410 (2004).
- [120] J. C. Cuevas, A. L. Yeyati, and A. Martín-Rodero, Phys. Rev. Lett. **80**, 1066 (1998).
- [121] K. S. Thygesen and K. W. Jacobsen, Phys. Rev. Lett. **94**, 036807 (2005).
- [122] J. K. Perry, J. Tahir-Kheli, and W. A. Goddard, Phys. Rev. B **63**, 144510 (2001).

Bibliography

- [123] J. P. Perdew and A. Zunger, Phys. Rev. B **23**, 5048 (1981).
- [124] E. Scheer *et al.*, Nature (London) **394**, 154 (1998).
- [125] A. Smogunov, A. DalCorso, and E. Tosatti, Phys. Rev. B **73**, 075418 (2006).
- [126] F. Pauly *et al.*, Phys. Rev. B **74**, 235106 (2006).
- [127] W. F. Egelhoff *et al.*, J. Appl. Phys. **95**, 7554 (2004).
- [128] A. Ohtomo and H. Y. Hwang, Nature **427**, 423 (2004).
- [129] S. Okamoto and A. J. Millis, Nature **428**, 630 (2004).
- [130] S. Gallego, J. I. Beltrán, J. Cerdá, and M. C. Munoz, J. Phys.: Condens. Matter **17**, L451 (2005).
- [131] N. Agraït, A. L. Yeyati, and J. M. van Ruitenbeek, Physics Reports **377**, 81 (2003), and references therein.
- [132] W. H. A. Thijssen, D. Marjenburgh, R. H. Bremmer, and J. M. van Ruitenbeek, Phys. Rev. Lett. **96**, 026806 (2006).
- [133] A. Bagrets, N. Papanikolaou, and I. Mertig, cond-mat/0510073 (unpublished).
- [134] N. Papanikolaou, J. Phys.: Condens. Matter **15**, 5049 (2003).
- [135] G. A. Sawatzky and J. W. Allen, Phys. Rev. Lett. **53**, 2339 (1984).
- [136] K. Terakura, T. Oguchi, A. R. Williams, and J. Kübler, Phys. Rev. B **30**, 4734 (1984).
- [137] J. Zaanen, G. A. Sawatzky, and J. W. Allen, Phys. Rev. Lett. **55**, 418 (1985).
- [138] M. Towler *et al.*, Phys. Rev. B **50**, 5041 (1994).
- [139] F. Aryasetiawan and O. Gunnarsson, Phys. Rev. Lett. **74**, 3221 (1995).
- [140] O. Tjernberg *et al.*, Phys. Rev. B **54**, 10245 (2005).
- [141] T. Bredow and A. R. Gerson, Phys. Rev. B **61**, 5194 (2000).
- [142] E. Ruiz, M. Llunell, and P. Alemany, J. Solid State Chem. **176**, 400 (2003).
- [143] K. Doll, M. Dolg, P. Fulde, and H. Stoll, Phys. Rev. B **55**, 10282 (1997).
- [144] S. R. Bahn and K. W. Jacobsen, Phys. Rev. Lett. **87**, 266101 (2001).
- [145] A. Delin and E. Tosatti, Phys. Rev. B **68**, 144434 (2003).
- [146] T. Nautiyal, T. H. Rho, and K. S. Kim, Phys. Rev. B **69**, 193404 (2004).
- [147] C. Sirvent *et al.*, Phys. Rev. B **53**, 16086 (1996).
- [148] R. H. S. *et al.*, Phys. Rev. Lett. **87**, 266102 (2001).

- [149] R. H. S. *et al.*, Phys. Rev. Lett. **91**, 076805 (2003).
- [150] S. K. Nielsen *et al.*, Phys. Rev. B **67**, 245411 (2003).
- [151] P. C. S. V. Rodrigues, J. Bettini and D. Ugarte, Phys. Rev. Lett. **91**, 096801 (2003).
- [152] A. Delin, E. Tosatti, and R. Weht, Phys. Rev. Lett. **92**, 057201 (2004).
- [153] V. S. Stepanyuk *et al.*, Phys. Rev. B **70**, 195420 (2004).
- [154] L. de la Vega, A. Martín-Rodero, A. L. Yeyati, and A. Saúl, Phys. Rev. B **70**, 113107 (2004).
- [155] Y. García *et al.*, Phys. Rev. B **69**, 041402(R) (2004).
- [156] K. S. T. *et al.*, Phys. Rev. B **72**, 033401 (2005).
- [157] S. W. B. C. J. L. S. S. V. M. García-Suárez, A. R. Rocha and J. Ferrer, Phys. Rev. Lett. **95**, 256804 (2005).
- [158] K. Doll, Surface Science **573**, 464 (2004).
- [159] M. Wierzbowska, A. Delin, and E. Tosatti, Phys. Rev. B **72**, 035439 (2005).
- [160] A. Ferretti *et al.*, Phys. Rev. Lett. **94**, 116802 (2005).
- [161] A. Caneschi *et al.*, J. Am. Chem. Soc. **113**, 5873 (1991).
- [162] C. Untiedt and J. M. van Ruitenbeek, unpublished (unpublished).
- [163] J. Velev, R. F. Sabirianov, S. S. Jaswal, and E. Y. Tsympal, Phys. Rev. Lett. **94**, 127203 (2005).
- [164] L. Brey, C. Tejedor, and J. Fernández-Rossier, Appl. Phys. Lett. **85**, 1996 (2004).
- [165] F. D. Novaes, A. J. R. daSilva, E. daSilva, and A. Fazzio, Phys. Rev. Lett. **96**, 016104 (2006).
- [166] P. Crespo *et al.*, Phys. Rev. Lett. **93**, 087204 (2004).
- [167] E. G. Moroni, G. Kresse, J. Hafner, and J. Furthmüller, Phys. Rev. B **56**, 15629 (1997).
- [168] A. Grechnev *et al.*, cond-mat/0610621 (unpublished).
- [169] K. D. Belashchenko, V. P. Antropov, and N. E. Zein, Phys. Rev. B **73**, 073105 (2006).
- [170] K. I. Bolotin, F. Kuemmeth, and D. C. Ralph, Phys. Rev. Lett. **97**, 127202 (2006).
- [171] M. Viret *et al.*, Eur. Phys. J. B **51**, 1 (2006).

List of abbreviations

AMR	Anisotropic magneto-resistance
BL	Bethe lattice
BMR	Ballistic magneto-resistance
DFT	Density functional theory
DOS	Density of states
EXX	Exact exchange
GF	Green's function
GGA	Generalized gradient approximation
GMR	Giant magneto-resistance
HF	Hartree-Fock
HFA	Hartree-Fock approximation
HFX	Hartree-Fock exchange
IC	Integrated circuit
KS	Kohn-Sham
LDA	Local density approximation
LDOS	Local density of states
LSDA	Local spin density approximation
NOBS	Non-orthogonal basis set
PDOS	Projected density of states
MCBJ	Mechanically controllable break junction
MR	Magneto-resistance
NEGF	Non-equilibrium Green's function
STM	Scanning tunneling microscope
TMR	Tunneling magneto-resistance

List of publications

F. Muñoz-Rojas, D. Jacob, J. Fernández-Rossier, and J. J. Palacios
Coherent transport in graphene nanoconstrictions
Phys. Rev. B **74**, 195417 (2006)

D. Jacob, J. Fernández-Rossier, and J. J. Palacios
Electronic structure and transport properties of atomic NiO spinvalves
J. Magn. Magn. Mater. **310**, e675-e677 (2007)

D. Jacob, J. Fernández-Rossier, and J. J. Palacios
Emergence of half-metallicity in suspended NiO chains
Phys. Rev. B **74**, 081402(R) (2006).

D. Jacob and J. J. Palacios
Orbital eigenchannel analysis for ab initio quantum transport calculations
Phys. Rev. B **73**, 075429 (2006)

J. Fernández-Rossier, D. Jacob, C. Untiedt, and J. J. Palacios
Transport through magnetically ordered Pt nanocontacts
Phys. Rev. B **72**, 224418 (2005)

D. Jacob, J. Fernández-Rossier, and J. J. Palacios
Magnetic and orbital blocking in Ni nanocontacts
Phys. Rev. B **71**, 220403(R) (2005)

B. Wunsch, D. Jacob, and D. Pfannkuche
Isospin blockade in transport through vertical double quantum dots
Physica, E **26**, 464 (2005)

D. Jacob, B. Wunsch, and D. Pfannkuche
Charge localization and isospin blockade in vertical double quantum dots
Phys. Rev. B **70**, 081314(R) (2004)

In preparation:

D. Jacob, J. Fernandez-Rossier and J. J. Palacios
Anisotropic magneto-resistance in nanocontacts

D. Soriano, D. Jacob and J. J. Palacios
A localized basis set description of free electrons

D. Jacob and J. J. Palacios
Comparison of electrode models for ab initio quantum transport calculations

D. Jacob, J. Fernández-Rossier, and J. J. Palacios
Domainwall formation and scattering in one-dimensional chains